Universitat Politècnica de Catalunya

Doctoral Thesis

Barocaloric effects at first-order phase transitions

Author:
Araceli Aznar Luque

Supervisor:
Dr. Pol M. Lloveras
Dr. Josep Lluís Tamarit

A thesis submitted in fulfillment of the requirements for the degree of Doctor of Philosophy

in the

Group of Characterization of Materials (GCM), PhD programme in Computational and Applied Physics
Department of Physics

February 2021

A l'Adrià i a la Carmen

Abstract

Preserving food has always been one of the major concerns of mankind. In ancient times, food was conserved and transported for commercialization purposes using ice, which was previously cut from iced rivers and mountains and sold to merchants [1]. Nonetheless, this was obviously unpractical and problematic, and thus alternatives and better solutions were needed for refrigeration to be available anywhere, anytime. In fact, ice trade continued in Europe until the end of the XIX century, when the first mechanical refrigeration devices that did not rely on ice started to popularize. At present, refrigeration plays a major role in our daily lives and is employed for purposes beyond food preservation. For instance, the pharmaceutical industry requires strict temperature control for many processes. In parallel, the internet and all data storage servers require constant refrigeration to counterbalance their natural temperature increase and to avoid system failures. As a last example, it is clear that in a context of global warming, air-conditioning, which is implemented both for domestic and industrial purposes (transport and space cooling), is becoming an ever-greater need. All in all, it is clear that refrigeration is indispensable for sustaining our current lifestyle. In particular, the total amount of refrigeration setups in operation in 2018 was about 3.6 billion, where only domestic refrigeration corresponds to the 67 % of units [2].

Refrigerants used in the first cooling devices in the early XIX century were diethyl ether (R-610), dimethyl ether (R-170), carbon dioxide (R-744), ammonia (R-717), sulfur dioxide (R-764) and methyl chloride (R-40) [3, 4], which exhibited sever drawbacks concerning toxicity and flammability. Some of the reported accidents are quite recent (see Refs. [5, 6]), since unfortunately, these last chem-

icals persisted during a long time, and in fact are still in use in some developing countries. When domestic refrigeration was implemented at the end of the XIX century, new toxicity-free refrigerants were required [7]. During the first third of the XX century, the last refrigerants were replaced by chlorofluorocarbons (CFC) and hydrochlorofluorocarbons (HCFC), synthesized by General Motors [8], which showed no toxicity issues and remained in the market during the next 60 years.

Around 1980, the ozone depletion layer was discovered. This damage was mainly caused by the chlorine gas-based emissions to the atmosphere [9]. Consequently, in 1987, the Montreal Protocol [10] prohibited the use of CFC as a refrigerant and programmed the progressive removal of HCFC among other damaging substances in order to put an end to this global emergency. HCFC and CFC were replaced by hydrofluorocarbons (HFC), which were identified as non-ozone depletion refrigerants. Unfortunately, these gases exhibit a global warming potential (GWP) of approximately a thousand times that produced by CO_2 [7] considering the same time lapse of 100 years. Additionally, they currently contribute with around 7.8% of the total greenhouse emissions [7]. Therefore, in 2016, the Kigali amendment [11] to the Montreal Protocol accorded to reduce the production and consumption of HFC. This amendment along with the ever-greater middle class and their increasing refrigeration needs (which currently accounts for 17% of the global energy used [12]), creates the urgency for research to discover new eco-friendly cooling technologies. The potential replacement of these refrigerants could reduce the greenhouse emissions in 3%, with a direct impact on the environment [7].

Solid-state caloric effects have been proposed as green alternatives to replace the present-day gas-compression devices. They may arise when applying an external field which induces a first-order phase transition with changes in entropy or temperature. Caloric effects may be driven by magnetic field (magnetocaloric, MC), electric field (electrocaloric, EC), uniaxial stress (elastocaloric, eC) and hydrostatic pressure (barocaloric, BC). Although eC was the first caloric effect observed (in 1805) [13], the MC effect, discovered in 1917 [14], took the lead quite recently in 1976, when room temperature magnetocaloric cooling was achieved

using Gd [15]. From that moment, the interest in potential magnetocaloric refrigeration materials increased. The EC effect was first discovered in the Rochelle salt in 1930 [16], and as for the eC effect, it did not spark great interest until the discovery of their respective giant effects in $Cu_{69.6}Al_{27.7}Ni_{2.7}$ [17] and $Fe_{49}Rh_{51}$ [18] in 1980 and 1990, respectively. Lastly, the BC effect was first reported in rare-earths $Pr_{1-x}La_xNiO_3$ and CeSb in 2000 [19]. But the interest was not renewed until 2010, when giant BC effects were reported in the Ni-Mn-In magnetic alloy [20], which competed with other caloric effects previously described. In Fig. 1 the evolution of segregated caloric effects publications is displayed.

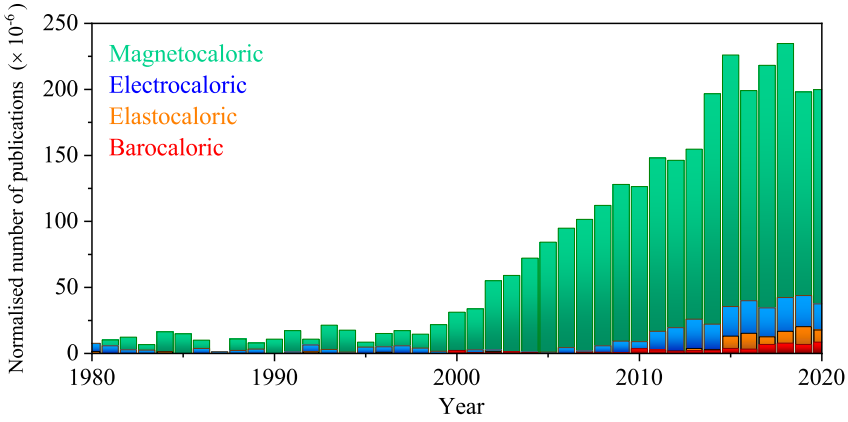

Figure 1: Number of year publications for each caloric type normalized by the total amount of indexed publications. Data obtained from Scopus database.

Drawbacks and advantages must be evaluated for each caloric effect when considering a potential implementation. MC materials usually require from high magnetic fields to induce the heat exchanges required by a real refrigeration device. Also, MC materials are usually composed by rare-earths elements which may suppose high production costs. High fields are equally needed for EC materials to achieve useful temperature changes. Therefore, good EC performances are observed in thin films. MC, EC and eC often exhibit fatigue upon cyclic field changes, which is one of the most important concerns to be overcome. However, powdered compounds are allowed when designing a BC device, which avoid the problem of fatigue upon cycling. Additionally, the range of materials that exhibit BC effects is wider than for the other caloric effects. For this reason further research in new

materials showing good BC performances is encouraged.

In this dissertation the study of BC effects of some compounds belonging to four different material families are reported. In Chapter 1 the theoretical introduction to the concept of BC effects along with the methods required in order to determine them are presented. Chapter 2 describes the experimental setups used in this work, and the remaining chapters provide the BC results of each material family: Plastic crystals (Chapter 3), hybrid organic-inorganic perovskites (Chapter 4), magnetic alloys (Chapter 5) and the superionic conductor AgI (Chapter 6). Finally, in Chapter 7 the results are discussed as a whole. The aim of this work is, apart from presenting individual materials with potential real applications as solid refrigerants, to make a general perspective and comparison of the BC behavior of different material families.

Contents

Chapter 1

INTRODUCTION

We experimentally observe that pressure application and removal following adiabatic and isothermal paths produces changes in both the system temperature and entropy, respectively. These variations are referred to as barocaloric effects since they are driven by changes in hydrostatic pressure. As entropy variations imply heat exchanges, they can be exploited to build refrigeration cycles. If the application and removal of hydrostatic pressure is capable of inducing a first-order phase transition, the overall exchanged heat will be of the order of the latent heat, therefore possibly resulting in giant barocaloric effects. Nowadays this is the principle used in current devices which rely on liquid-vapor transitions driven by hydrostatic pressure. In particular, this thesis explores the barocaloric behavior of solid materials undergoing a solid-solid phase transition which in the future may create a place of its own in the refrigeration devices market due to its technological and environmental advantages. In this chapter the fundamentals of thermodynamics of the barocaloric effects are presented. We describe the main features required from a certain compound to be considered as a barocaloric material to be implemented in future devices.

1.1 Thermodynamics of barocaloric effects

From the first law of thermodynamics we are able to write the exact differential of the internal energy (dU) for a pVT system (where p, V and T stand for pressure, volume and temperature, respectively) as [21]

$$dU = TdS - pdV, \tag{1.1}$$

where S is the entropy, and TdS and $-pdV$ are the reversible heat and the reversible work exchanged by the system, respectively. At this point, if we express the internal energy as an exact differential, we can identify the following quantities. First, differentiating with respect to volume and entropy we obtain

$$\left(\frac{\partial U}{\partial S}\right)_V = T \quad \text{and} \quad \left(\frac{\partial U}{\partial V}\right)_S = -p. \tag{1.2}$$

Deriving again with respect to the opposite variables, the last expressions lead to

$$\frac{\partial^2 U}{\partial V \partial S} = \left(\frac{\partial T}{\partial V}\right)_S \quad \text{and} \quad \frac{\partial^2 U}{\partial S \partial V} = -\left(\frac{\partial p}{\partial S}\right)_V. \tag{1.3}$$

Applying the exact differential relation $\left(\frac{\partial^2 U}{\partial S \partial V} = \frac{\partial^2 U}{\partial V \partial S}\right)$ the following equality is derived

$$\left(\frac{\partial V}{\partial T}\right)_S = -\left(\frac{\partial S}{\partial p}\right)_V. \tag{1.4}$$

Equation 1.4 is known as the first *Maxwell relation*, which relate the entropy variation with respect to pressure under isochoric conditions with the adiabatic variation of volume with respect to temperature.

Recall that our purpose is to compute the isothermal entropy and adiabatic temperature variations upon applied pressures. Consequently, in order to deduce the mathematical expressions for the barocaloric effects we first need to express the dS in terms of the intensive thermodynamic variables T and p as

$$dS = \left(\frac{\partial S}{\partial T}\right)_p dT + \left(\frac{\partial S}{\partial p}\right)_T dp. \tag{1.5}$$

If the heat capacity expression at constant pressure $C_p = T\left(\frac{\partial S}{\partial T}\right)_p$ and the first Maxwell relation (derived in equation 1.4) are introduced into equation 1.5, we obtain

$$dS = \frac{C_p}{T}dT - \left(\frac{\partial V}{\partial T}\right)_p dp. \tag{1.6}$$

When an isothermal path is established ($dT = 0$), we derive the isothermal entropy changes observed when increasing pressure from p_0 to p_1. After integration, equation 1.6 can be written as

$$(dS)_T = -\left(\frac{\partial V}{\partial T}\right)_p dp \quad \Rightarrow \quad \boxed{\Delta S(T, p_0 \rightarrow p_1) = -\int_{p_0}^{p_1}\left(\frac{\partial V}{\partial T}\right)_p dp.} \tag{1.7}$$

Contrary, when considering an adiabatic path ($dS = 0$) the expression for the adiabatic temperature change is determined

$$\frac{C_p}{T}dT = \left(\frac{\partial V}{\partial T}\right)_p dp \quad \Rightarrow \quad \boxed{\Delta T(S, p_0 \rightarrow p_1) = \int_{p_0}^{p_1}\frac{T}{C_p}\left(\frac{\partial V}{\partial T}\right)_p dp.} \tag{1.8}$$

Equations 1.7 and 1.8 refer to the so-called *barocaloric effects*. Notice that this formulation can be generalized for other pair of generalized variables (X) and conjugate fields (y), such as magnetization and magnetic field ($X = M$, $y = H$, for *magnetocaloric effect*) [22, 23], polarization and electric field ($X = P$, $y = E$, for *electrocaloric effect*) [24, 25] and uniaxial stress and strain ($X = \sigma$, $y = \epsilon$, for *elastocaloric effect*) [26, 27], where the isothermal entropy and adiabatic temperature changes are derived in terms of the corresponding conjugate fields.

This thesis will focus on caloric effects induced by means of hydrostatic pressure. Hence, equations will keep the intensive variables T and p with their corresponding conjugate variables S and V, respectively. From equations 1.7 and 1.8, it is observed that in the case of materials presenting positive thermal expansion $\left[\alpha = \frac{1}{V}\left(\frac{\partial V}{\partial T}\right)_p > 0\right]$, negative values of $\Delta S(T, p_0 \rightarrow p_1)$ and positive values of $\Delta T(S, p_0 \rightarrow p_1)$ are obtained upon compression [28, 29]. As this is the most frequent situation, its is referred as a *conventional* barocaloric effect. Contrary, materials showing negative thermal expansions $\left[\alpha = \frac{1}{V}\left(\frac{\partial V}{\partial T}\right)_p < 0\right]$ yield positive values of $\Delta S(T, p_0 \rightarrow p_1)$ and negative values of $\Delta T(S, p_0 \rightarrow p_1)$ under pressure

increase [30, 31]. This behavior is consequently non-conventional and compounds showing this performance present *inverse* barocaloric effects.

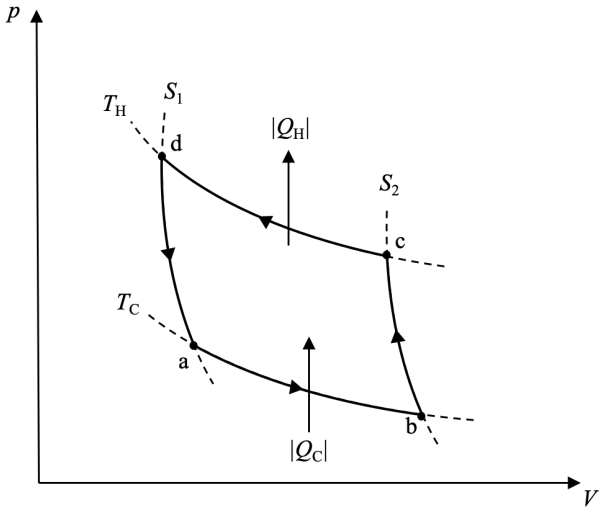

Figure 1.1: Inverse Carnot cycle of an ideal gas, where subscripts H and C stand for hot and cold respectively. Dashed lines of T_{H} and T_{C} (where $T_{\mathrm{C}} < T_{\mathrm{H}}$) show isothermal paths, while lines S_1 and S_2 represent adiabatic processes where $S_1 < S_2$. Solid lines show the path of the Carnot cycle.

Cooling devices may use different refrigeration cycles. Barocaloric effects are formulated according to the fundamental definition of the Carnot cycle, involving isothermal and adiabatic changes as shown in Fig. 1.1 for an ideal gas. It is observed that during the isothermal pressure release at T_C heat is absorbed by the gas from the cold reservoir ($|Q_C|$), which leads to positive changes in entropy of the gas ($\Delta S(T_C, p_a \rightarrow p_b) > 0$). In the same way, during the isothermal compression at T_H, heat is released by the gas to the hot reservoir ($|Q_H|$), resulting in negative gas entropy changes ($\Delta S(T_H, p_c \rightarrow p_d) < 0$). In the course of the adiabatic compression at S_2, temperature increases ($\Delta T(S_2, p_b \rightarrow p_c) > 0$), while temperature decreases in the adiabatic expansion at S_1 ($\Delta T(S_1, p_d \rightarrow p_a) < 0$).

1.2 First-order phase transitions and the Clausius-Clapeyron equation

In 1933 Paul Ehrenfest proposed a phase transition classification on the basis of the discontinuity of the Gibbs free energy derivative with respect to its intensive variables (Fig. 1.2) [32] . More precisely, he defined the order n as the lowest derivative order of the thermodynamic potential $G(p,T)$ which shows a discontinuity across the phase transition. Accordingly, a first-order phase transition ($n = 1$) presents a discontinuity in the first derivatives of $G(p,T)$. In this case, derivatives with respect to the intensive variables p and T yield the entropy S and volume V, respectively. Discontinuities in enthalpy are directly related with the latent heat ($\Delta H_{\mathrm{t}} = T_{\mathrm{t}} \Delta S_{\mathrm{t}}$) exchanged through the transition, which is the main attribute of this kind of transformations along with hysteresis and phase coexistence in equilibrium. It follows from Ehrenfest definition that, second-order phase transitions ($n = 2$) are continuous in first-order derivatives with respect to the state variables, while in some second-order derivatives we observe discontinuities (Table 1.1).

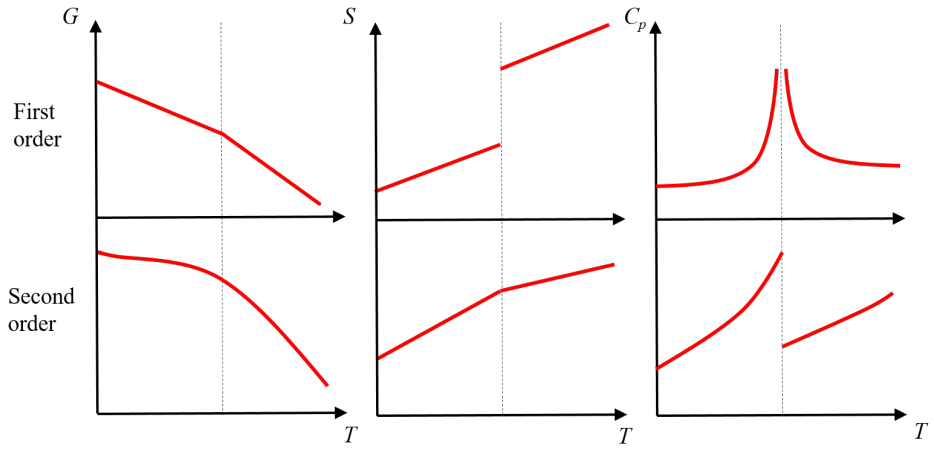

Figure 1.2: First and second row display the behavior of first- and second-order phase transitions respectively.

Let us now consider a coexistence of two phases of the same compound at

Order	Derivatives of $G(p,T)$
$n=1$	$\left(\frac{\partial G}{\partial T}\right)_p = -S$
	$\left(\frac{\partial G}{\partial p}\right)_T = V$
$n=2$	$\left(\frac{\partial^2 G}{\partial T^2}\right)_p = -\frac{C_p}{T}$
	$\left(\frac{\partial^2 G}{\partial p^2}\right)_T = -V\kappa_T$

Table 1.1: Derivatives of the free energy $G(p,T)$ for first- and second-order phase transitions [33]. κ_T stands for the isothermal compressibility.

constant values of T and p. The Gibbs free energy will read

$$G(p,T) = m_\alpha G_\alpha(p,T) + m_\beta G_\beta(p,T), \tag{1.9}$$

where m_α and m_β stand for the masses of both phases and $G_\alpha(p,T)$ and $G_\beta(p,T)$ for the corresponding specific Gibbs potentials. As p and T are constant at the phase transition, the equilibrium expression is written as

$$dG(p,T) = G_\alpha(p,T)dm_\alpha + G_\beta(p,T)dm_\beta = 0. \tag{1.10}$$

In a closed system the mass is conserved ($dm_\alpha + dm_\beta = 0 \rightarrow dm_\alpha = -dm_\beta$). Therefore, the last equation will be reduced to

$$G_\alpha(p,T) = G_\beta(p,T), \tag{1.11}$$

which can be easily generalized to a number n of coexisting phases. This situation occurs at a well determined constant values of T and p where only one degree of freedom is present. This entails that for a certain value of temperature, the pressure value at which coexistence takes place is unique. Therefore, the transition pressure is a simple function of temperature and they define the so-called *coexistence curve*. Out of the coexistence regime, the stable phase always corresponds to the one with lower Gibbs free energy. In Fig. 1.3a, the 3D surfaces $G_\alpha(p,T)$ and $G_\beta(p,T)$ of two phases of the same compound are displayed. Notice that at low temperatures, β

corresponds to the stable phase since $G_\beta(p,T) < G_\alpha(p,T)$ and analogously for the α phase at the high temperature regime. At some point, these two surfaces intersect $[G_\beta(p,T) = G_\alpha(p,T)]$ to define the previously introduced coexistence curve where being in either phase will be equally favorable energetically. If we work under isobaric conditions (shown in Fig. 1.3b) we observe that the coexistence curve reduces to a single point corresponding to the transition temperature. Additionally, the projection of the coexistence curve to the $p-T$ plane results in the phase diagram (Fig. 1.3c).

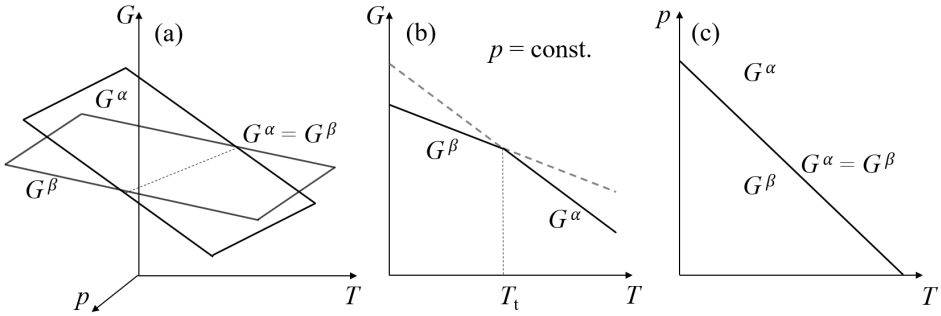

Figure 1.3: (a) Sketch of the Gibbs free energy dependence of temperature and pressure for two different phases. (b) The corresponding projection at constant pressure, where the black lines follow the system evolution, corresponding to the most stable (less energetic) Gibbs free energy at a certain pressure. (c) Projection of the $G(p,T)$ surfaces intersection in the $p-T$ plane. The intersection between both surfaces stands for the coexistence curve, which at a given pressure corresponds to a single transition temperature T_t.

In Fig. 1.4 a phase diagram is shown where a and b represent two coexistence thermodynamic states at $(p,T)_a$ and $(p,T)_b$. According to the equilibrium condition we know that $G_\alpha^{(a)} = G_\beta^{(a)}$ and $G_\alpha^{(b)} = G_\beta^{(b)}$. Consequently, as the differential Gibbs free energy is defined as $dG = Vdp - SdT$ in each phase, we are allowed to write the path $a \to b$ in terms of differential steps in temperature and pressure (dT and dp) as

$$\begin{aligned} dG_\alpha &= V_\alpha dp - S_\alpha dT \\ dG_\beta &= V_\beta dp - S_\beta dT. \end{aligned} \tag{1.12}$$

After considering that at the coexistence curve $dG_\alpha = dG_\beta$ we derive the *Clausius-*

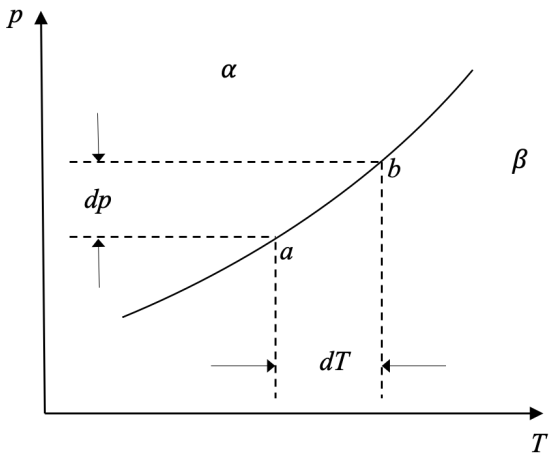

Figure 1.4: Schematic representation of a $T-p$ phase diagram where a and b show two coexisting states.

Clapeyron equation

$$V_\alpha dp - S_\alpha dT = V_\beta dp - S_\beta dT \Rightarrow (V_\alpha - V_\beta)dp = (S_\alpha - S_\beta)dT$$
$$\frac{dT}{dp} = \frac{\Delta V_\mathrm{t}}{\Delta S_\mathrm{t}}, \tag{1.13}$$

where ΔV_t and ΔS_t stand for the volume and entropy changes across the phase transformation, and $\frac{dT}{dp}$ corresponds to the slope of the coexistence curve. The Clausius-Clapeyron equation can also be written as $\frac{dT}{dp} = \frac{T\Delta V_\mathrm{t}}{\Delta H_\mathrm{t}}$, where ΔH_t is the aforementioned latent heat, characteristic of the first-order phase transitions. Materials with conventional (inverse) barocaloric effects present positive (negative) values of volume changes at the phase transition ($\Delta V_\mathrm{t} > 0$) upon heating. If the entropy changes are always positive ($\Delta S_\mathrm{t} > 0$ for an endothermic transition), according to equation 1.13, the slope of the T-p diagram $\frac{dT}{dp}$ also presents positive (negative) values [34–36]. Contrary, cooling transformations present negative entropy changes ($\Delta S_\mathrm{t} < 0$ for an exothermic transition) with also negative volume changes ($\Delta V_\mathrm{t} < 0$), which also result in positive values of $\frac{dT}{dp}$ (see Fig. 1.5, which relates conventional and inverse BCEs with the sign of the volume change at the transition) [30, 37, 38].

The transition entropy changes may contain different contributions. For in-

stance, changes in entropy due to structure variations (which may result in volume changes), and occupational, orientational and configurational disorder. Knowing the source of these contributions is of much interest, since this information would guide us to future potential barocaloric materials. From the Boltzmann equation, which relates the thermodynamic concept of entropy with the number N_i of possible microstates that lead to the same macrostate, we are able to write the following expression for the entropy changes due to configurational disorder [39]

$$\Delta S^c = \frac{R}{M}\ln(N_{\mathrm{I}}) - \frac{R}{M}\ln(N_{\mathrm{II}}) = \frac{R}{M}\ln(N_{\mathrm{I}}/N_{\mathrm{II}}), \tag{1.14}$$

where R is the ideal gas constant and M the molar mass of a certain compound.

On the other hand, the structure contribution to the entropy can be computed by means of considering a reference unstrained cubic lattice (with entropy $S^e_{\mathrm{I}} = 0$) in terms of the Helmholtz free energy (F) as

$$\Delta S^e_{\mathrm{t}} = S^e_{\mathrm{I}} - S^e_{\mathrm{II}} = -S^e_{\mathrm{II}} = \left(\frac{\partial F^e}{\partial T}\right)_e, \tag{1.15}$$

where e refers to the strain. For a cubic system, following the harmonic approximation, F^e can be written as [40]

$$F^e = \frac{1}{2}Ke_1^2 + \frac{1}{2}C'(e_2^2 + e_3^2) + \frac{1}{2}C_{44}(e_4^2 + e_5^2 + e_6^2), \tag{1.16}$$

where $K = \frac{C_{11}+2C_{21}}{3}$ and $C' = \frac{C_{11}-C_{12}}{2}$ are the bulk and deviatoric moduli respectively, and C_{ij} correspond to the components of the stiffness tensor. Terms e_i correspond to the symmetry-adapted strains, where e_1 stands for the volumic, e_2 and e_3 to the deviatoric, and e_4, e_5 and e_6 to the shear strains[1].

Additionally, the entropy changes due to volume increments can also be approximated as [41]

[1] In terms of the strain tensor components:

$$e_1 = \frac{1}{\sqrt{3}}(\epsilon_{xx} + \epsilon_{yy} + \epsilon_{zz}), \quad e_2 = \frac{1}{\sqrt{2}}(\epsilon_{xx} - \epsilon_{yy}), \quad e_3 = \frac{1}{\sqrt{6}}(\epsilon_{xx} + \epsilon_{yy} - 2\epsilon_{zz}),$$
$$e_4 = \epsilon_{xy}, \quad e_5 = \epsilon_{yz}, \quad e_6 = \epsilon_{xz}$$

$$\Delta S_V = \left\langle \frac{\alpha}{\beta} \right\rangle \Delta V_t, \tag{1.17}$$

where α and β correspond to the thermal expansion and isothermal compressibility. Its proof is presented in Appendix A.

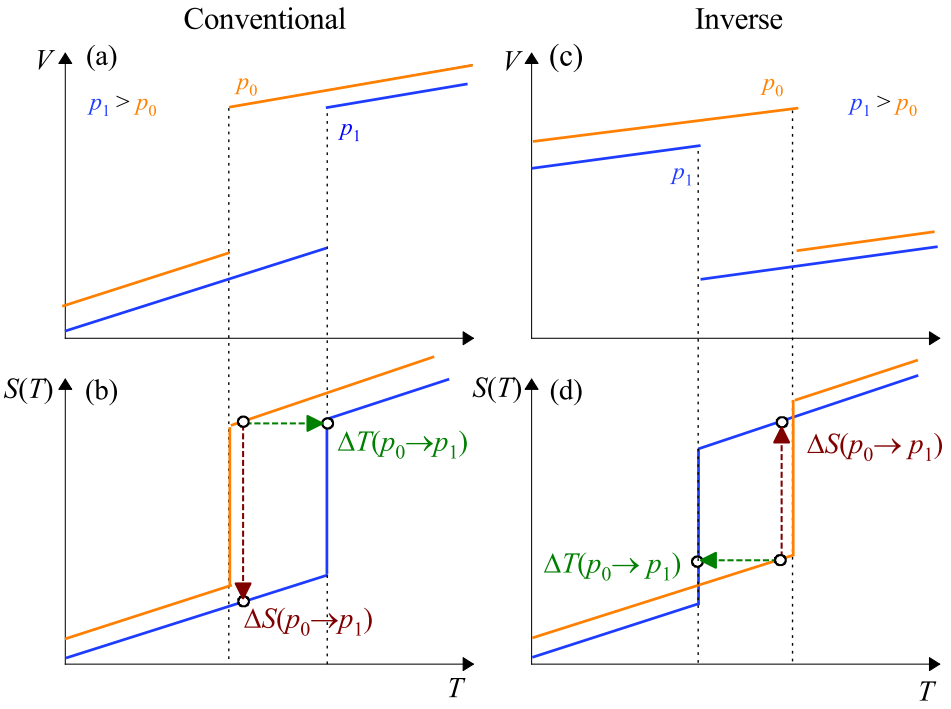

Figure 1.5: Conventional and inverse barocaloric effects are represented in left and right columns, respectively. Panels (a) and (c) display the volume evolution on temperature under isobaric conditions at p_0 (usually atmospheric pressure) and p_1, where $p_1 > p_0$. The corresponding entropy change in temperature is shown in panels (b) and (d) where the barocaloric effects upon applying pressure are indicated.

1.3 Determination of the barocaloric effects

In this section the methods to compute the barocaloric effects are introduced. These correspond to the direct, quasi-direct and indirect method. Thereafter, the implemented combination of the quasi-direct and indirect methods is further described along with the computation of the barocaloric effects.

1. **Direct methods**: They consist in methods whose outputs are directly the barocaloric effects themselves. More precisely, the isothermal entropy changes $\Delta S(T, p_0 \rightarrow p_1)$ are determined by means of calorimetry upon applying and removing pressure isothermally. This procedure provides the most reliable results, although the experimental setup can become complex since isothermal conditions and pressure changes are difficult to control. Likewise, the adiabatic temperature changes $\Delta T(S, p_0 \rightarrow p_1)$ require fast variations of the applied field which may be hard to perform [42, 43].

2. **Quasi-direct methods**: Calorimetry experiments are usually performed using quasi-direct methods since it may not be possible to have a good control of temperature when applying and removing the external field. This is why measurements are conducted keeping the pressure constant while heating and cooling the sample. Therefore, isobaric entropy changes at the phase transition are obtained as a function of temperature, and further analysis finally yields the barocaloric effects which are computed by isobaric entropy curves subtraction as $\Delta S(T, p_0 \rightarrow p_1) = S(T, p_1) - S(T, p_0)$ and $\Delta T(S, p_0 \rightarrow p_1) = T(S, p_1) - T(S, p_0)$. For this purpose, measurements with conventional and pressure-variable calorimeters are performed, Differential Scanning Calorimetry (DSC) or Differential Thermal Analysis (DTA). The quasi-direct method, which serves to determine the isobaric entropy curves and the corresponding barocaloric effects, will be explained in detail in the following section.

3. **Indirect methods**: They consist in obtaining the barocaloric effects using non-calorimetric nor thermometric measurements. For this purpose, by means of diffraction and dilatometry we first obtain the volume dependence with respect to temperature. Therefore, using equation $\Delta S(T, p_0 \rightarrow p_1) = -\int_{p_0}^{p_1} \left(\frac{\partial V}{\partial T}\right)_p dp$ and $\Delta T(S, p_0 \rightarrow p_1) = -\int_{p_0}^{p_1} \frac{T}{C_p} \left(\frac{\partial V}{\partial T}\right)_p dp$ (previously introduced in equation 1.7 and 1.8), the corresponding entropy and temperature changes driven by external field variations are computed. In our case this method is used when computing entropy changes out of the phase transition, and is performed as explained since our experimental setups do not

allow to directly obtain these entropy values caused by volume changes.

When performing measurements of heat flow with respect to temperature of a certain compound, a peak is observed when going through a first-order phase transition corresponding to either the release or absorption of the latent heat ΔH_{t}. As further explained in section 2.1, this value can be obtained by means of peak integration over temperature. Similarly, the entropy changes through the transition can also be obtained by means of peak integration as follows

$$\Delta S_{\mathrm{t}}(p) = \int_{T_1}^{T_2} \left(\frac{1}{T} \frac{\delta Q}{dT} \right) dT. \tag{1.18}$$

Temperatures T_1 and T_2 stand for the integration limits over its corresponding baseline. When we go from a lower to a higher temperature phase we experience an endothermic transition, which implies positive entropy changes ($\frac{1}{T} \frac{\delta Q}{|\delta T|} > 0$). Contrary, when going from a high to a low temperature phase we observe an exothermic transition with negative values of the entropy change ($\frac{1}{T} \frac{\delta Q}{|\delta T|} < 0$). Integrations have been performed using a custom software which yields the entropy evolution on temperature at constant pressure,

$$S(T') - S(T_{\mathrm{s}}) = \int_{T_{\mathrm{s}}}^{T'} \left(\frac{1}{T} \frac{\delta Q}{dT} \right) dT \tag{1.19}$$

where T' is an arbitrary temperature within the transition range, and T_{s} is the starting temperature. The cumulative entropy value results from the fraction of mass transformed during the phase transformation as $S(T') - S(T_{\mathrm{s}}) = \chi(T')\Delta S_{\mathrm{t}}$ (represented at Fig. 1.6b). Therefore, the fraction of mass transformed is written as

$$\chi(T') = \frac{S(T') - S(T_{\mathrm{s}})}{\Delta S_{\mathrm{t}}} = \frac{\displaystyle\int_{T_{\mathrm{s}}}^{T'} \left(\frac{1}{T} \frac{\delta Q}{dT} \right) dT}{\Delta S_{\mathrm{t}}}. \tag{1.20}$$

Apart from the aforementioned phase transition entropy changes, we also have to take into account the entropy variation out of the phase transition regime. In order to compute this variation we need first to recover the entropy differential

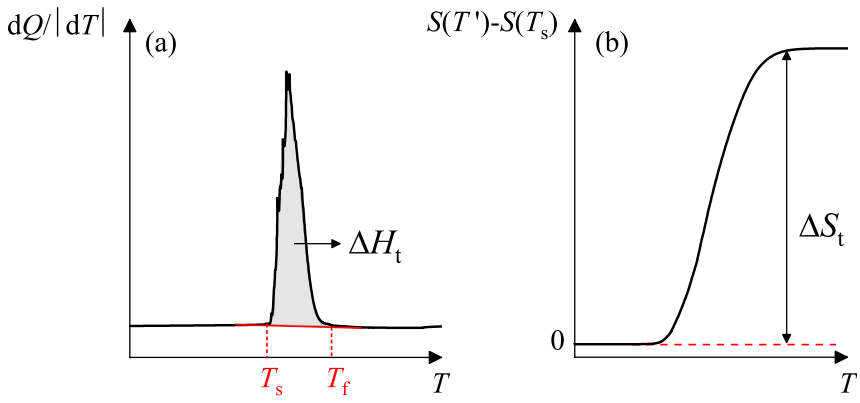

Figure 1.6: Panel (a) shows a representative Differential Scanning Calorimetry measurement where the peak integration is displayed, which corresponds to the latent heat (ΔH_t). The baseline is represented in red, along with the integration limits T_s and T_f. Panel (b) displays the corresponding entropy as a function of temperature through the phase transition.

expression with respect to T and p which reads

$$dS = \frac{C_p}{T}dT - \left(\frac{\partial V}{\partial T}\right)_p dp. \tag{1.21}$$

As the entropy is a function of state, entropy changes do not depend on the specific path but only on the initial and final states. A priori, as we conduct isobaric calorimetry runs, it would be desirable to compute the entropy variation also following isobaric paths. Under isobaric conditions ($dp = 0$), equation 1.21 reads

$$dS = \frac{C_p}{T}dT \quad \Rightarrow \quad \Delta S(T,p) = S(T,p) - S(T_0,p) = \int_{T_0}^{T} \frac{C_p}{T}dT, \tag{1.22}$$

where $S(T_0, p_{\mathrm{atm}})$ is the reference entropy at $T = T_0$, from which the isobaric entropy curves are computed. Nonetheless, heat capacity measurements are only obtained at atmospheric pressure, and consequently the entropy variation can only be well determined for an atmospheric pressure measurement $S(T, p_{\mathrm{atm}})$, where the temperature domain is defined by the temperature range of the experimental measurements of the heat capacity. In order to compute $S(T, p_{\mathrm{atm}})$ we have to consider the heat capacity of the low and high-temperature phases (C_p^{II} and C_p^{I}), and additionally, the fraction of mass transformed [$\chi(T)$] during the phase transition. With

the fraction of mass, we are allowed to compute the heat capacity value through the phase transition regime, which is written as $C_p^{\chi} = C_p^{\mathrm{II}}\chi(T) + C_p^{\mathrm{I}}(1-\chi(T))$. Therefore, considering the low and high-temperature phases regime, equation 1.22 for the entropy as a function of temperature at atmospheric pressure can be written as

$$S(T,p_{\mathrm{atm}})\text{-}S(T_0,p_{\mathrm{atm}}) = \begin{cases} \displaystyle\int_{T_0}^{T} \frac{C_p^{\mathrm{II}}}{T}\mathrm{d}T & T_0 \leq T \leq T_{\mathrm{s}} \\ \displaystyle\int_{T_{\mathrm{s}}}^{T} \frac{1}{T}\left(C_p^{\chi} + \frac{\delta Q}{dT}\right)dT & T_{\mathrm{s}} \leq T \leq T_{\mathrm{f}} \\ \displaystyle\int_{T_{\mathrm{f}}}^{T} \frac{C_p^{\mathrm{I}}}{T}\mathrm{d}T & T \geq T_{\mathrm{f}} \end{cases} \tag{1.23}$$

where the heat exchanged related with the latent heat $\left(\frac{\delta Q}{dT}\right)$ has also been incorporated, and T_{s} and T_{f} correspond to the start and finish transition temperatures respectively.

Contrary, under higher pressures ($p > p_{\mathrm{atm}}$), the pressure dependence of the heat capacity is generally not available, and therefore the entropy variation can not be directly computed using equation 1.23. However, making use of the definition of state function for the entropy, we are allowed to compute the entropy changes under pressure changes by going through isothermal paths. In order to do so, it is supposed that for $T \leq T_0$ the heat capacity is also pressure-dependent $[C_p(p)]$, and therefore, recovering equation 1.21, the entropy changes are computed following isothermal paths ($dT = 0$) as

$$dS = -\left(\frac{\partial V}{\partial T}\right)_p dp \quad \Rightarrow \quad \Delta S(T, p_{\mathrm{atm}} \to p_1) = -\int_{p_{\mathrm{atm}}}^{p_1}\left(\frac{\partial V}{\partial T}\right)_p dp. \tag{1.24}$$

If we consider $\left(\frac{\partial V}{\partial T}\right)_p$ to be non-pressure dependent, the entropy changes can finally be written as [28, 37]

$$\Delta S(T, p_{\mathrm{atm}} \to p_1) \approx -\left(\frac{\partial V}{\partial T}\right)_{p_{\mathrm{atm}}} (p_1 - p_{\mathrm{atm}})\,. \tag{1.25}$$

Therefore, at $T = T_0$ the high pressure entropy curves will be shifted according to the isothermal entropy changes of equation 1.25 (as represented in Fig. 1.7). The

assumption of non-pressure dependence of $\left(\frac{\partial V}{\partial T}\right)_p$ simplifies our calculations, since measurements of volume at atmospheric pressure are easily obtained by means of XRD or dilatometry.

Conversely, for $T > T_0$ the pressure dependence of the heat capacity is explored. The general expression may be written as

$$\left(\frac{\partial C_p}{\partial p}\right)_T = \frac{\partial}{\partial p}\left(\frac{\delta Q}{dT}\right)_p = \frac{\partial}{\partial p}\left(\frac{TdS}{dT}\right)_p = T\left(\frac{\partial^2 S}{\partial p \partial T}\right)_{T,p}. \tag{1.26}$$

From the Maxwell relation $\left(\frac{\partial S}{\partial p}\right)_T = -\left(\frac{\partial V}{\partial T}\right)_p$ it is derived that $\left(\frac{\partial^2 S}{\partial p \partial T}\right)_{T,p} = -\left(\frac{\partial^2 V}{\partial T^2}\right)_p$. Therefore, replacing this last expression into equation 1.26 we obtain [44]

$$\left(\frac{\partial C_p}{\partial p}\right)_T = -T\left(\frac{\partial^2 V}{\partial T^2}\right)_p. \tag{1.27}$$

From equation 1.27 it is deduced that when V is a linear function of T, the second derivative on temperature vanishes $\left(\partial^2 V/\partial T^2 \sim 0\right)$, and so the pressure derivative of the heat capacity $(\partial C_p/\partial p \sim 0)$. Consequently, if C_p is considered to be non-pressure dependent $C_p \neq C_p(p)$, we are allowed to use the atmospheric pressure measurements to compute the isobaric entropy runs at higher pressures since $C_p(p_{\mathrm{atm}}) = C_p(p_1)$, and thus equation 1.23 can be employed. Note that, as displayed in Fig. 1.7, when $\left(\frac{\partial V}{\partial T}\right)_p > 0$ the high-pressure entropy curves $S(T, p_1) - S(T_0, p_{\mathrm{atm}})$ will correspond to the atmospheric pressure curve $S(T, p_{\mathrm{atm}}) - S(T_0, p_{\mathrm{atm}})$ shifted to lower values of entropy (by the isothermal path performed at $T = T_0$), where the phase transition contribution is displaced according to dT/dp and including its corresponding transition entropy changes $\Delta S_{\mathrm{t}}(T', p_1) = \int_{T_{\mathrm{s}}}^{T'} \left(\frac{1}{T}\frac{\delta Q}{dT}\right) dT$. Contrary, when V is not a linear function of T, equation 1.27 states that C_p will be a function of pressure $C_p = C_p(p)$, and therefore the high-pressure entropy curves $S(T, p_1) - S(T_0, p_{\mathrm{atm}})$ will be computed considering the corresponding pressure dependence of the heat capacity into equation 1.23. The specific treatment of the heat capacity variation will be commented in detail for each compound studied in this thesis. Finally, once the isobaric entropy curves are computed, the barocaloric effects are obtained by means of curve subtraction as $\Delta S(T, p_{\mathrm{atm}} \rightarrow p_1) = S(T, p_1) - S(T, p_{\mathrm{atm}})$ and

$\Delta T(S, p_{\text{atm}} \rightarrow p_1) = T(S, p_{\text{atm}}) - T(S, p_1)$, resulting in a combination of the quasi-direct and indirect method.

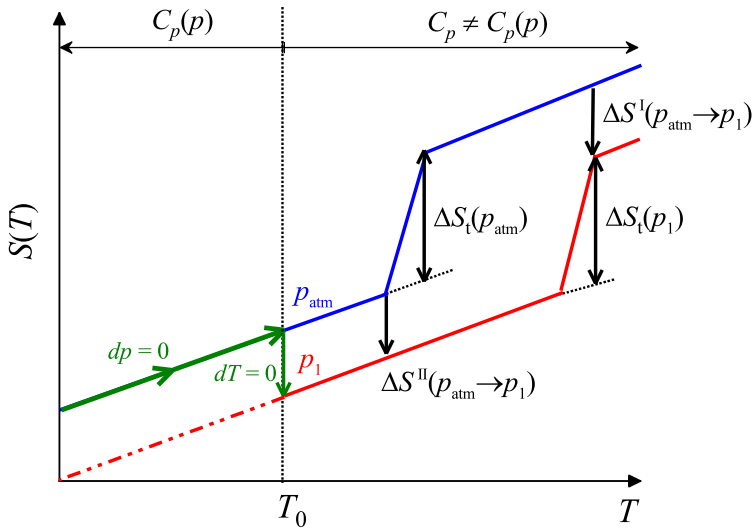

Figure 1.7: Representation of two isobaric entropy evolutions, where $p_1 > p_{\text{atm}}$. T_0 indicates the reference temperature. Above T_0 the C_p is considered to be not-pressure dependent. The isobaric and isothermal paths are shown with green lines, and the transition entropy changes as well as the isothermal entropy changes at the high and low-temperature phases are displayed.

It is important to emphasize that when computing the entropy changes following isothermal paths (equation 1.25) we will proceed differently when working with conventional or inverse barocaloric materials. If C_p presents similar values both in the high- and the low- temperature phases, the slope of the entropy curves in both phases will be similar (as represented in Fig. 1.7), and consequently $\Delta S_{\text{t}}(T, p_{\text{atm}}) + \Delta S^{\text{II}}(T, p_{\text{atm}} \rightarrow p_1) = \Delta S_{\text{t}}(T, p_1) + \Delta S^{\text{I}}(T, p_{\text{atm}} \rightarrow p_1)$, where $\Delta S^{\text{II}}(T, p_{\text{atm}} \rightarrow p_1)$ and $\Delta S^{\text{I}}(T, p_{\text{atm}} \rightarrow p_1)$ stand for the entropy changes computed by isothermal paths at low and high-temperature phases, respectively. Nonetheless, in general C_p exhibits different values in both phases, and as represented in Fig. 1.8 the slopes of the isobaric entropy curves will be different in the high- and low- temperature regimes. Consequently, the last mentioned equality must be rewritten as

$$\Delta S_{\text{t}}(T, p_{\text{atm}}) + \Delta S^{\text{II}}(T, p_{\text{atm}} \rightarrow p_1) \approx \Delta S_{\text{t}}(T, p_1) + \Delta S^{\text{I}}(T, p_{\text{atm}} \rightarrow p_1), \quad (1.28)$$

where the high and low-temperature entropy changes do not correctly fit with the transition entropy change. For this reason, when working with conventional materials the low-temperature entropy changes $\Delta S^{\mathrm{II}}(T, p_{\mathrm{atm}} \rightarrow p_1)$ and the corresponding transition entropy change $\Delta S_{\mathrm{t}}(p_1)$ will be used. Then, the high-temperature entropy change $\Delta S^{\mathrm{I}}(T, p_{\mathrm{atm}} \rightarrow p_1)$ will be determined according to equation 1.28, where its experimental value should be within the accepted error interval.

Conversely, for materials with inverse BCEs, the high-temperature entropy changes $\Delta S^{\mathrm{I}}(T, p_{\mathrm{atm}} \rightarrow p_1)$ and the corresponding transition entropy change $\Delta S_{\mathrm{t}}(p_1)$ will be used. Then, the low-temperature entropy change $\Delta S^{\mathrm{II}}(T, p_{\mathrm{atm}} \rightarrow p_1)$ will be determined according to equation 1.28.

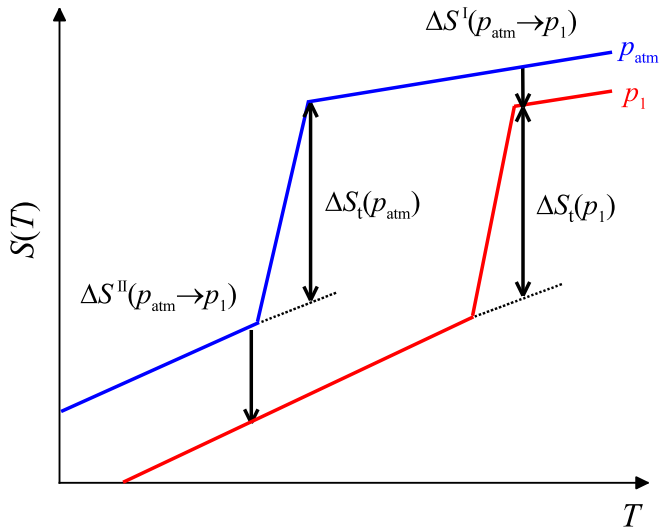

Figure 1.8: General representation of two isobaric entropy curves ($p_1 > p_{\mathrm{atm}}$) where $\Delta S^{\mathrm{II}}(p_{\mathrm{atm}} \rightarrow p_1) + \Delta S_{\mathrm{t}}(p_{\mathrm{atm}}) \neq \Delta S^{\mathrm{I}}(p_{\mathrm{atm}} \rightarrow p_1) + \Delta S_{\mathrm{t}}(p_1)$ due to the heat capacity effect.

1.4 Hysteresis and reversibility

The phenomenon of hysteresis is found in many areas of physics, and it is generally related with the delay of a response to an external stimulus [45]. More precisely, in solid-solid first-order phase transitions it is driven by the metastability upon cooling, and is also related with the energetic losses due to internal

friction. The transition mechanism is highly associated with hysteresis. In some cases, thermal fluctuations trigger the phase transition (isothermal transitions) and therefore, hysteresis depends on the temperature rate [46]. Contrary, it may be an intrinsic feature for other materials where diffusion does not prevail (athermal transitions) [47]. In this case the system is trapped in a local minimum until the external parameter forces the system to transform. Additionally, lattice imperfections such as dislocations or the non-uniformity of grain dimensions, act as separated nucleation points with independent activation energies that result in an heterogeneous nucleation. The nature of hysteresis will be further commented specifically for each material.

Hysteresis plays a major role when designing a refrigeration cycle involving a first-order phase transition. In Fig. 1.9 the phase diagram and the refrigeration cycle are displayed where the effect of hysteresis has been taken into account for a conventional and an inverse BC material. Additionally, notice that the phase transition occurs in a finite range which is defined by the start temperature T_s and the finish temperature T_f. We first consider a conventional BC material (see Fig. 1.9b) to be at the initial state (1) at atmospheric pressure p_{atm}. Then, the system is compressed adiabatically up to p_1 (2). Consequently, it increases its temperature following an isobaric path in order to thermalize at the hot sink temperature (3). Then, pressure is removed adiabatically to p_{atm} (4) and finally thermalizes at state (5). Note that due to hysteresis effects, once the first cycle is performed the final and initial states of the refrigeration cycle do not coincide, but they will match after further cyclability. At this point we define the *irreversible* BCEs as those obtained upon the first pressure change, and *reversible* BCEs as those obtained upon cyclic pressure changes.

It is important to point out that for conventional materials the transition induced by compression is exothermic (the phase with smaller volume is favored) and endothermic by means of decompressing (the phase with bigger volume is favored). In this regard, the coexistence line upon heating and decompression and upon cooling and compression coincide. For this reason, the irreversible BCEs upon compression (decompression) are computed using the cooling (heating) iso-

baric entropy curves. In the opposite way, for materials with inverse BCEs, the transition induced by compression (decompression) is endothermic (exothermic), and therefore the irreversible BCEs upon compression (decompression) are computed with heating (cooling) isobaric entropy curves.

As a result, barocaloric effects yield lower values when considering hysteresis. For this reason we will be interested in materials showing the lowest hysteresis values as possible in order to enhance the barocaloric performance.

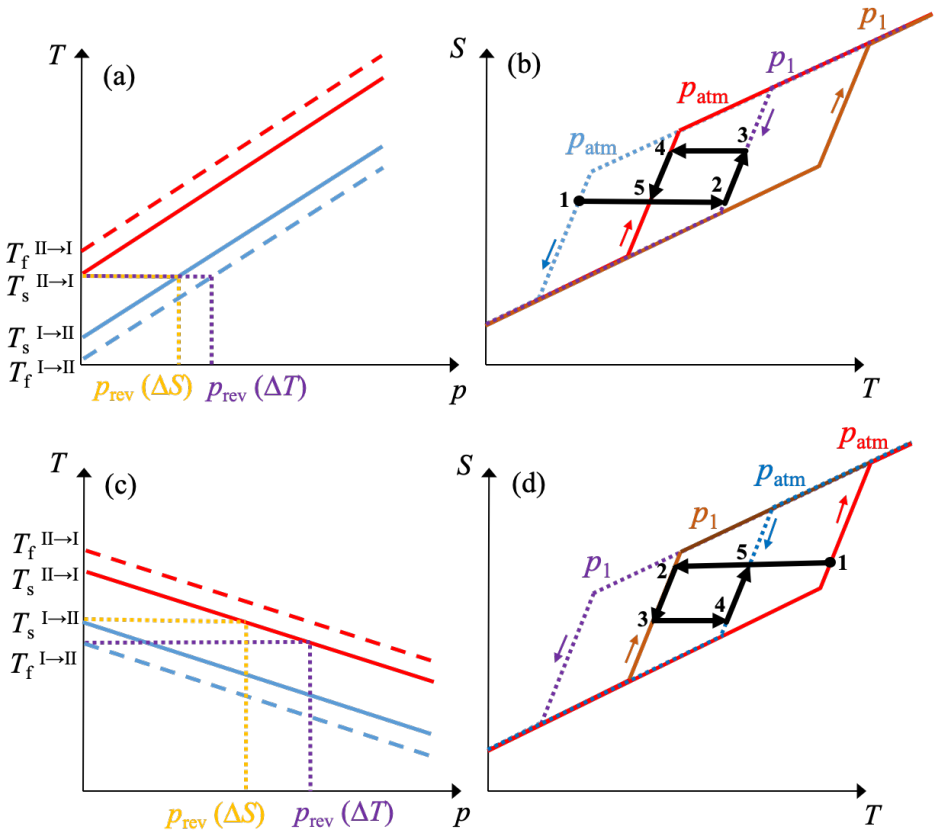

Figure 1.9: Panels (a,c) display the diagram phase for a conventional and inverse barocaloric material respectively, where T_s and T_f correspond to the start and finish transition temperatures. Blue and red lines stand for heating and cooling runs, and solid and dashed lines represent the start and finish coexistence curves. Panels (b,d) show the reversible refrigeration cycle for a conventional and inverse barocaloric material. Heating and cooling isobaric entropy runs are represented in solid and dashed lines respectively, where $p_{atm} < p_1$.

We pay special attention to the availability of running reversible refrigeration cycles upon the cyclic application and removal of hydrostatic pressure (counter-clockwise cycles in S-T diagram). In order to do so, for a conventional (inverse) barocaloric material, the cooling (heating) entropy run performed at higher pressures has to be shifted towards higher temperatures than the heating (cooling) entropy curve at atmospheric pressure (Fig. 1.9). Therefore, the corresponding reversible value for the isothermal entropy changes results from the following curves subtraction.

$$\Delta S_{\mathrm{rev}}(T, p_{\mathrm{atm}} \to p_1) = \begin{cases} S_{\mathrm{cool}}(T, p_1) - S_{\mathrm{heat}}(T, p_{\mathrm{atm}}) & \text{conventional} \\ S_{\mathrm{heat}}(T, p_1) - S_{\mathrm{cool}}(T, p_{\mathrm{atm}}) & \text{inverse} \end{cases} \tag{1.29}$$

where $p_1 > p_{\mathrm{atm}}$. Analogously for the adiabatic temperature changes

$$\Delta T_{\mathrm{rev}}(T, p_{\mathrm{atm}} \to p_1) = \begin{cases} T(S_{\mathrm{cool}}, p_1) - T(S_{\mathrm{heat}}, p_{\mathrm{atm}}) & \text{conventional} \\ T(S_{\mathrm{heat}}, p_1) - T(S_{\mathrm{cool}}, p_{\mathrm{atm}}) & \text{inverse} \end{cases} \tag{1.30}$$

where $S_{\mathrm{cool}}(T, p)$ and $S_{\mathrm{heat}}(T, p)$ stand for the isobaric cooling and heating entropy runs, respectively. Nonetheless, experimental results strongly suggest that reversible values of isothermal entropy changes performed by means of direct methods are obtained at lower pressures even when this last condition is not fulfilled (due to minor loops). Furthermore, this result matches with values obtained by the overlapping of the non-reversible barocaloric effects yielded upon the first application and removal of hydrostatic pressure [48–50]. We observe that the overlapping condition for ΔS_{rev} for a conventional (inverse) material (Fig. 1.10) is achieved when the start transition temperature for the heating (cooling) run at atmospheric pressure is smaller than the start transition temperature of the cooling (heating) run at higher pressures ($T_{\mathrm{s}}^{\mathrm{II}\to\mathrm{I}}(p_1) \geq T_{\mathrm{s}}^{\mathrm{I}\to\mathrm{II}}(p_{\mathrm{atm}})$ for conventional materials and $T_{\mathrm{s}}^{\mathrm{I}\to\mathrm{II}}(p_1) \geq T_{\mathrm{s}}^{\mathrm{II}\to\mathrm{I}}(p_{\mathrm{atm}})$ for inverse barocaloric materials). In the case of sharp transitions, where the phase transition has been induced almost isothermally, the reversible values obtained by both the overlapping and curve subtraction methods (equation 1.29) coincide [51].

With this in mind, the minimum required pressure changes to overcome hys-

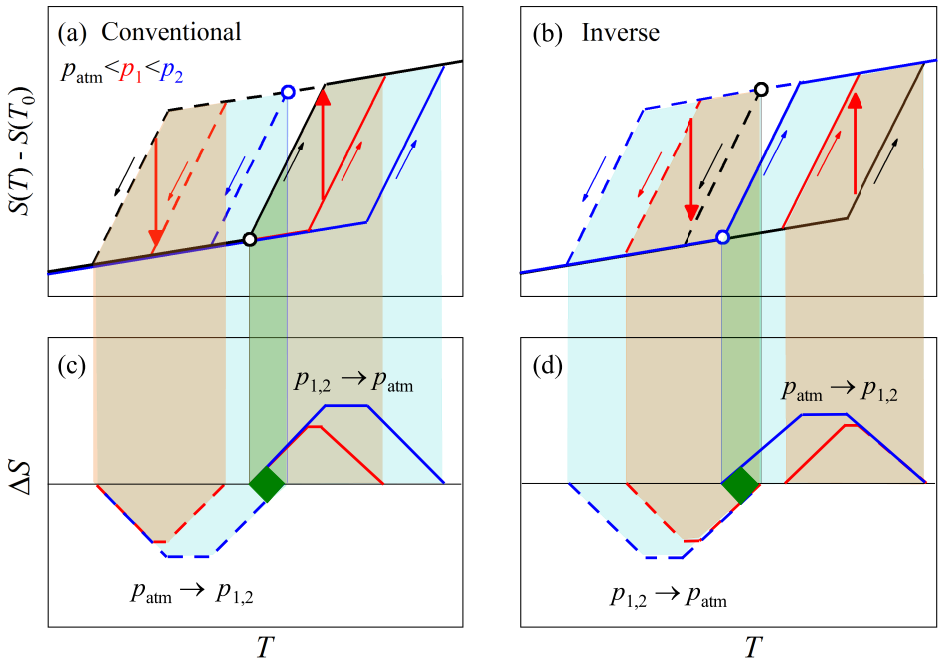

Figure 1.10: Left and right panels refer to conventional and inverse isothermal entropy changes, respectively. Panels (a) and (b) display the isobaric entropy curves showing the path to compute the isothermal entropy changes. In panels (c) and (d) the resulting reversible (area shaded in green) and non-reversible (areas shaded in orange and blue for pressure changes of $p_{atm} \rightleftarrows p_1$ and $p_{atm} \rightleftarrows p_2$) barocaloric effects are displayed [52].

teresis and to obtain reversible barocaloric effects can be directly obtained with the $T-p$ diagram, and are defined according to the following expression [52]:

$$p_{\mathrm{rev}}^{\Delta S}=\int_{T_{\mathrm{s}}^{\mathrm{I}\to\mathrm{II}}(p_{\mathrm{atm}})}^{T_{\mathrm{s}}^{\mathrm{II}\to\mathrm{I}}(p_{\mathrm{atm}})}\left(\frac{dT^{\mathrm{I}\to\mathrm{II}}}{dp}\right)^{-1}dT. \tag{1.31}$$

If $\left(\frac{dT^{\mathrm{I}\to\mathrm{II}}}{dp}\right)^{-1}$ is constant, equation 1.31 reads

$$p_{\mathrm{rev}}^{\Delta S}=\left(\frac{dT^{\mathrm{I}\to\mathrm{II}}}{dp}\right)^{-1}\Delta T^{\mathrm{II}\leftrightarrow\mathrm{I}}(p_{\mathrm{atm}}) \tag{1.32}$$

where $\Delta T^{\mathrm{II}\leftrightarrow\mathrm{I}}(p_{\mathrm{atm}})$ stands for the hysteresis at atmospheric pressure. Alternatively, reversible values for adiabatic temperature changes ΔT_{rev} are computed by entropy curve subtraction according to equation 1.30. Therefore, in this case the hysteresis effect needs to be completely overcome (Fig. 1.11). For a conventional (inverse) material, the start transition temperature for the heating (cooling) run at atmospheric pressure has to be smaller than the finish transition temperature of the cooling (heating) runs at higher pressures ($T_{\mathrm{s}}^{\mathrm{II}\to\mathrm{I}}(p_{\mathrm{atm}})<T_{\mathrm{f}}^{\mathrm{I}\to\mathrm{II}}(p_1)$ for conventional and $T_{\mathrm{s}}^{\mathrm{II}\to\mathrm{I}}(p_1)<T_{\mathrm{f}}^{\mathrm{I}\to\mathrm{II}}(p_{\mathrm{atm}})$ for inverse materials). For this reason, the minimum reversible pressure for the adiabatic temperature changes is written as

$$p_{\mathrm{rev}}^{\Delta T}=\int_{T_{\mathrm{f}}^{\mathrm{I}\to\mathrm{II}}(p_{\mathrm{atm}})}^{T_{\mathrm{s}}^{\mathrm{II}\to\mathrm{I}}(p_{\mathrm{atm}})}\left(\frac{dT^{\mathrm{I}\to\mathrm{II}}}{dp}\right)^{-1}dT. \tag{1.33}$$

Under ideal conditions in which the phase transition is conducted under fully isothermal transition, the start and finish temperatures will be equal $\left[T_{\mathrm{s}}^{\mathrm{I}\to\mathrm{II}}(p_{\mathrm{atm}})=T_{\mathrm{f}}^{\mathrm{I}\to\mathrm{II}}(p_{\mathrm{atm}})\right]$. Therefore, reversibility will be observed under the same minimum applied pressure for both ΔS_{rev} and ΔT_{rev}.

1.5 The refrigerant performance

Once the barocaloric effects of a certain material are analyzed, we will be interested in comparing to other materials' barocaloric performance in order to discriminate the most suitable compound or compound family. In this section several additional variables that will help us to make comparisons are introduced.

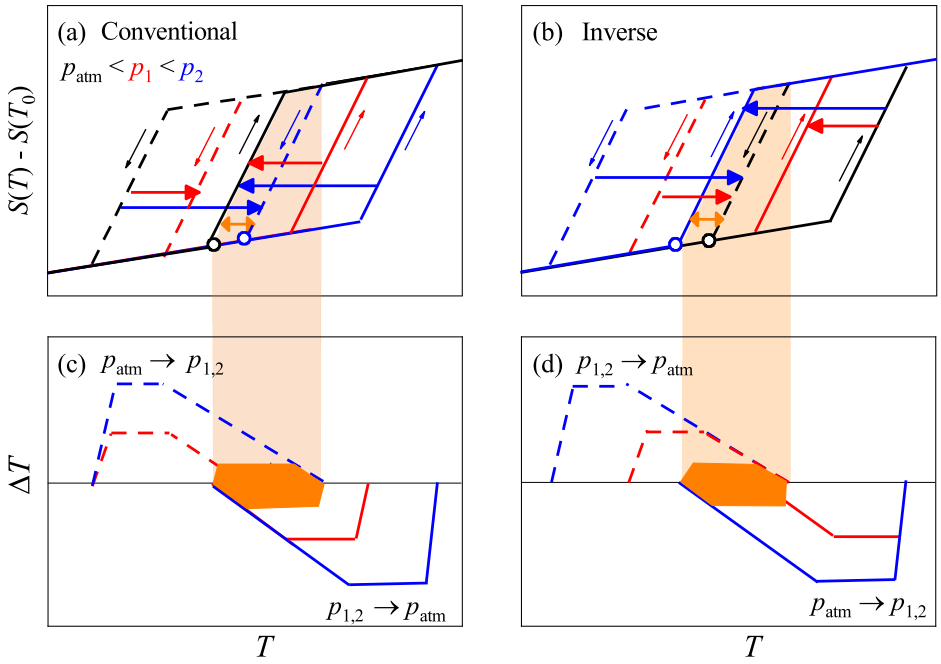

Figure 1.11: Left and right panels show the computation of conventional and inverse adiabatic temperature changes respectively. Panels (a) and (b) display the isobaric entropy curves respectively. In panels (c) and (d) the resulting reversible (area shaded in orange) and non-reversible barocaloric effects (dashed lines in red and blue for pressure changes of $p_{\mathrm{atm}} \rightleftarrows p_1$ and $p_{\mathrm{atm}} \rightleftarrows p_2$) are displayed [52].

1. **Values of $\Delta S_{\mathbf{max}}(p)$ and $\Delta T_{\mathbf{max}}(p)$**: They correspond to the maximum values of isothermal entropy changes and adiabatic temperature changes upon applying and removing pressure.

2. **Refrigerant capacity (RC)**: The definition of the RC is found to be unclear in the literature, and sometimes is confused with the Relative Cooling Performance (RCP) [30, 53]. In this thesis the RC is defined as follows

$$RC(p) = \Delta S_{\max}(p)\Delta T_{\mathrm{FWHM}}, \tag{1.34}$$

where $\Delta S_{\max}$ is the maximum isothermal entropy change driven by means of applying hydrostatic pressure, and ΔT_{FWHM} stands for the temperature span at full width at half maximum of the isothermal entropy change, which corresponds to the temperature difference between the cold and hot thermal sinks. This definition of the RC yields approximately $4W/3$ (where $W = \Delta S(p)\Delta T$ is the work applied to the refrigerant), at the same temperature span $\Delta T = \Delta T_{\mathrm{FWHM}}$, which gives an approximation of the heat exchanged in the refrigeration cycle [53].

3. **Coefficient of refrigerant performance (CRP)**: This value is similar to the coefficient of performance computed in motor and refrigeration cycles [54, 55]. Note that it also considers the work needed to drive the corresponding barocaloric effects. It is defined as

$$CRP(p) \sim \frac{\Delta S(p)\Delta T_{\mathrm{rev}}}{\frac{1}{2}p\Delta V_{\mathrm{t}}}, \tag{1.35}$$

where ΔT_{rev} corresponds to the reversible adiabatic temperature changes and the denominator is the applied work $W \sim \frac{1}{2}p\Delta V_{\mathrm{t}}$, where ΔV_{t} is the volume change across the phase transition [55, 56].

4. **Temperature span**: It is the temperature lapse where a certain minimum value of isothermal entropy changes or adiabatic temperature changes is observed (Fig. 1.12). We are interested in obtaining as higher values of T_{span} as possible at lower pressure.

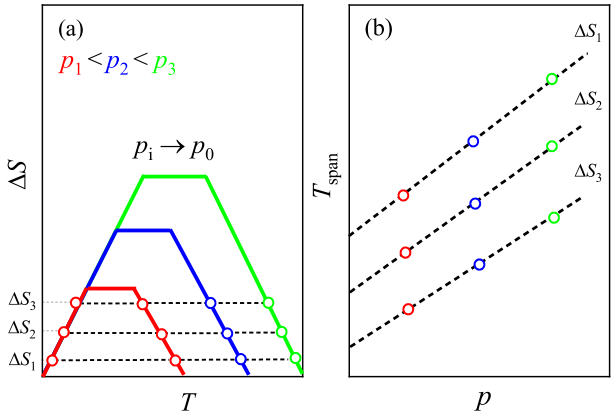

Figure 1.12: (a) Isothermal entropy changes when removing pressure from p_i to p_{atm}. The temperature span (T_{span}) required in order to achieve minimum values of ΔS is marked with empty dots. In figure (b) the temperature span at different pressures is represented. The dashed lines correspond to T_{span} values at constant ΔS.

At this point, we can define the main features that a proper barocaloric material must accomplish in order to present remarkable caloric effects.

1. High values of ΔH_t, ΔS_t and dT/dp, which also generally lead to high values of caloric effects ΔS and ΔT.

2. Low hysteresis in order to reduce losses and to obtain reversibility at lower pressures, that will demand smaller work to achieve.

3. Narrow transitions, otherwise the pressure needed to overcome the phase transition will be higher.

4. Transitions near room temperature, since air conditioning, fridges and freezers need a range of operation between $[255, 298]$ K. Additionally, materials with transitions above room temperature could also be implemented for refrigeration at higher temperatures, such as for industrial applications.

Other features are also taken into account, such as material degradation after cycling, thermal conductivity and density, which are essential when designing a prototype. It is also important to consider the abundance of a certain compound in nature or its feasibility to be synthesized. The materials fulfilling these

requirements have low production costs and therefore are economically affordable. Finally, toxicity is also a major feature to have in consideration, since the refrigeration technology is conceived to be near the human activity.

Chapter 2

METHODS

2.1 Differential Scanning Calorimetry

2.1.1 Conventional DSC

The Differential Scanning Calorimeter (DSC) measures the temperature difference between a certain sample and a reference as a function of temperature at p_{atm}. The ΔT is proportional to the differential heat flow [57, 58] as

$$\frac{\delta Q}{dt} \propto \Delta T, \tag{2.1}$$

and is computed by means of the proper calibration [59]. This technique is generally used to study phase transitions (first and second-order), glass transitions and, in general, any heat exchange process or any heat capacity change.

In a conventional heat-flux DSC (Fig. 3.12), the sample and reference are prepared into sealed aluminum pans and placed on the corresponding thermoelectric disks, that yield the sample and reference temperatures (T_{S} and T_{R} respectively). The pans are surrounded by the heating block that will be the responsible of the injection and removal of heat at a linear temperature controlled rate ($\frac{dT}{dt} = b$, which permits to convert the time scale into temperature scale). Consequently, as observed in Fig. 2.2, both sample and reference present parallel heating curves

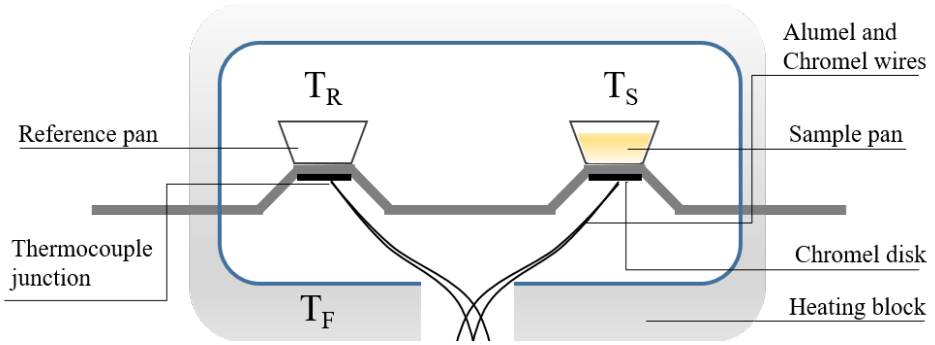

Figure 2.1: Cross-section of a DSC showing the encapsulated sample at temperature T_{S}, the reference pan at T_{R} and the temperature of the furnace or heating block written as T_{F}. The chromel and alumel wires, which consist the thermocouple, along with the constantan thermoelectric disk are also depicted.

until a phase transition is observed. In this case, the T_{S} is kept constant, while T_{R} keeps presenting a linear dependence. Once the phase transformation is completed, the T_{S} starts to increase again. Therefore, the temperature difference (ΔT) exhibits a calorimetric peak in the temperature range of a phase transition. In this thesis, endothermic transitions are defined with positive peaks and exothermic transitions by negative peaks.

DSC measurements were performed with a *Q100 Analyzer* from *TA Instruments* which operates between a temperature range of $T \in [183, 823]$ K and is able to run ramps with temperature rates between $\dot{T} \in [0.01, 20]$ K min^{-1}. The sample and reference atmosphere during measurements is controlled with purge gas (helium). The sample mass can reach values of several milligrams, and the aluminium pan weights approximately $\sim 50 - 60$ mg. The setup calibration depends on the specific DSC model. We employ an indium sample in order to calibrate enthalpy and temperature, and a sapphire disk to calibrate heat capacity measurements. The specific workflow is detailed in the manual [59].

In the following lines we will mathematically define the expression of the latent heat (ΔH_{t}) and transition entropy change (ΔS_{t}) with respect to the differential heat flow obtained from the DSC by means of equation 2.1. According to Ref. [60], the differential heat flow can also be written as

$$\frac{\delta Q}{dt} = \frac{dH}{dt} + (C_{p_{\mathrm{R}}} - C_{p_{\mathrm{S}}})\frac{dT}{dt}, \tag{2.2}$$

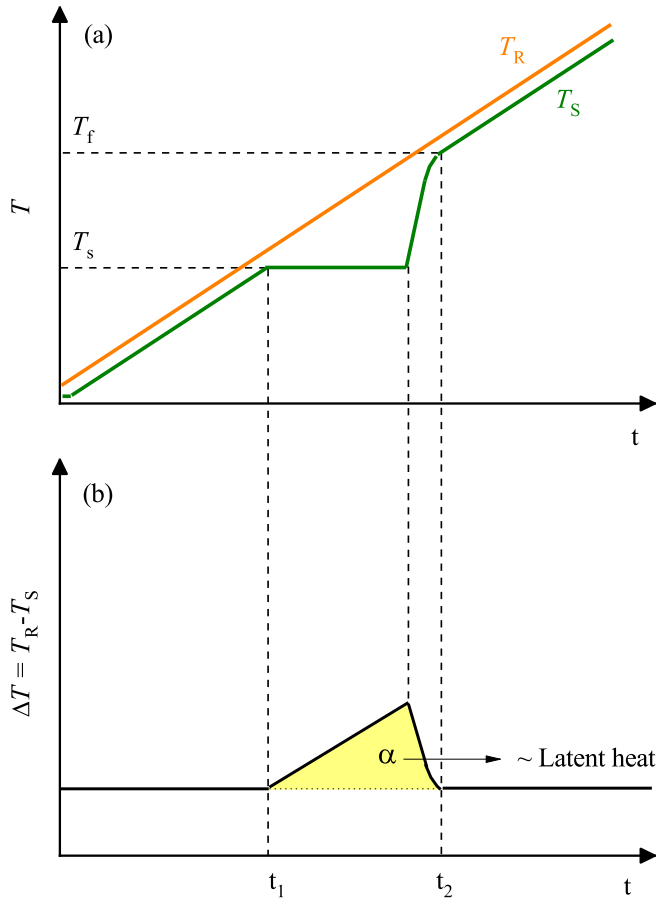

Figure 2.2: (a) Sample and reference temperatures evolution, where T_s and T_f stand for start and finish transition temperatures. (b) Differential temperature evolution, where the shaded area (α) is proportional to the latent heat of the phase transition. Times t_1 and t_2 stand for the corresponding times of the start and finish transition temperatures.

where C_{p_R} and C_{p_S} correspond to the heat capacities of the reference and sample respectively, dH/dt stands for the heat flow caused for the first-order phase transition (latent heat), and $\delta Q/dt$ is the differential heat flow obtained from the DSC. Therefore, after rewriting the heat flow expression as $\delta Q/dt = \dot{Q}/\dot{T}$, equation 2.2 can be written as

$$\frac{\delta Q}{dT} = \frac{dH}{dT} + (C_{p_R} - C_{p_S}). \tag{2.3}$$

From equation 2.3 we observe that out of the first-order phase transition the heat flow will differ from zero caused by the difference of heat capacities, and when going through the phase transformation we will observe the characteristic transition peak (Fig. 2.3). It is worth mentioning that the sensitivity and the calorimeter response can be associated with a small error for the start and peak transition temperatures (T_s and T_p) of approximately $\varepsilon(T) = \pm 1$ K. From integration of the calorimetric peaks, ΔH_t and ΔS_t can be determined. Only the first term of equation 2.3 will be integrated, which is the one corresponding to the transition peak. The enthalpy change is determined by the following equation, where the baseline contribution has been previously extracted

$$\Delta H_t = \int_{t_1}^{t_2} \frac{\delta Q'}{dt} \frac{1}{dT/dt} dt = \int_{T_1}^{T_2} \frac{\delta Q'}{dT} dT. \tag{2.4}$$

T_1 and T_2 correspond to the baseline temperature values of phase II and I respectively, which not necessarily refer to the start and finish transition temperatures, and $\delta Q'/dT$ corresponds to the heat flux once the baseline contribution has been extracted. Analogously, knowing that $dS = \delta Q_{rev}/T$, by means of peak integration we compute the entropy changes as

$$\Delta S_t = \int_{T_1}^{T_2} \frac{1}{T} \frac{\delta Q'}{dT} dT. \tag{2.5}$$

This value will be later employed to calibrate the high-pressure calorimetry integrations.

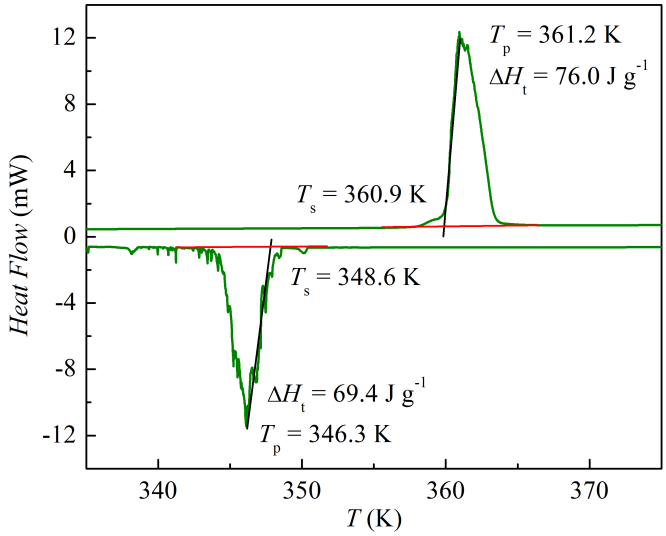

Figure 2.3: DSC thermogram showing the calorimetric peaks associated with a first-order phase transition. By means of peak integration the latent heat (ΔH_t) is derived. T_s and T_p and refer to the start and peak temperatures.

2.1.2 Modulated DSC

Modulated DSC (MDSC) is a technique aimed to measure the temperature dependence of the heat capacity. For this purpose, the furnace temperature will be programmed to change following a sinusoidal function in addition to the linear ramp $\frac{dT}{dt} = b$ defined in equation 2.6 [61, 62].

$$T = T_0(t = 0) + bt + B\sin(\omega t), \tag{2.6}$$

Parameter B corresponds to the temperature modulation amplitude and ω to the angular frequency. Values for B and ω are defined by the user when programming the calorimetric scan. Measurements in isothermal mode ($b = 0$) can also be performed, which in fact yield more reliable results. In Fig. 2.4a we observe the representation of both linear and sinusoidal temperature rates, and its corresponding derivatives in Fig. 2.4b. From equation 2.6 we determine that the temperature rate is defined as $dT/dt = b + B\omega\cos(\omega t)$, that after replacing it into equation 2.2

we obtain the following heat flux expression

$$\frac{\delta Q}{dt} = C_p(b + B\omega\cos(\omega t)) + \frac{dH}{dt}. \tag{2.7}$$

At this point, we will consider only the temperature range out of the phase transition regime. Therefore, no other thermal effects apart of the heat capacity will take place, and $\frac{dH}{dt} = 0$.

$$\frac{\delta Q}{dt} = C_p b + C_p B\omega\cos(\omega t). \tag{2.8}$$

This heat flow expression can be explained by two contributions, the *underlying* term which corresponds to the measurement taken from the conventional DSC, and the *periodic* term. From the amplitude of the periodic contribution $A = C_p B\omega$, which is computed by means of Fourier analysis, we finally obtain the heat capacity of a certain sample $C_p = \frac{A}{B\omega}$, which is usually referred as reversible heat capacity [63, 64]. Note that this last expression does not depend on the linear term used in the conventional DSC procedure, but only on the periodic contribution.

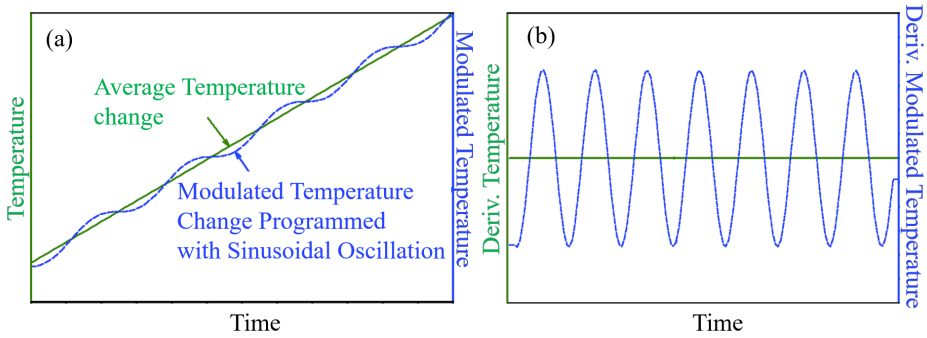

Figure 2.4: (a) Temperature evolution depending on time. The green line correspond to the linear heating rate and blue line to the modulated contribution. (b) Time derivatives of these linear and modulated rates. Modified from [65].

2.2 High Pressure Differential Thermal Analysis

As previously mentioned, we require from high-pressure differential thermal analysis (HPDTA) to finally obtain the barocaloric effects. In this section we in-

troduce the three high-pressure calorimeters used to perform our measurements. They are divided in two sections, the first one for calorimeters which operate up to 3 kbar at the high- and low-temperature regimes (A and B, respectively), and the second one for the calorimeter which operates up to 6 kbar (C). Both devices operate by means of Differential Thermal Analysis (DTA), which is the same procedure performed for DSC (in section 2.1) but, in this case the ΔT is not straightforward converted into heat flow, it is given directly in mV.

The sample is prepared in the same way for all calorimeters. It is placed inside a tin capsule which has been previously made by means of tin melting and moulding. Perfluorinated oil (Galden, Bioblock Scientist) is also inserted in order to avoid air bubbles. After introducing the sample into the corresponding calorimeter, the experimental measurements are performed by means of isobaric scans on temperature at a controlled rate. Additionally, there are other experimental features which are common for all calorimeters, such as the control of temperature (for calorimeters B and C) and pressure. In this case, they will only be specified in section 2.2.1.

2.2.1 3 kbar high-pressure calorimeters

In this section we will introduce the two calorimeters which operate up to pressure values of 3 kbar (A and B), which have been designed in our group. The sample is introduced into the high-pressure chamber allocated inside the calorimetric block, while another chamber is provided for the reference calorimetric signal. These both enclosures contain Bridgman-type chromel-alumel thermocouples, which record an electric voltage difference (ΔV) which is proportional to the temperature difference between sample and reference (Seebeck effect). Further calibration permits to relate ΔV as a function of temperature, pressure and time with the exchanged heat flow. More precisely, the thermocouple is inserted in a hole drilled in the tin capsule in order to improve the thermal contact. Nonetheless, this thermocouple needs a reference temperature to be compared with, for this reason a junction is set between the reference thermocouple and a dewar containing ice and water coexisting at the ice normal pressure melting temperature

($T = 273.15$ K).

In particular, the high-pressure calorimeter which operates in the high-temperature regime (A), allows measurements between nominally 0-3 kbar and $T \in [298, 473]$ K (a general sketch is represented in Fig. 2.5). Hydrostatic pressure is applied by means of a manual pump that compresses the pressure transmitting oil which flows into steel pipes to the sample cavity, which is typically *DW-Therm M90.200.02* (from Huber Kältemaschinenbau GmbH) or *Therm 240* (silicon oil from Lauda). Pressure is read by means of a pressure sensor attached to one of these capillars. Temperature is controlled with a resistor that surrounds the calorimetric block and is able to increase temperature at a certain defined rate. On the other hand, cooling is done by thermal contact with the ambient.

The other cell operating up to 3 kbar (B), works in the temperature range $T \in [200, 393]$ K with the help of circulating fluids through the thermal jacket surrounding the cell: *Kryo 85* or *Kryo 51* (from *Lauda*), with operating temperatures between $T \in [200, 303]$ K and $T \in [223, 393]$ K, respectively. The temperature is controlled by means of an external thermal bath (*Lauda Proline RP 1290*).

2.2.2 6 kbar high-pressure calorimeter

This high-pressure calorimeter allows to run measurements to pressures up to 6 kbar (C). This setup is equivalent to the 3 kbar calorimeter with the particularity that the calorimetric block (Cu-Be cell by Unipress, Poland) has been improved in order to support higher pressures (Fig. 2.7). Similarly to calorimeter B, it performs measurements between $T \in [188, 303]$ K and $T \in [223, 393]$ K. However, in this setup the differential voltage proportional to the heat flux is measured using Peltier modules (or thermopile) instead of thermocouples. As shown in Fig. 2.6 we attach the tin capsule to a Peltier module side, which is simultaneously in thermal contact with another Peltier module (which are connected by wired welded in opposition) by means of a piece of aluminium. Each Peltier module reads the difference in temperature between their both sides in terms of a differential electrical voltage. The voltage recorded by the reference and sample modules will be $V_\mathrm{r} \propto T_\mathrm{r} - T_\mathrm{aluminium}$ and $V_\mathrm{s} \propto T_\mathrm{s} - T_\mathrm{aluminium}$ respectively. Finally, the calorimetric output is

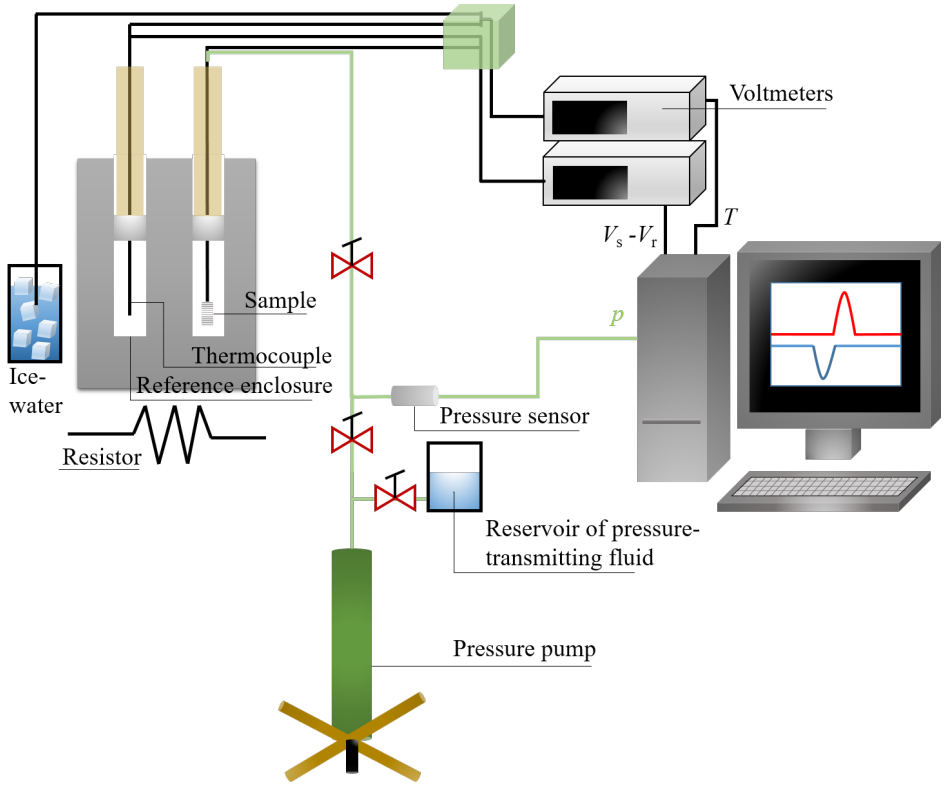

Figure 2.5: Sketch of the high temperature differential scanning calorimeter operating up to pressures of 3 kbar. The symbols V_r and V_s correspond to the voltage difference between reference and ice and water coexisting at 273.15 K and to the voltage difference between sample and reference, respectively. When performing measurements with the low-temperature calorimeter a thermal bath is employed in order to control temperature in place of the resistor. The black lines represent the electrical connections to the thermocouples which yield the differential temperature, and the green lines stand for the steel pipes from which the pressure transmitting fluid circulates to the sample cavity.

read as the differential voltage between sample and reference $\Delta V = V_s - V_r \propto T_s - T_r$, which by means of further calibration will be converted to heat flow. The block temperature is recorded using a Pt100 thermometer embedded at the bottom of the calorimeter. The reference temperature is measured using a *National Instruments USB 9162* connection instead of ice and water coexisting at $T = 273.15$ K.

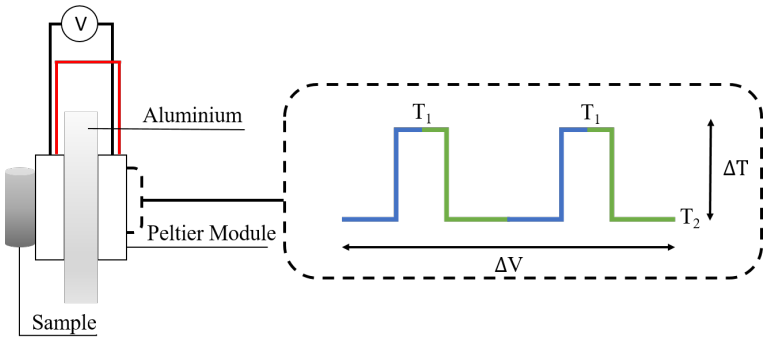

Figure 2.6: Sketch of a Peltier module. The right figure represents the internal structure which is formed by thermocouples attached in series. By means of thermal gradient, a voltage is induced between the ends of the thermocouple, which is proportional to this temperature difference.

As for the calorimeters introduced in section 2.2.1, the refrigerants used in the thermal bath are *Kryo 85* and *Kryo 51* (from *Lauda*), and the pressure transmitting fluid also corresponds to *DW-Therm M90.200.02* or *Therm 240*.

2.2.3 Setup Calibration

As aforementioned, DTA electric outputs depend on the temperature difference between sample and reference. The proportionality between this last differential temperature ($T_s - T_r$) and heat flow ($\dot{Q}$) depends on the setup susceptibility, which at the same time is related with the pressure transmitting fluid and the thermocouple thermal contact [66]. In this section we will present the calibration procedure for the specific case of the pressure transmitting fluid *Therm 240* (silicon oil), by which the electric output from DTA will be expressed in terms of heat flow. Other pressure transmitting fluids are calibrated similarly. First of all, we start by

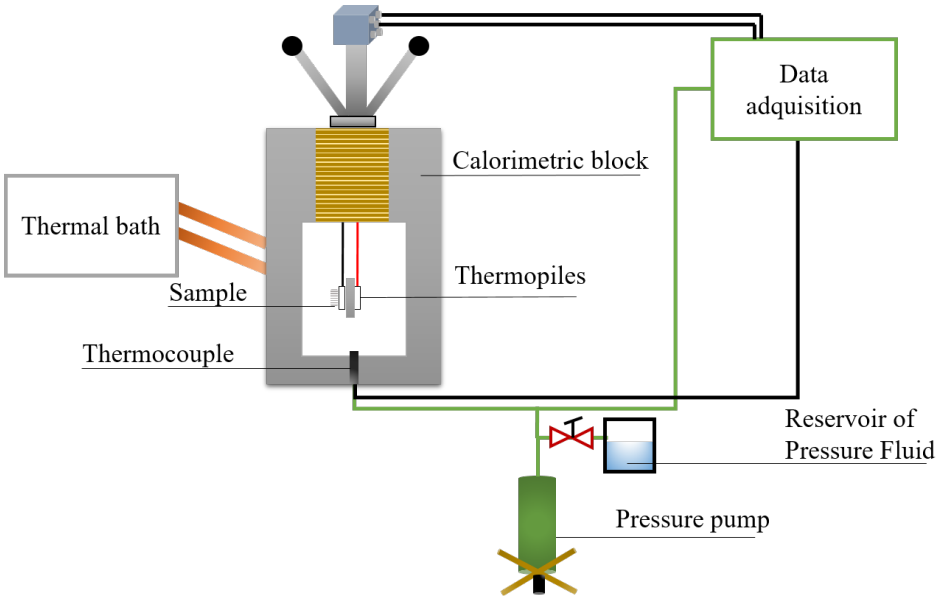

Figure 2.7: Sketch of the high-pressure cell which operates up to 6 kbar.

writing the electric output of the DTA as

$$\Delta V(p) = \sigma(p,T)\dot{Q}, \tag{2.9}$$

where $\Delta V(p)$ is the electric calorimetric signal and $\sigma(p,T)$ stands for the sensitivity of the calorimeter. In order to compute this expression, we carried out measurements with two samples with a well known calorimetric response. We performed measurements with Cu-Zn-Al and Cu-Ni-Al alloys which undergo a martensitic transition at $T = 325.0$ K and $T = 442.2$ K, respectively, with negligible volume changes. For these reason, they show non-pressure dependence of the transition temperature, enthalpy and entropy changes ($\mathrm{d}T/\mathrm{d}p = 0$, $\mathrm{d}(\Delta H_\mathrm{t})/\mathrm{d}p = 0$ and $\mathrm{d}(\Delta S_\mathrm{t})/\mathrm{d}p = 0$).

At this point we recorded DTA isobaric ramps upon heating and cooling of both samples, and computed the pressure-dependent peak integrations which are represented in Fig. 2.8. Considering that the latent heat must remain constant in the whole pressure range, we apply the following sensitivity correction

$$\bar{Y}(p) = \frac{Y(p)}{\sigma(p,T)}, \text{ where } Y(p) = \int_{T_1}^{T_2} \frac{\Delta V(p)}{\dot{T}} dT. \tag{2.10}$$

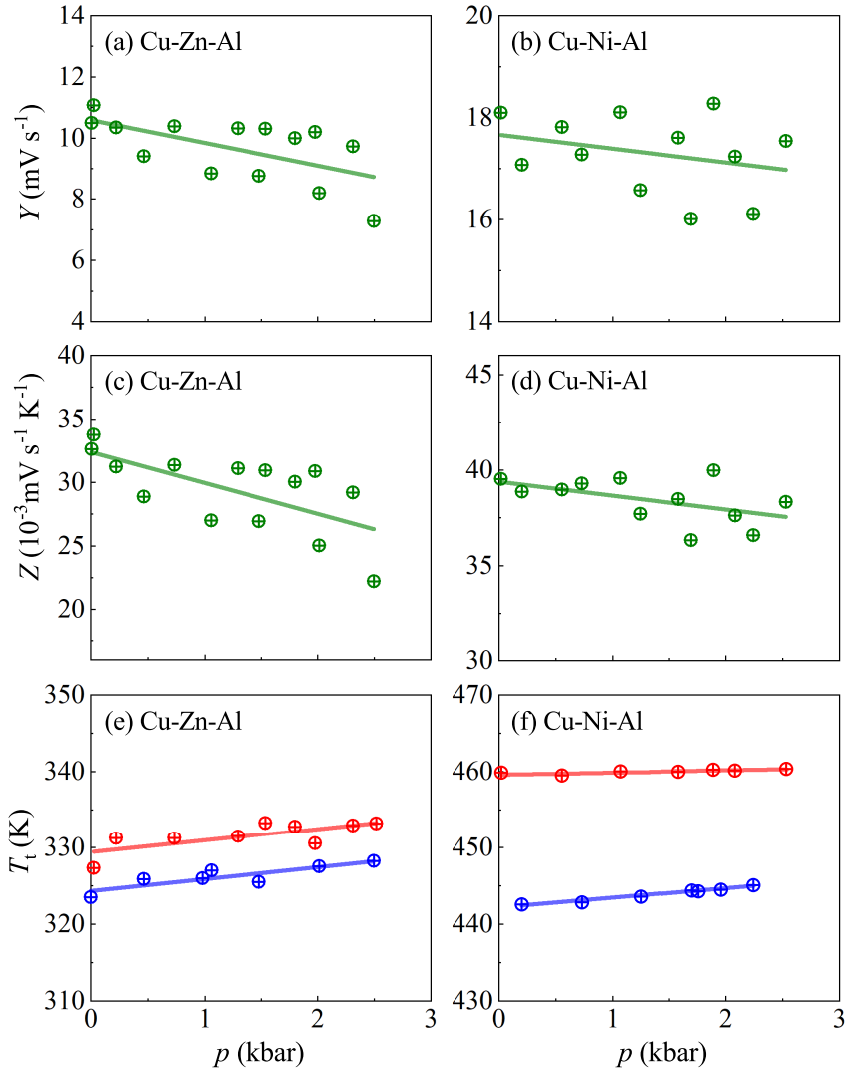

Figure 2.8: Left and right columns stand for Cu-Zn-Al and Cu-Ni-Al measurements. Plots (a,b) show the pressure dependence of the latent heat integration for the non-calibrated data. Panels (c,d) represent the entropy exchange integration. Red lines stand for the linear fits which clearly show a decreasing tendency. On the other side, figures (e,f) show the transition temperatures upon pressure. Red and blue empty dots represent heating and cooling runs respectively.

where $Y(p)$ stands for the peak integration between the transition temperature range defined by T_1 and T_2 at a certain pressure. The same procedure is carried out for the entropy integration, where the sensitivity correction is applied as follows

$$\bar{Z}(p) = \frac{Z(p)}{\sigma(p,T)}, \text{ where } Z(p) = \int_{T_1}^{T_2} \frac{\Delta V(p)}{T\dot{T}} dT. \tag{2.11}$$

The sensitivity is assumed to be a linear function of pressure as

$$\begin{aligned} \sigma(p,T)_Y &= A(T) + B(T)p \\ \sigma(p,T)_Z &= C(T) + D(T)p, \end{aligned} \tag{2.12}$$

where parameters $A(T)$, $B(T)$, $C(T)$ and $D(T)$ are also assumed to be linear with respect to temperature. Recall that $\bar{Y}(p)$ and $\bar{Z}(p)$ must remain invariant, therefore $\sigma(p,T)_Y \propto Y(p)$ and $\sigma(p,T)_Z \propto Z(p)$, where $Y(p)$ and $Z(p)$ differ for each alloy:

$$\begin{cases} Y(\text{Cu-Zn-Al}) = \text{-}7.46\ 10^{-4}p + 10.6 \\ Y(\text{Cu-Ni-Al}) = \text{-}2.87\ 10^{-4}p + 17.7 \end{cases} \tag{2.13}$$

$$\begin{cases} Z(\text{Cu-Zn-Al}) = \text{-}2.44\ 10^{-6}p + 0.0324 \\ Z(\text{Cu-Ni-Al}) = \text{-}7.29\ 10^{-7}p + 0.0394 \end{cases} \tag{2.14}$$

Therefore, using equations 2.13 and 2.14, we are able to write the following systems of equations considering that $A(T) = m+nT$, $B(T) = m'+n'T$, $C(T) = p+qT$ and $D(T) = p'+q'T$ corresponding to equations 2.15, 2.16, 2.17 and 2.18, respectively.

$$A(T) \rightarrow \begin{cases} m + 325.0n = 10.6 \\ m + 442.2n = 17.7 \end{cases} \tag{2.15}$$

$$B(T) \rightarrow \begin{cases} m' + 325.0n' = \text{-}7.46\ 10^{-4} \\ m' + 442.2n' = \text{-}2.87\ 10^{-4} \end{cases} \tag{2.16}$$

$$C(T) \rightarrow \begin{cases} p + 325.0q = \text{-}2.44\ 10^{-6} \\ p + 442.2q = \text{-}7.29\ 10^{-7} \end{cases} \tag{2.17}$$

$$D(T) \rightarrow \begin{cases} p' + 325.0q' = 0.0324 \\ p' + 442.2q' = 0.0394 \end{cases} \tag{2.18}$$

Finally, sensitivity is written as

$$\begin{cases} \sigma(T,p)_{\mathrm{Y}} = \text{-}9.1336 + 0.06068T + (\text{-}2.019\ 10^{-3} + 3.9177\ 10^{-6}T)p \\ \sigma(T,p)_{\mathrm{Z}} = 0.02527 + 1.6135\ 10^{-5}T + (\text{-}1.081\ 10^{-6} + 1.8965\ 10^{-9}T)p \end{cases}$$

Combining $\sigma(T,p)_{\mathrm{Y}}$ and $\sigma(T,p)_{\mathrm{Z}}$ with equations 2.10 and 2.11, we are able to obtain the enthalpy and entropy integrations ($\bar{Y}(p)$ and $\bar{Z}(p)$, respectively) calibrated according to the setup sensibility. After that, we will finish the calibration by reescaling the value of the atmospheric pressure integration with the one previously obtained with DSC. In other words, we will impose that $\Delta H(0) = \Delta H_{\mathrm{DSC}}$ and $\Delta S(0) = \Delta S_{\mathrm{DSC}}$. Therefore, the final expression for the integration calibration reads

$$\Delta H_{\mathrm{t}}(p) = \frac{\Delta H_{\mathrm{DSC}}}{\bar{Y}(0)}\bar{Y}(p) \quad \text{and} \quad \Delta S_{\mathrm{t}}(p) = \frac{\Delta S_{\mathrm{DSC}}}{\bar{Z}(0)}\bar{Z}(p). \tag{2.19}$$

As a matter of fact, most DTA measurements have been performed using *DW-Therm M90.200.02* as a pressure transmitting fluid. It has been proved, in this case, that there is no pressure effect on the calorimetric measurements, and therefore there is no need to correct neither $Y(p)$ nor $Z(p)$. Only the DSC calibration will be required.

2.3 Dilatometer

Dilatometry is an experimental technique which allows to determine the equation of state, and whose measurements are performed by means of a dilatometer. The dilatometer used to perform our measurements was first build at Bochum

(Germany) and finally improved in our group (Grup de Caracterització de Materials, UPC), and can only be used for samples which melt at $T < 473$ K.

As shown in Fig. 2.9, the sample is introduced into a stainless steel cylinder by means of a syringe, since the solid sample has been previously melted in order to avoid bubbles inside the cavity. The cylinder, which has a Bridgman piston in one side and is hermetically closed using a screw on the other side, is later placed inside the calorimetric block. The Bridgman piston is attached to a ferromagnet which is set inside a coil. Consequently, by means of compression and decompression, the ferromagnet will move down and up inside the coil respectively. As defined by the Faraday law, the change of magnetic flux inside the coil caused by the ferromagnet movement, will induce an electric voltage ΔV, which will be later expressed in terms of volume. As for the high-pressure DTA, temperature will be controlled by a *Lauda* thermal bath, using *Kryo 51* and *Kryo 85* as refrigerants circulating inside the calorimetric block. We also set a thermocouple inside a dewar containing ice and water in coexistence. Therefore it will measure the ice melting temperature as the reference value ($T = 273.15$ K), which will be compared with the one read by another thermocouple attached to the calorimetric block. Pressure is applied by means of a manual pump reaching values between $p \in [0, 3]$ kbar, where the same refrigerant is used as a pressure transmitting fluid, and circulates to the chamber inside the calorimetry block through steel capillaries. Finally, measurements are performed by means of isothermal ramps of pressure upon applying and removing pressure. The voltage measurements will be later calibrated to volume values, previously obtained by means of XRD at atmospheric pressure, and consequently we will be able to obtain pressure-volume-temperature (p-V-T) diagrams.

2.4 X-ray powder diffraction

X-ray powder diffraction (XRPD) measurements were performed in order to obtain the cell parameter variation as a function of temperature. In general, with the peak intensity refinement the lattice structure can also be obtained. Nonetheless, if the crystal structure is known, the peak position will be sufficient to extract

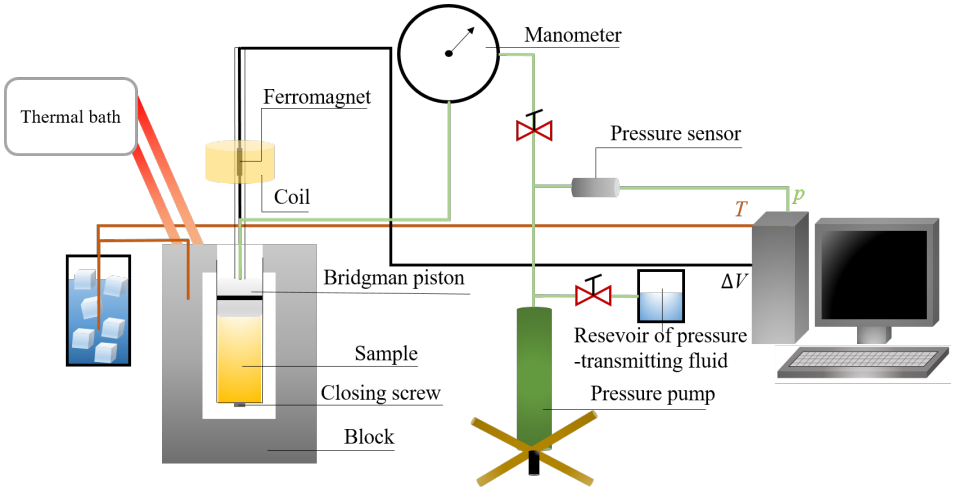

Figure 2.9: Sketch of the dilatometer setup. The black, orange and green lines represent the voltage, temperature and pressure connections.

the lattice parameters. From the lattice parameters the transition volume change and the unit cell volume are straightforwardly computed. Consequently, its dependence with temperature at atmospheric pressure $\left(\frac{\partial V}{\partial T}\right)_{p_{\text{atm}}}$ is obtained, which is needed in equation 1.7. A conventional diffractometer is basically composed of an X-ray source and a detector. X-rays are generated from a cathode. Once they are generated, they are filtered to obtain monochromatic light, which will be collimated in order to properly focus the beam to hit the sample. The incident radiation is transmitted resulting in a constructive interference for specific angle positions (θ). A constructive interference is observed at a certain position θ by the detector (higher intensity of photons per second) when the Bragg's law is satisfied ($n\lambda = 2d\sin\theta$, where n is an integer, d the inter-planar distance and θ the diffracted angle). The Bragg's law relates the diffracted angles with the radiation wavelength λ and the inter-planar distance d. The inter-planar distance can finally be related with the crystallographic structure of the sample under study.

XRPD experiments have been performed in different Research Institutions, that will be specified for each particular sample. However, for most of the samples under analysis here, these experiments have been carried out using the X-Ray diffractometer of the Group of Characterization of Materials where this thesis has been carried out. In the X-ray diffractometer available in our laboratory, X-

rays are generated with a copper anode where the $K\alpha_1$ radiation (corresponding to a wavelength of $\lambda = 1.54056$ Å) has been selected by means of a quartz monochromator. The setup is mounted with a Debye-Scherrer geometry which implies a transmission mode, where the sample is prepared inside capillaries with 0.1–0.5 mm diameter. The measured range of the scattered radiation is between $2\theta \in [4°, 120°]$ with a step of 0.029°, and captured by an INEL Cylindrical Position-Sensitive detector (CPS120). Temperature is controlled by means of a nitrogen flux in a *700 Cryostream* cooler from Oxford Cryosistems, with an operating range of $T \in [90,\ 500]$ K.

2.5 Synchrotron X-ray diffraction

We performed synchrotron X-ray Diffraction (SXRD) measurements in order to obtain the unit cell parameters variation following isobaric and isothermal paths. Our measurements were carried out at ALBA synchrotron (Cerdanyola del Vallès, Catalunya) at the Material Science Powder Diffraction (MSPD) beamline. In a synchrotron, electrons are accelerated inside the ring with energies up to several GeV. According to Larmor equation, any charged particle radiates when accelerated. In synchrotron facilities the direction of electron beams are changed, consequently a centripetal acceleration causes the electron to move in a circular orbit and to emit radiation. This emitted radiation can be fine tuned in order to have X-rays with an specific wavelength, which will be later directed towards the corresponding beamline and to the sample to be analyzed [67]. For conventional diffractometers with a copper anode, X-rays with $\lambda \cong 1.54$ Å wavelength are generated. Nonetheless, in synchrotron facilities we are able to reach values of $\lambda = 0.4246$ Å due to the high energies at which the electrons are accelerated (of 3 GeV). The main advantage of SXRD in front of conventional XRPD is that better resolution is achieved for a smaller 2θ range thanks to the detectors farther position.

The sample is prepared inside a diamond anvil cell (DAC) with cullet size between 0.4–0.7 mm. Additionally, sodium chloride (NaCl), strontium tetraborate (SrB_4O_7) or ruby ($Cr_xAl_{2-x}O_3$ where $x \sim 0.05$) are also added as pressure

markers as exemplified in Fig. 2.10. Regarding NaCl, the experimental pressure inside the DAC is checked by introducing in its equation of state the temperature value, and the (200) peak position[1]. Upon applying pressure, the fluorescence peak ($\lambda_0 = 694.76$ nm and $\lambda_0 = 685.37$ nm at atmospheric pressure for ruby and strontium tetraborate, respectively) will shift towards higher wavelengths. As this shift is properly calibrated, we can indirectly know the pressure value inside the DAC. Temperature is controlled using a resistor surrounding the gasket, and a thermocouple is attached near the diamond cell. A cryostat is set instead of the resistor when performing low-temperature measurements.

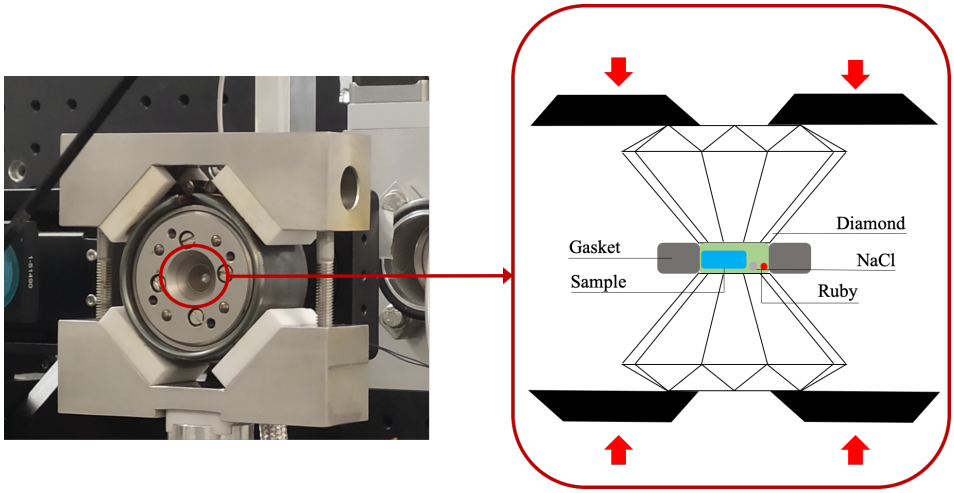

Figure 2.10: The left figure shows the ALBA Diamond Anvil Cell. The right sketch represents the same DAC where the sample and pressure marker positions are depicted.

[1] http://kantor.50webs.com/diffraction.htm

Chapter 3

PLASTIC CRYSTALS

3.1 Introduction

Plastic crystals are polymorphic compounds, generally with pseudo-globular molecular shapes, which present a high-temperature positionally ordered and orientationally disordered phase, which is also referred to as *plastic phase* (hereafter phase I) [68]. It owes its name to the high plasticity observed when permanent deformations are caused after applying low stresses [69, 70]. In fact, the plastic phase is a mesophase between solid and liquid due to its orientational disorder. Nonetheless, it presents the mechanical properties of the solid phase. By cooling down from the plastic phase, a first-order phase transition is observed where molecules evolve to well defined orientations while the lattice experiments a decrease in symmetry (hereafter phase II). This phase is also referred as the *solid phase*. In Fig. 3.1 a solid-solid phase transition of a plastic crystal is outlined.

As a consequence of the orientational disorder observed in the plastic phase, the energy released when melting is small since it mainly comes from the positional order-disorder contribution of the crystal lattice. However, plastic crystals show particular high values of entropy changes in the solid-solid transformation in comparison with the ones obtained in the melting point, and in some cases may have a colossal value. The giant values of transition entropy changes observed for some

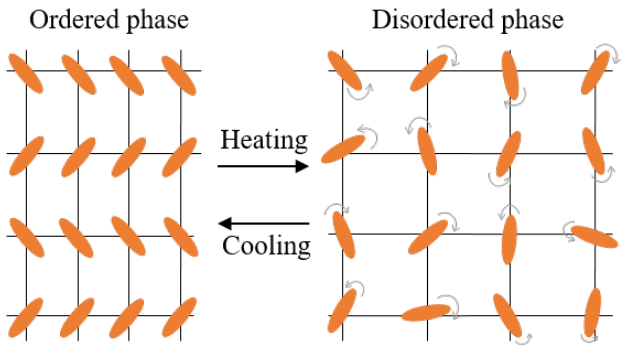

Figure 3.1: Sketch of a plastic crystal phase transition.

plastic crystals encouraged the further study of their barocaloric response. As introduced in section 1.2, this entropy change depends on the ratio of configurations of the plastic (N_{I}) and solid phase (N_{II}), and is written as $\Delta S = \mathrm{RM}^{-1}\ln(N_{\mathrm{I}}/N_{\mathrm{II}})$. For most of the plastic crystals studied in this thesis, it can be reasonably assumed that $N_{\mathrm{II}} = 1$, since in most of the cases the strength of hydrogen bonding does not allow molecular disorder [71]. Nonetheless, plastic crystals sometimes present disorder in phase II (i.e. $N_{\mathrm{II}} > 1$) [72–74]. They generally display a high-simmetry lattice in the plastic phase (fcc, bcc or rombohedral). Consequently, the high symmetry of the crystallographic site implies a reorientational dynamic of the molecule that, although, pseudo-globular in shape, does not fulfill the symmetry elements of the site.

In this chapter we present the barocaloric results of seven plastic crystal compounds, which are organized in two subfamilies, adamantane and neopentane derivatives.

3.2 Neopentane derivatives

Neopentane is an organic compound widely used in industry, for example as a gasoline blending agent in manufacturing plastic and cosmetics [75, 76]. It belongs to the alkane group ($\mathrm{C_nH_{2n+2}}$), and it is build by a double carbon branch (methyl radicals) in the second carbon position forming a tetrahedral shape. According to the IUPAC, it is also named 2,2-dimethylpropane with chemical formula $\mathrm{C_5H_{12}}$

(Fig. 3.2). The plastic crystal compounds studied in this section are neopentane derivatives in which one or more methyl groups have been replaced by amino and/or hydroxyl radicals.

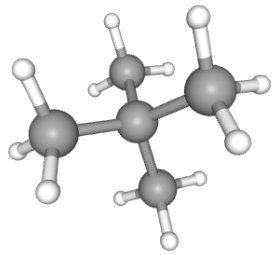

Figure 3.2: 3D neopentane molecule. Grey and white spheres stand for carbon and hydrogen atoms respectively [76].

3.2.1 Tris(hydroxymethyl)aminomethane (TRIS)

TRIS is a tetrahedral organic molecule which corresponds to the short name of Tris(hydroxymethyl)aminomethane with chemical formula $(NH_2)C(CH_2OH)_3$. This compound is in fact a direct pentaerythrytol derivative $[C(CH_2OH)_4]$, from where methyl groups of neopentane have been replaced for hydroxymethyl groups (-CH_2OH). Then, TRIS is obtained by replacing an hydroxymethyl by an amino group (-NH_2) as shown in Fig. 3.3.

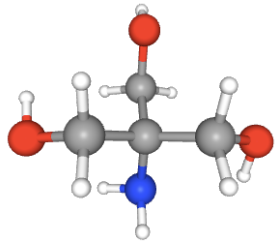

Figure 3.3: TRIS molecule in 3D. Grey, white, red and blue spheres stand for carbon, hydrogen, oxygen and nitrogen atoms respectively [77].

At phase II, the low-temperature stable phase, TRIS is arranged in an orientationally ordered orthorhombic lattice with space group $Pn2_1a$ and four molecules per unit cell ($Z = 4$) [78, 79]. Molecules are located forming layers perpendicular to the c axis in which strong intermolecular hydrogen bonds between hydroxyl groups are present. Contrary, layers are interconnected by weak hydrogen bonds

between hydroxyl and amino groups. Upon heating, at $T_t^{II \to I} = 407$ K, TRIS undergoes a first-order phase transition towards an orientationally disordered bcc lattice with Im3m space group and two molecules per unit cell ($Z = 2$). During the transformation, planes perpendicular to the c axis increase their distance to finally arrange in a cubic lattice, where the molecules also realign [80]. The corresponding lattice parameters are summarized in Table 3.1.

TRIS has biochemical and pharmaceutical applications. On one hand, it is used as a buffer solution to keep a stable pH, such as in DNA extraction [81]. On the other hand, it is also prescribed for correcting metabolic acidosis [82].

Phase II (293 K)	Phase I (408 K)
orthorhombic ($Pn2_1a$)	bcc (Im3m)
a = 8.853(3) Å	
b= 7.804(3) Å	a = 6.888(8) Å
c= 8.800(3) Å	Z = 2
Z = 4	

Table 3.1: Lattice parameters of TRIS for phases I and II [78].

3.2.2 2-amino-2-methyl-1,3-propanediol (AMP)

AMP, the short for 2-amino-2-methyl-1,3-propanediol, is an organic compound with chemical formula $(NH_2)(CH_3)C(CH_2OH)_2$ presenting a tetrahedral shape. It is a neopentane derivative in which three methyls have been replaced by one amino and two hydroxyl radicals as represented in Fig. 3.4.

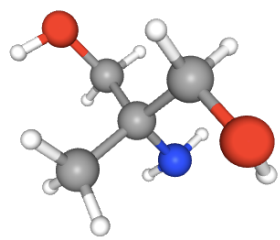

Figure 3.4: AMP molecule in 3D. White, gray, red and blue stand for hydrogen, carbon, oxygen and nitrogen atoms respectively [83, 84].

At the low-temperature (phase II), AMP is arranged in a monoclinic structure

with $Z = 4$ (space group not reported in literature) where molecules present fixed orientations. Upon heating, at $T_t^{II \to I} = 351$ K molecules rearrange into an orientationally disordered bcc lattice with space group $Im\bar{3}m$ and $Z = 2$. Crystallographic data are summarized in Table 3.2.

AMP is used in cosmetics manufacturing [85, 86], also as a buffer in a gel for electrophoresis separation of peptides [87, 88].

Phase II (293 K)	Phase I (358 K)
monoclinic a = 8.62 Å b = 11.00 Å c = 6.10Å β = 93.53 ° Z = 4	bcc ($Im\bar{3}m$) a = 6.76(2) Å Z = 2

Table 3.2: Lattice parameters of AMP at solid and plastic phases [89].

3.2.3 Pentaglycerine (PG)

The plastic crystal PG stands for 2-hydroxymethyl-2-methyl-1,3-propanediol (or pentaglycerine) with a chemical formula of $(CH_3)C(CH_2OH)_3$ and a molecule with tetrahedral shape. It is synthesized by means of replacing three neopentane methyl groups by hydroxymethyl groups (Fig. 3.5). At phase II, the low-temperature stable phase, PG is arranged as an ordered body-centered tetragonal lattice with space group $I\bar{4}$ and two molecules per unit cell ($Z = 2$). Upon heating, at $T_t^{II \to I} = 375.5$ K it displays a first-order phase transition towards an orientationally disordered fcc structure with $Fm\bar{3}m$ space group and four molecules per unit cell (Z = 4).

In phase II, PG molecules are ordered in layers perpendicular to the c axis which are strongly linked by means of hydrogen bonds. Contrary, layers are weakly interconnected by means of van der Waals forces [78, 91]. Upon increasing temperature the perpendicular planes to [001] increase their distance gradually transforming into the plastic phase. In Table 3.3 the crystallographic data is summarized.

PG it is mainly used in industry for the manufacturing of coats, varnishes and

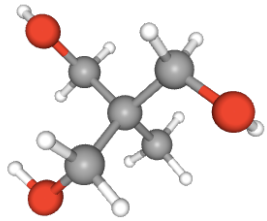

Figure 3.5: PG molecules in 3D, where white, grey and red stand for hydrogen, carbon and oxygen atoms respectively [90].

polyester resins among others [92, 93].

Phase II (298 K)	Phase I (363 K)
tetragonal ($I\bar{4}$)	fcc ($Fm\bar{3}m$)
a = 6.052(2) Å	a = 8.876(8) Å
c = 8.872(3) Å	Z = 4
Z = 2	

Table 3.3: Lattice parameters of PG at solid and plastic phases [83].

3.2.4 Neopentyl alcohol (NPA)

NPA is a plastic crystal with chemical formula $(CH_3)_3C(CH_2OH)$ also known as neopentyl alcohol (2,2-dimethyl-1-propanol). It is synthesized by means of replacing one methyl group by an hydroxyl radical (Fig. 3.6) in neopentane. In the low-temperature phase (phase II), NPA presents an orientationally ordered triclinic lattice with four molecules per unit cell ($Z = 4$). Upon heating, at $T_t^{II\to I} = 235.4$ K, it exhibits a first-order phase transition where phase II evolves towards an orientationally disordered fcc structure with $Fm\bar{3}m$ space group and four molecules per unit cell (Z = 4). In Table 3.4 the crystallographic data for both high and low-temperature phases are summarized. NPA is a compound widely used for pharmaceutical purposes [94].

3.2.5 Neopentylglycol (NPG)

NPG with chemical formula $(CH_3)_2\,C\,(CH_2OH)_2$ is a plastic crystal also referred to as neopentylglycol (2,2-dimethylpropane-1,3-diol). It is a direct deriva-

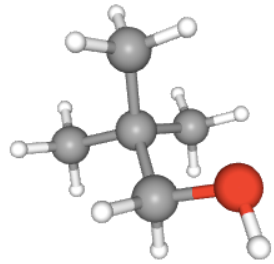

Figure 3.6: NPA molecules in 3D, where white, gray and red correspond to hydrogen, carbon and oxygen atoms respectively [95].

Phase II (233.3 K)		Phase I (293 K)
triclinic (Unknown)		fcc ($Fm\bar{3}m$)
a = 10.304(10) Å	$\alpha = 90.14(6)°$	
b = 10.418(9) Å	$\beta = 99.51(3)°$	a = 8.815 Å
c = 11.398(12) Å	$\gamma = 107.08(6)°$	
Z = 7		Z = 4

Table 3.4: Crystallographic parameters of NPA [96].

tive from neopentane where two methyl groups have been substituted for two hydroxymethyl groups (Fig. 3.7). At room temperature, NPG presents a completely ordered phase II where the crystal is arranged in a monoclinic structure with $P2_1/c$ space group and four molecules per unit cell ($Z = 4$). Upon heating, at $T_t^{II \to I} = 314$ K, phase II evolves towards an orientatinoally disordered phase where molecules form an fcc lattice with 4 molecules per unit cell ($Z = 4$) and $Fm\bar{3}m$ space group. Further crystallographic information is summarized in Table 3.5. Additionally, NPG has a wide use as an additive in paints, lubricants and cosmetics [97–99].

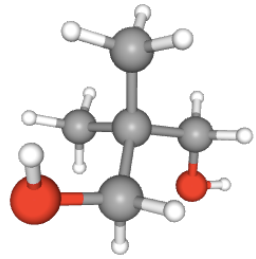

Figure 3.7: NPG molecule in 3D where white, gray and red spheres stand for hydrogen, carbon and oxygen atoms respectively [100].

Phase II (310 K)	Phase I (320 K)
monoclinic ($P2_1/c$)	fcc ($Fm\bar{3}m$)
a = 5.9820(7) Å	
b = 10.9125(12) Å	a = 8.8293(4) Å
c = 10.8444(9) Å	
β = 113.168(9)°	
Z = 4	Z = 4

Table 3.5: Crystallographic parameters of NPG [28].

3.3 Adamantane derivatives

Adamantane is an hydrocarbon with chemical formula $C_{10}H_{16}$ which is composed by three cyclohexane rings providing the molecule a cage-like structure (Fig. 3.8). The crystal structure at room temperature is present as a fcc with $Z = 4$ [101]. In this work, the barocaloric effects of 1- and 2- adamantanol will be reported, which consist in adamantane derivatives where an hydrogen atom has been respectively replaced by a -OH in the tertiary carbon and the secondary carbon in position 2 according to the numeration system of Ref.[102]. Adamantane and some derivatives present medical applications such as in prophylaxis, as an antiviral and for Parkinson treatment [103–105].

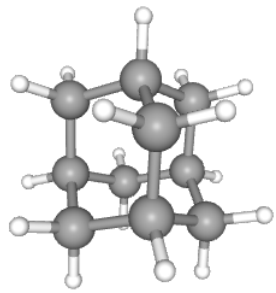

Figure 3.8: Adamantane molecule in 3D. White and black spheres represent carbon and hydrogen atoms respectively [106].

3.3.1 1-adamantanol

As aforementioned, 1-adamantanol (hereafter refered to as 1-ada-ol), also named 1-hydroxyadamantane is an adamantane derivative with chemical formula $C_{10}H_{16}O$ (Fig. 3.9a). This molecule presents a cage structure where the vertices positions are occupied by carbon atoms. At room temperature, phase II of 1-ada-ol presents an orientationally ordered tetragonal lattice with space group $P4_2/n$ and eight molecules per unit cell ($Z = 8$). According to [107], this phase II in fact presents certain disorder in the hydrogen bonding between hydroxyls. Upon heating, at $T_t^{II \to I} = 362$ K, it exhibits a first-order phase transition towards an orientationally disordered cubic structure with F43c space group and four molecules per unit cell ($Z = 4$). In Table 3.6 the crystallographic data at both high and low-temperature phases are summarized.

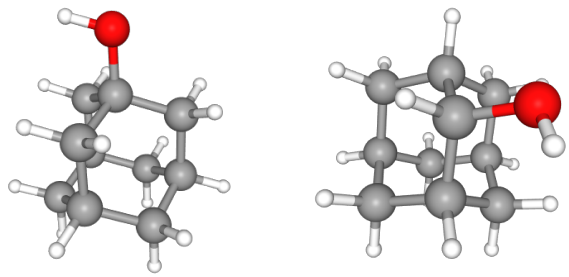

(a) (b)

Figure 3.9: 3D structure of (a) 1-ada-ol and (b) 2-ada-ol [108, 109]. Gray, white and red spheres stand for carbon, hydrogen and oxygen atoms respectively.

Phase II (320 K)	Phase I (420 K)
tetragonal ($P4_2/n$)	fcc (F43c)
a = 15.888(9) Å	a = 9.800(2) Å
c = 6.881(5) Å	Z = 4
Z = 8	

Table 3.6: Crystallographic parameters of 1-ada-ol. Data obtained by means of XRD.

3.3.2 2-adamantanol

The plastic crystal 2-adamantanol (hereafter refered to as 2-ada-ol), also named as 2-hydroxyadamantane and with chemical formula $C_{10}H_{16}O$ is synthesized by replacing the hydrogen atom placed at position 2 of the adamantane molecule, by a -OH (Fig. 3.9b). From room temperature up to the melting, 2-ada-ol presents 3 solid phases. The low-temperature solid-phase (phase III), is arranged in a triclinic structure with $Z = 6$. Upon heating, we observe a first-order phase transition with small latent heat of $\Delta H_t^{III \to II} = 2.0$ J g^{-1} [110]. Phase II presents an orientationally ordered monoclinic lattice with $Z = 12$. Upon further heating, 2-ada-ol exhibits another first-order phase transition towards an orientationally disordered cubic lattice with $Z = 4$ (space group F$\bar{4}$3m) [111], and with enthalpy changes of $\Delta H_t^{II \to I} = 24.6$ J g^{-1}. We decided to explore the barocaloric effects only in the vicinity of II $\rightleftarrows$ I solid-solid phase transition since it presents higher values of enthaphy change. In Table 3.7, 2-ada-ol crystallographic data are summarized.

Phase III (325 K)	$a = 11.657(4)$ Å $b = 11.668(5)$ Å $c = 11.664(5)$ Å	$\alpha = 81.243(3)°$ $\beta = 70.541(3)°$ $\gamma = 61.045(3)°$	triclinic $Z = 6$
Phase II (387.2 K)	$a = 11.797(2)$ Å $b = 20.426(3)$ Å $c = 11.816(2)$ Å	$\beta = 109.598(6)°$	monoclinic $Z = 12$
Phase I (396.4 K)	$a = 9.667(2)$ Å		fcc $Z = 4$ (F$\bar{4}$3m)

Table 3.7: Crystallographic parameters of 2-ada-ol. Data obtained by means of XRD

3.4 Results

Powdered samples of TRIS ($\leq$ 99.8 % purity), PG (99 %), NPA (99 %) and 2-ada-ol (97 %) were purchased from Sigma Aldrich, and AMP ($\geq$ 99.5 %) and 1-ada-ol (99 %) from Fluka, and used as received.

XRPD and DSC measurements

XRD measurements were performed in order to obtain the volume variation with respect to temperature (Fig. 3.10). All the plastic crystals studied in this thesis present positive transition volume changes upon heating, therefore conventional barocaloric effects are expected. Heat capacity measurements at atmospheric pressure are shown in Fig. 3.11 and summarized in Table 3.8.

DSC measurements were performed at different temperature rates (Fig. 3.12) for TRIS, AMP, PG, NPA and NPG, and at $\dot{T} = 2$ K min^{-1} for 1- and 2-ada-ol. The $T_{\mathrm{s}}^{\mathrm{II}\rightarrow\mathrm{I}}$ remains approximately invariant while the $T_{\mathrm{f}}^{\mathrm{II}\rightarrow\mathrm{I}}$ increases with the temperature rate. Additionally, thermal hysteresis slightly varies with temperature rate. Notice that the exothermic transition of AMP is not observed. Nonetheless, after cyclic implementation of temperature scans the endothermic transition is noticed, therefore AMP must have conducted the I $\rightarrow$ II transformation at some point although it is not observed in DSC scans. Hysteresis values of $\sim$ 73 K,$\sim$ 12 K, $\sim$ 25 K, $\sim$ 13 K, $\sim$ 11 K, $\sim$ 0.5 K are observed for TRIS, PG, NPA, NPG, 1- and 2-ada-ol at $\dot{T} = 2$ K min^{-1}, respectively.

High-pressure DTA measurements

High-pressure DTA (HP-DTA) measurements were performed with the high-pressure calorimeter A for TRIS, AMP, PG, 1- and 2-ada-ol, and with calorimeter B for NPA and NPG (Fig. 3.13). In this case, HP-DTA measurements for AMP show the cooling transition peaks.

The phase diagrams are derived from the high-pressure calorimetric peaks (Fig. 3.14). Considering hysteresis and values of $\frac{dT_{\mathrm{t}}}{dp}$ obtained from the phase diagrams, reversibility can be evaluated. In this case, the large value of thermal hysteresis from TRIS and APM make them useless for barocaloric applications.

From peak integration, values of enthalpy and entropy changes at the transition are obtained (Fig. 3.15 and 3.16). As expected from volume measurements, TRIS, AMP and PG have small pressure dependence of enthalpy and entropy changes at the transition, while values for NPA, NPG, 1- and 2-ada-ol considerably decay

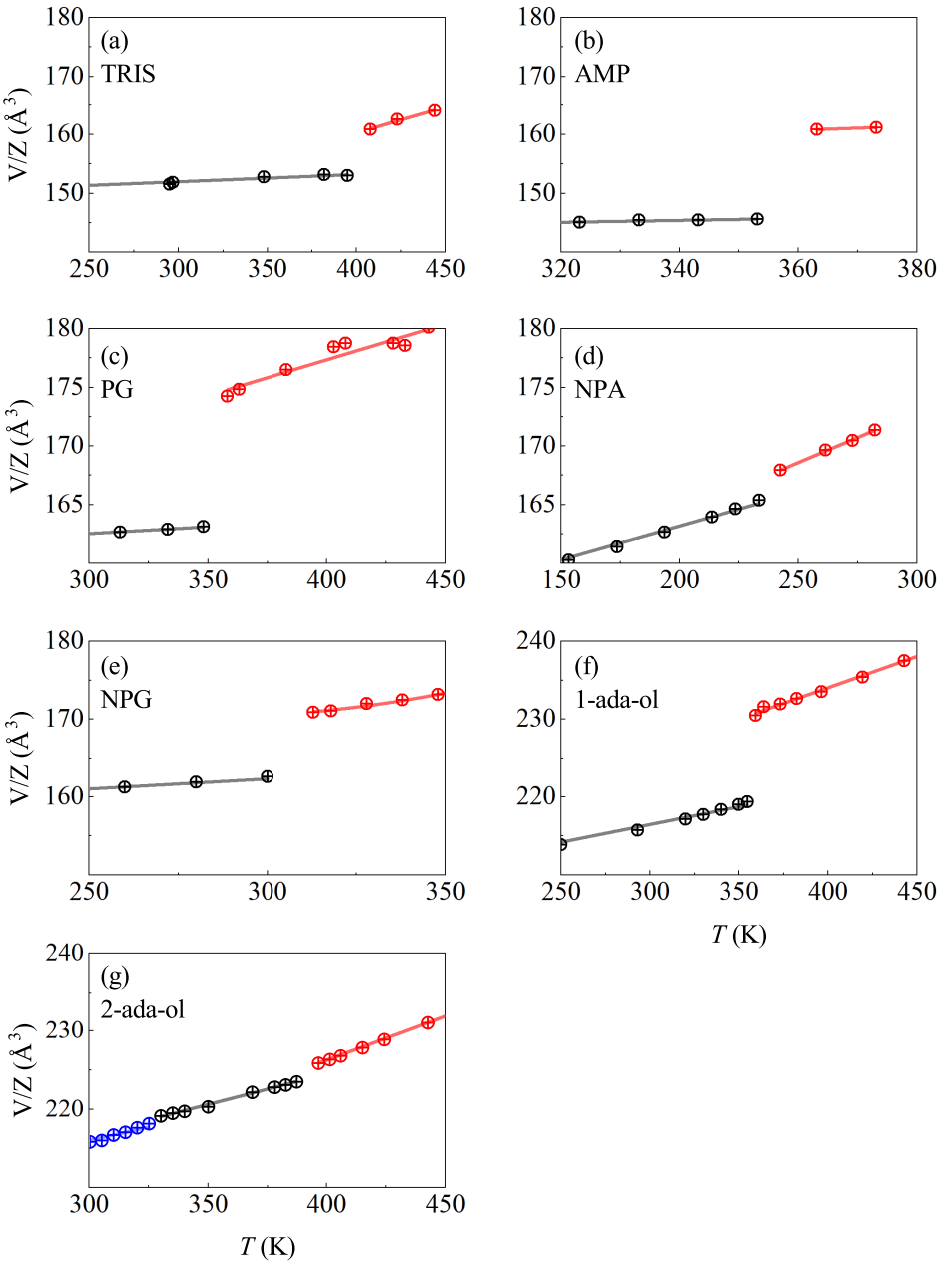

Figure 3.10: Unit cell volume evolution in temperature of TRIS[80], AMP [112], PG (computed from [113]), NPA (computed from [114]), NPG, 1-ada-ol and 2-ada-ol. Red, black and blue stand for phases I, II and III respectively.

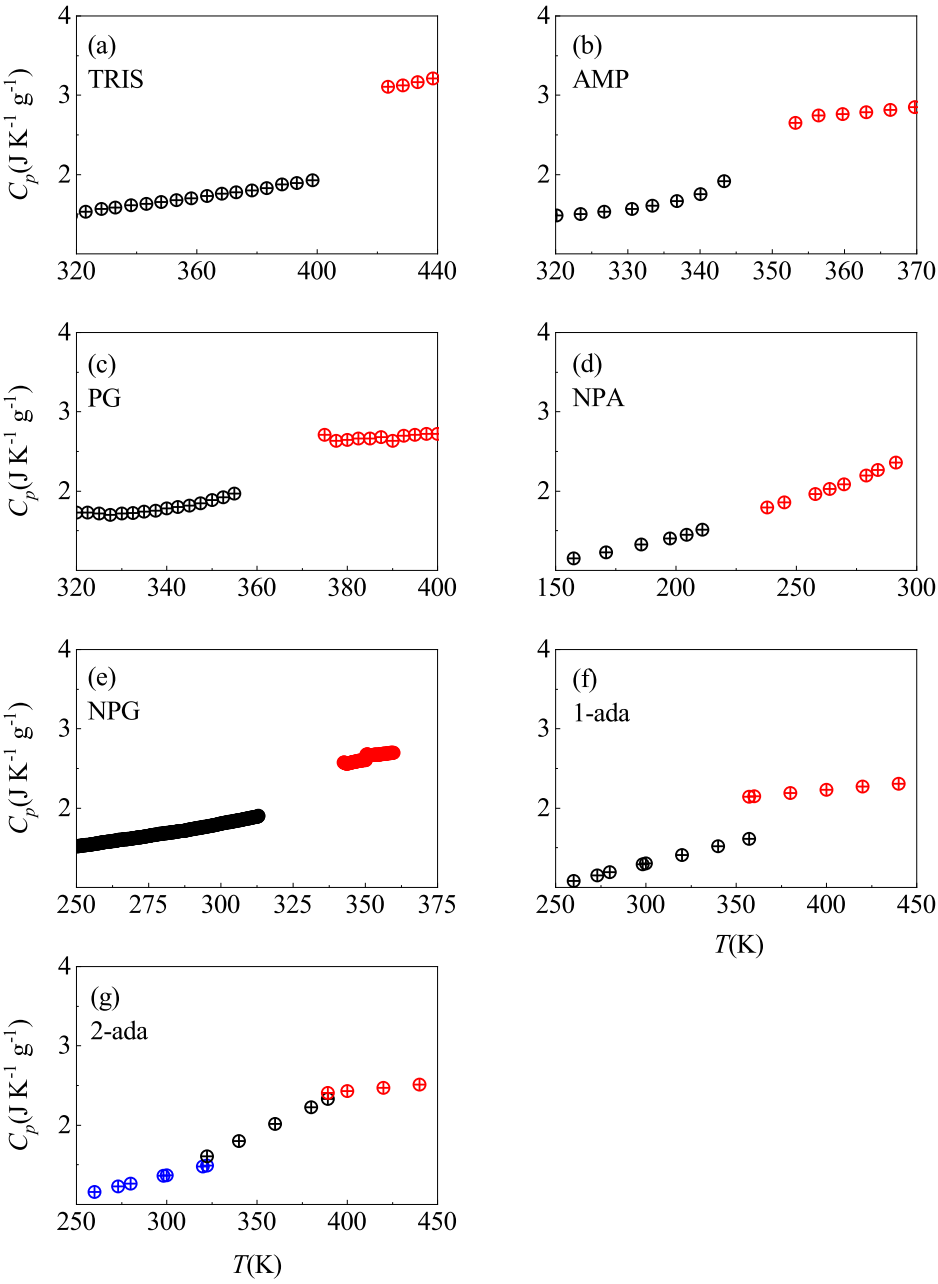

Figure 3.11: Heat capacity measurements from literature of TRIS [80], AMP [115], PG [116], NPA [117], NPG, 1-ada-ol and 2-ada-ol [111]. Red, black and blue dots stand for phases I, II and III respectively.

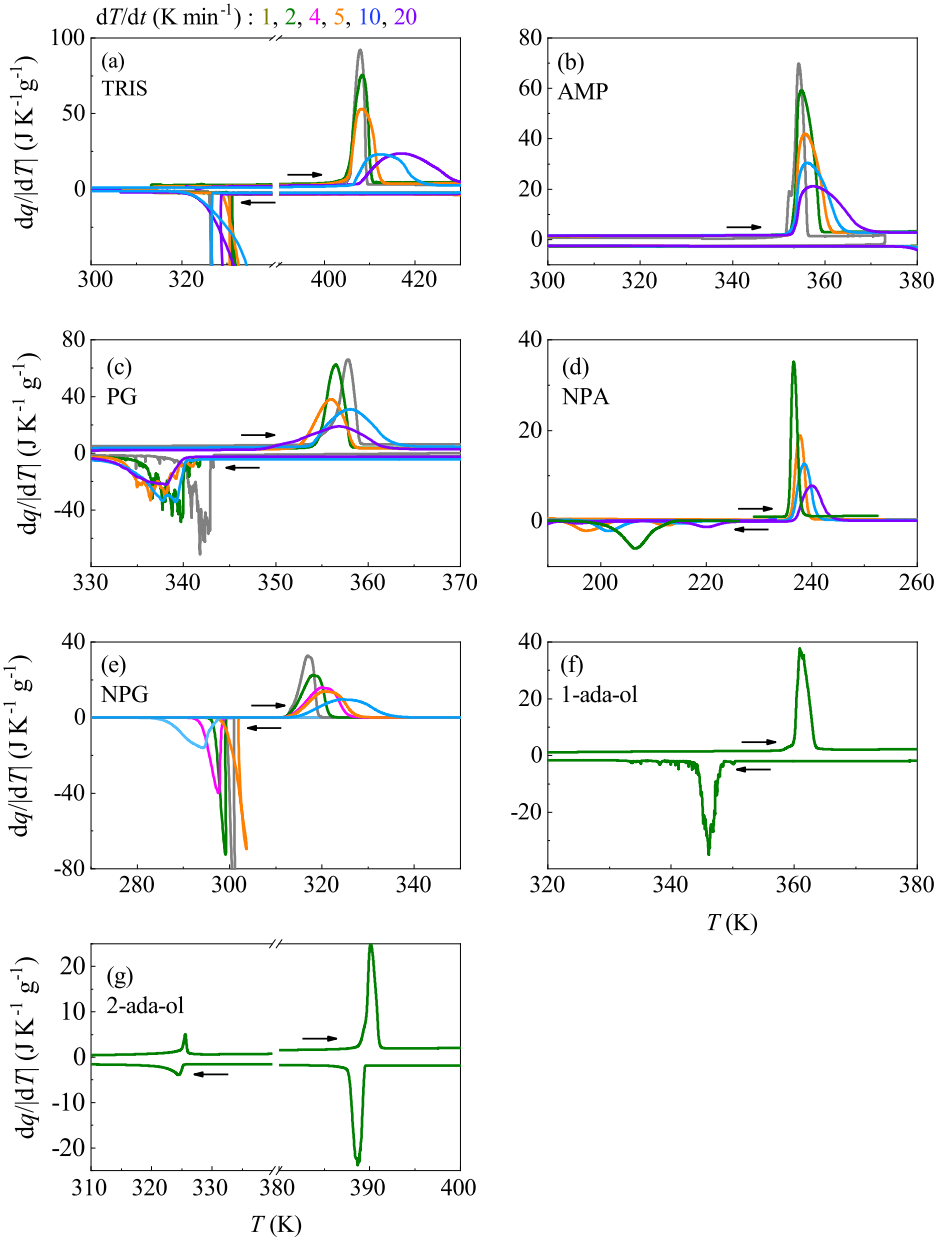

Figure 3.12: DSC measurements at different temperature rates

Compound	Phase	C_p J K^{-1} g^{-1}	$(\partial V/\partial T)_p$ $Å^3$ K^{-1}	$(\partial V/\partial T)_p$ cm^3 g^{-1} K^{-1}
TRIS	I	3.2 ± 0.3 (426 K)	0.09 ± 0.01	$(4.5 \pm 0.5) \times 10^{-4}$
	II	1.9 ± 0.2 (393 K)	0.012 ± 0.001	$(5.9 \pm 0.5) \times 10^{-5}$
AMP	I	2.6 ± 0.3 (352 K)	0.035	2.0×10^{-4}
	II	1.9 ± 0.2 (343 K)	0.016 ± 0.003	$(9.0 \pm 2.0) \times 10^{-5}$
PG	I	2.7 ± 0.3 (382 K)	0.061 ± 0.007	$(3.1 \pm 0.4) \times 10^{-4}$
	II	2.0 ± 0.2 (352 K)	0.012 ± 0.002	$(6.0 \pm 1.0) \times 10^{-5}$
NPA	I	1.9 ± 0.2 (246 K)	0.086 ± 0.003	$(5.8 \pm 0.2) \times 10^{-4}$
	II	1.4 ± 0.2 (204 K)	0.058 ± 0.002	$(3.9 \pm 0.2) \times 10^{-4}$
NPG	I	2.6 ± 0.3 (343 K)	0.067 ± 0.002	$(3.8 \pm 0.4) \times 10^{-4}$
	II	1.9 ± 0.2 (313 K)	0.0031 ± 0.001	$(1.8 \pm 0.6) \times 10^{-5}$
1-ada-ol	I	2.2 ± 0.3 (377 K)	0.083 ± 0.003	$(3.2 \pm 0.2) \times 10^{-4}$
	II	1.5 ± 0.2 (340 K)	0.041 ± 0.001	$(1.6 \pm 0.1) \times 10^{-4}$
2-ada-ol	I	2.4 ± 0.3 (400 K)	0.112 ± 0.001	$(4.4 \pm 0.1) \times 10^{-4}$
	II	1.9 ± 0.2 (350 K)	0.078 ± 0.003	$(3.1 \pm 0.2) \times 10^{-4}$

Table 3.8: Heat capacity and volume variation with respect to temperature for phases II and I. Heat capacity measurements for TRIS, AMP, PG, NPA and 2-ada-ol have been obtained from Refs. [80, 111, 115–117].

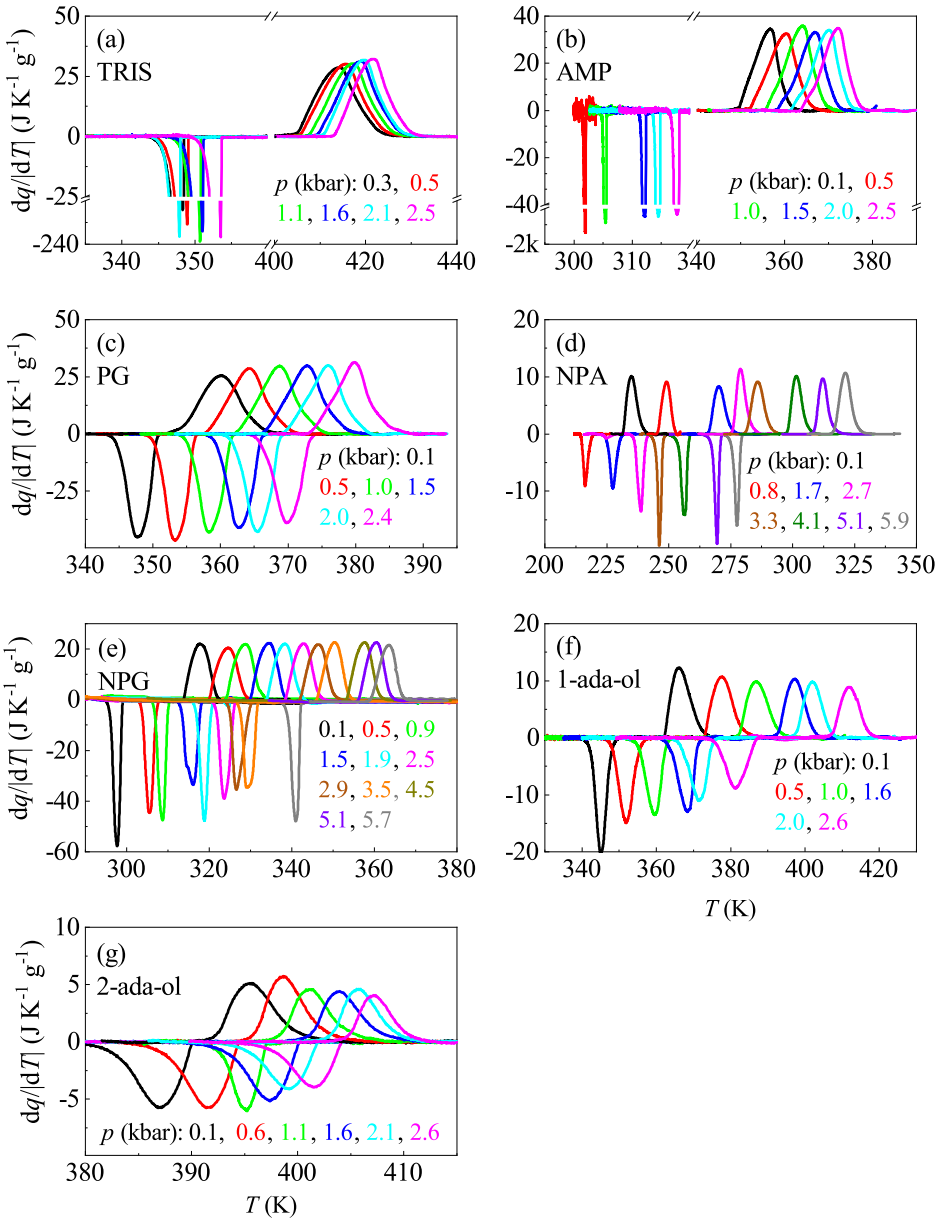

Figure 3.13: DTA measurements under isobaric conditions upon heating and cooling (endothermic and exothermic peaks respectively) after baseline subtraction.

upon applying pressure (Table 3.9).

Contributions to the ΔS_t

Recall that for these compounds the entropy changes at the phase transition have two different contributions: $\Delta S_t = \Delta S_t^e + \Delta S_t^c$, where the first term corresponds to the lattice distortions, and the second term refers to the conformational entropy changes as described in Chapter 1. The elastic constants for plastic crystals are not available in literature. For this reason, we first estimated ΔS_t^e for PG using the elastic constants with respect to temperature for plastic crystal C_{60}. Therefore, considering that $\frac{\partial K}{\partial T} \sim$ -3.8 $\times 10^7$ GPa K^{-1}, $\frac{\partial C'}{\partial T} \sim$ -4.7 $\times 10^6$ GPa K^{-1} and $\frac{\partial C_{44}}{\partial T} \sim$ -2.0 $\times 10^7$ GPa K^{-1} [118], and the symmetry strains $e_1 =$ -0.046, $e_3 = 0.032$ and $e_2 = e_4 = e_5 = e_6 = 0$ [119], the deviatoric contribution yields $\Delta S^d_{II \to I} \simeq 4$ J K^{-1} kg^{-1}, which is negligible with respect to the volumic contribution of $\Delta S^V_{II \to I} \simeq 67$ J K^{-1} kg^{-1}.

For the remaining materials, the deviatoric contribution will be equally not considered. All the studied compounds undergo a reconstructive phase transition, which difficults this last analysis. However, the strain contribution has been computed only for PG since it shows a more direct relationship between structures of phases II and I. Therefore, only the volumic contribution will be of interest.

As introduced in Chapter 1.2, the volume contribution is approximated as $\Delta S_t^V \sim \langle \alpha/\beta \rangle \Delta V_t$, where α and β correspond to the thermal expansion and isothermal compressibility respectively, which are obtained by means of dilatometry and XRD [79, 114]. In Table 3.9 the ΔS_t^V contribution for all materials is presented (except for 1- and 2-ada-ol, since no data has been obtained). It is observed that these results remain well below the total amount of entropy changes at the transition, entailing that the largest part of the entropy emerges from the orientational disordering.

The entropy changes due to conformational disorder can be determined as $\Delta S_t^c = RM^{-1} \ln(N_I/N_{II})$, where the number of configurations at the low-temperature phase can be approximated to $N_{II} = 1$, since the hydrogen bonding do not permits disorder in most of the cases. At the high-temperature phase, com-

pounds presenting a fcc lattice show 10 possible orientations (PG, NPA, NPG), while the bcc lattice allows 6 possible orientations (AMP and TRIS) [120]. Additionally, for each orientation they present 11, 9, 11, 3 and 6 conformations, which yield a total number of configurations of $N_{\mathrm{I}} = 110$, $N_{\mathrm{I}} = 54$, $N_{\mathrm{I}} = 66$, $N_{\mathrm{I}} = 30$ and $N_{\mathrm{I}} = 60$ for PG, AMP, TRIS, NPA and NPG respectively. For NPG, the total amount of transition entropy changes of $\Delta S_{\mathrm{t}} \sim 390$ J K^{-1} kg^{-1} derived from the volume and conformational disorder agrees with the experimental values reported from DSC. Nonetheless, predicted values of $\Delta S_{\mathrm{t}} \sim 325$ J K^{-1} kg^{-1}, $\Delta S_{\mathrm{t}} \sim 287$ J K^{-1}kg^{-1} and $\Delta S_{\mathrm{t}} \sim 315$ J K^{-1} kg^{-1} for PG, TRIS and AMP are approximately 50 % underestimated. In these cases, additional conformations could take place. Therefore, higher values of $\Delta S_{\mathrm{t}}^{c}$ are expected. In turn, NPA shows overestimated transition entropy values of $\Delta S_{\mathrm{t}} \sim 321$ J K^{-1} kg^{-1}, $\sim 60\%$ above the experimental value, and could be explained by an overestimation of the disorder conformations. Evaluation of 1- and 2-ada-ol entropy contributions has not been conducted yet.

Barocaloric effects

According to equation 1.27, as volume measurements present a linear tendency with temperature for all compounds (as seen in Fig. 3.10), the heat capacity is considered non-pressure dependent. Therefore, atmospheric pressure measurements can be employed for the high entropy curves construction. After the application of the quasi-direct and indirect method, the isobaric entropy curves are constructed (Fig. 3.17). From these results, the barocaloric effects are directly computed after the first application and removal of pressure by means of entropy curves subtraction (Fig. 3.18 and 3.19). As expected, outstanding values of non-reversible barocaloric effects are obtained even under considerably low pressure changes. For instance, values of isothermal entropy changes of $|\Delta S| \sim 400$ J K^{-1} kg^{-1} are derived for TRIS, NPA and NPG after pressure changes of 2.0 kbar. In fact, AMP yields the highest values of $|\Delta S| = 650 \pm 70$ J K^{-1} kg^{-1}, and 1- and 2-ada-ol achieve results of $|\Delta S| = 280 \pm 30$ J K^{-1} kg^{-1} and $|\Delta S| = 130 \pm 20$ J K $^{-1}$kg^{-1}, respectively. On the other hand, with the same pressure changes of 2.0 kbar, values of

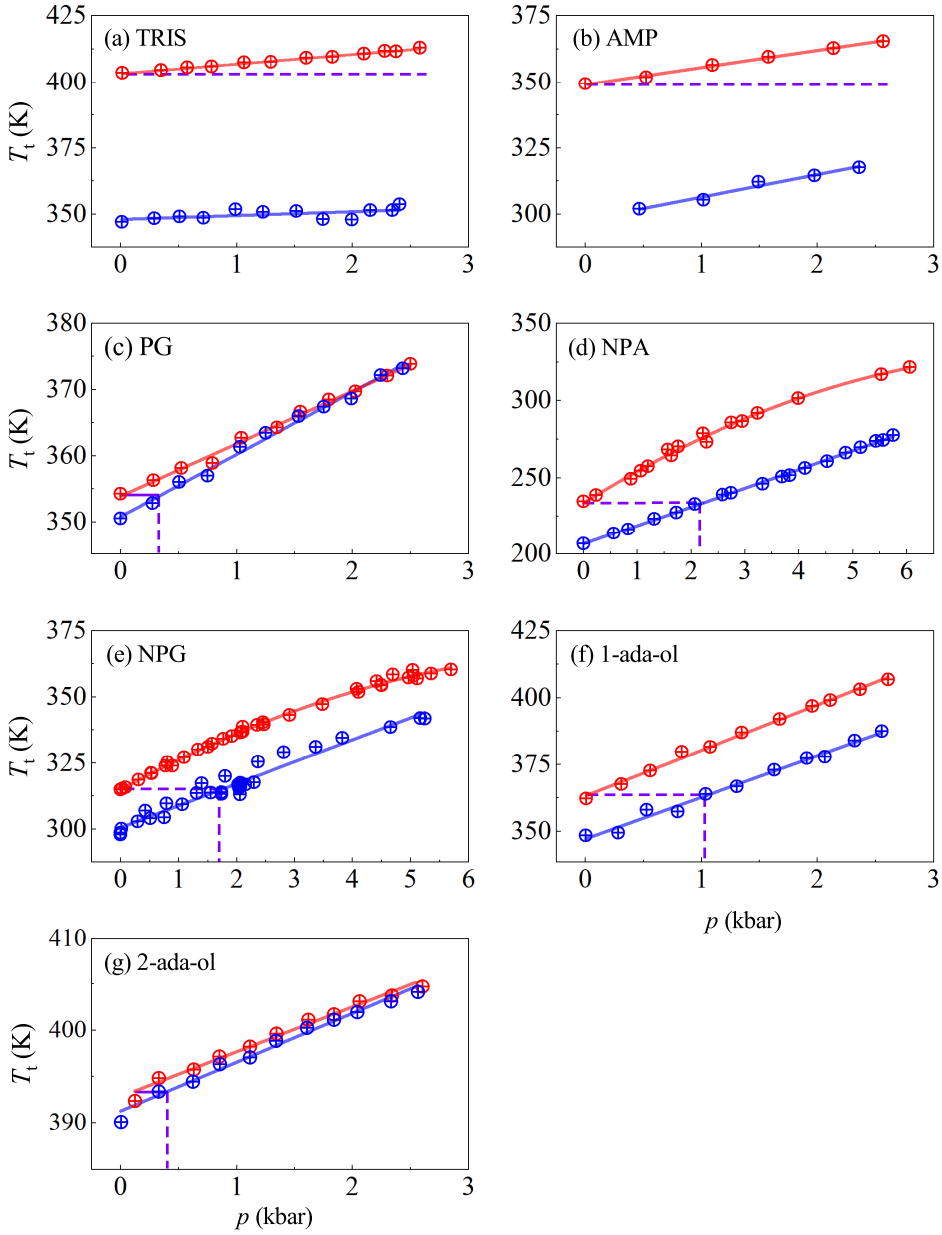

Figure 3.14: T-p diagram, where read and blue circles represent heating and cooling transition temperatures at a certain pressure respectively. Red and blue solid lines stand for linear regressions, and purple dashed lines show the pressure from which reversibility is obtained.

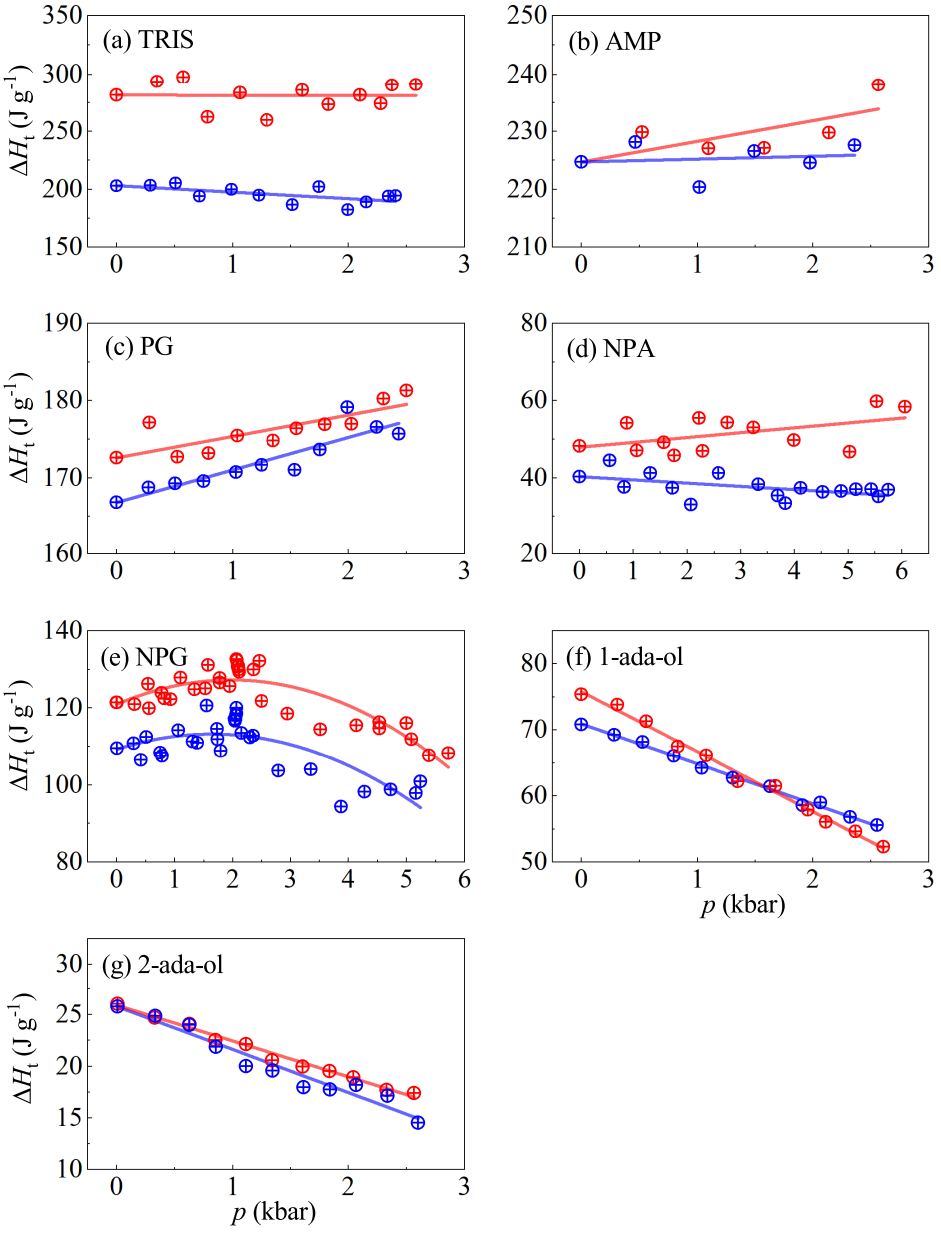

Figure 3.15: Latent heat measurements under isobaric conditions. Red and blue circles correspond to heating and cooling transitions. Lines are fits of the data.

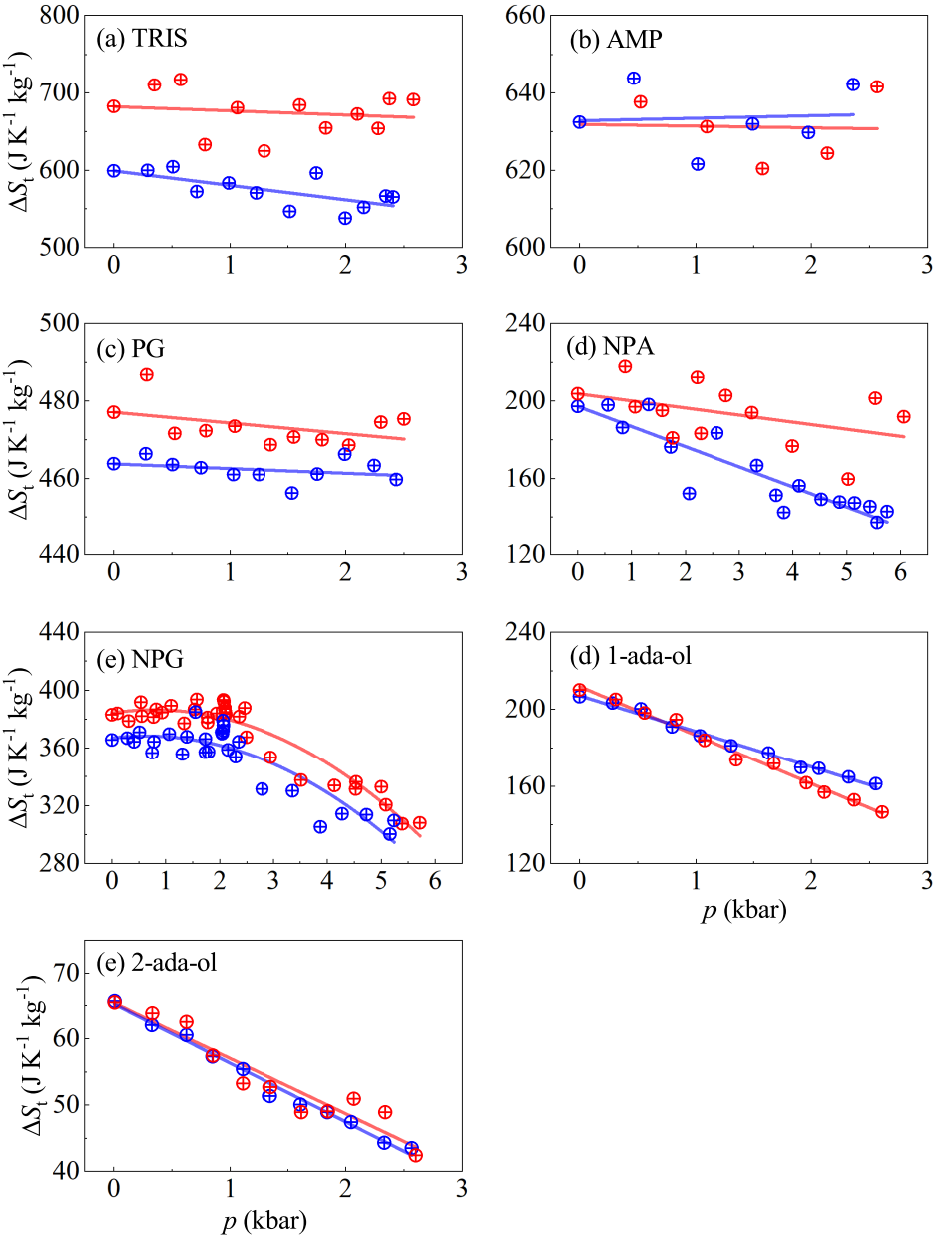

Figure 3.16: Transition entropy changes under isobaric conditions. Red and blue circles correspond to heating and cooling transitions. Lines are fits of the experimental data.

adiabatic temperature changes above $|\Delta T| \sim 10$ K are obtained for TRIS, AMP, PG and 2-ada-ol, respectively. For 1-ada-ol, NPG and NPA the outstanding values of $|\Delta T| = 20 \pm 2$ K, $|\Delta T| = 27 \pm 3$ K and $|\Delta T| = 35 \pm 4$ K are derived. In Table 3.10, the BCEs computed by means of isothermal paths out of the phase transition, following equation 1.25 (method 1), are presented. At phase I, the $\Delta S(p_{\mathrm{atm}} \rightarrow p)$ is also computed by means of isothermal subtraction of isobaric entropy curves (method 2).

Thereafter, the reversible barocaloric effects are computed for PG, NPA, NPG, 1- and 2-ada-ol (Fig. 3.20). More precisely, the reversible values of isothermal entropy changes are determined by means of the overlapping of the non-reversible results from Fig. 3.18. Notice that PG and 2-ada-ol reach reversible values after pressure changes of 0.5 kbar, resulting in $|\Delta S_{\mathrm{rev}}| = 430 \pm 50$ J K^{-1} kg^{-1} and $|\Delta S_{\mathrm{rev}}| = 120 \pm 20$ J K^{-1} kg^{-1}, respectively, and adiabatic temperature changes of $|\Delta T_{\mathrm{rev}}| \sim 6$ K for both compounds. 1-ada-ol presents reversible values after pressure changes of 1.6 kbar, and yields barocaloric effects of $|\Delta S_{\mathrm{rev}}| = 255 \pm 30$ J K^{-1} kg^{-1} and $|\Delta T_{\mathrm{rev}}| = 8 \pm 1$ K at pressure changes of 2.0 kbar. Finally, NPA and NPG show reversibility under pressure changes of 2.5 kbar, and also yield giant reversible isothermal entropy changes of $|\Delta S_{\mathrm{rev}}| = 335 \pm 40$ J K^{-1} kg^{-1} and $|\Delta S_{\mathrm{rev}}| = 320 \pm 40$ J K^{-1} kg^{-1} and adiabatic temperature changes of $|\Delta T_{\mathrm{rev}}| = 12 \pm 2$ K and $|\Delta T_{\mathrm{rev}}| = 7 \pm 1$ K respectively.

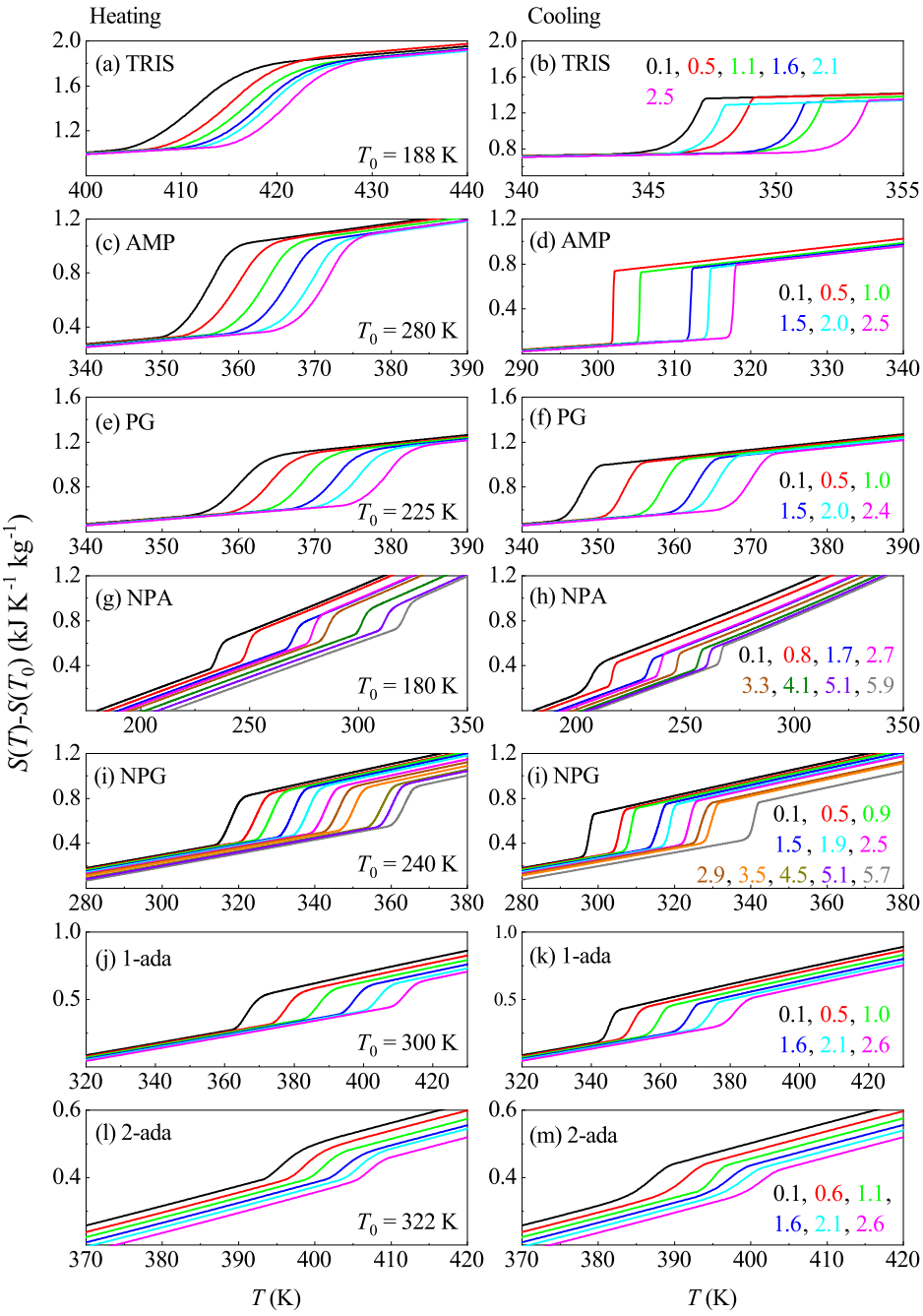

Figure 3.17: Isobaric entropy curves upon heating and cooling (left and right columns respectively) constructed as explained in section 1.3, where T_0 stands for the reference temperature.

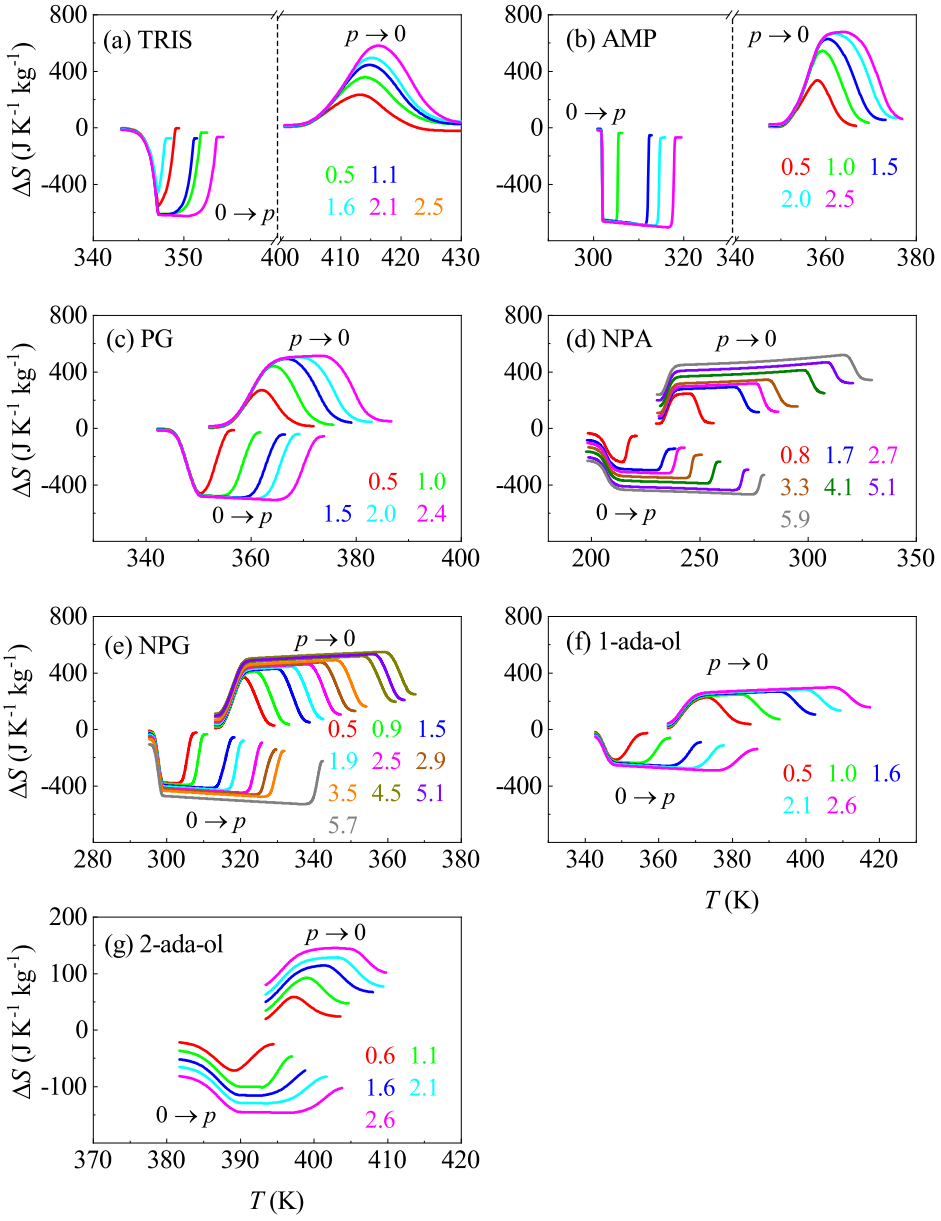

Figure 3.18: Isothermal entropy changes after the first application and removal of pressure.

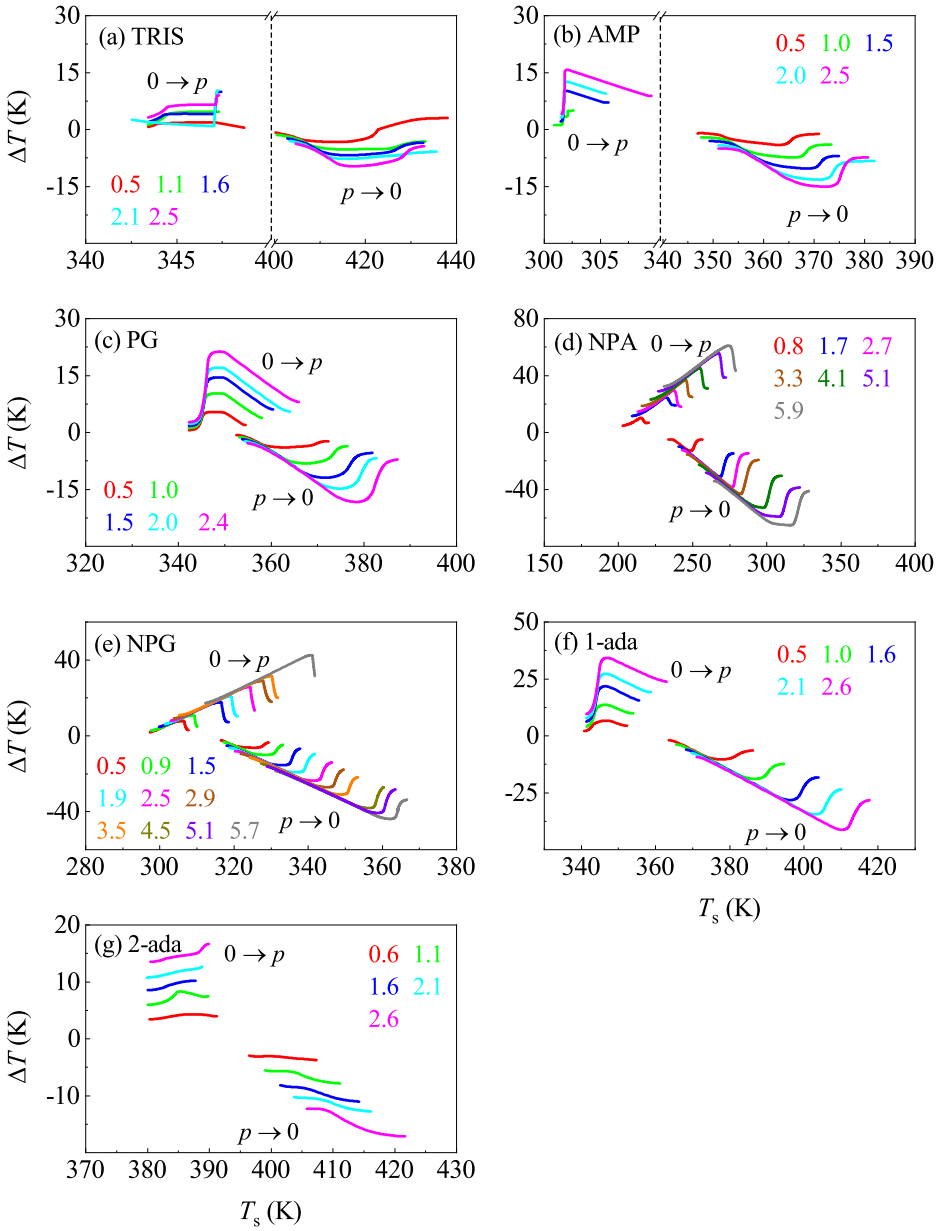

Figure 3.19: Adiabatic temperature changes after the first application and removal of pressure.

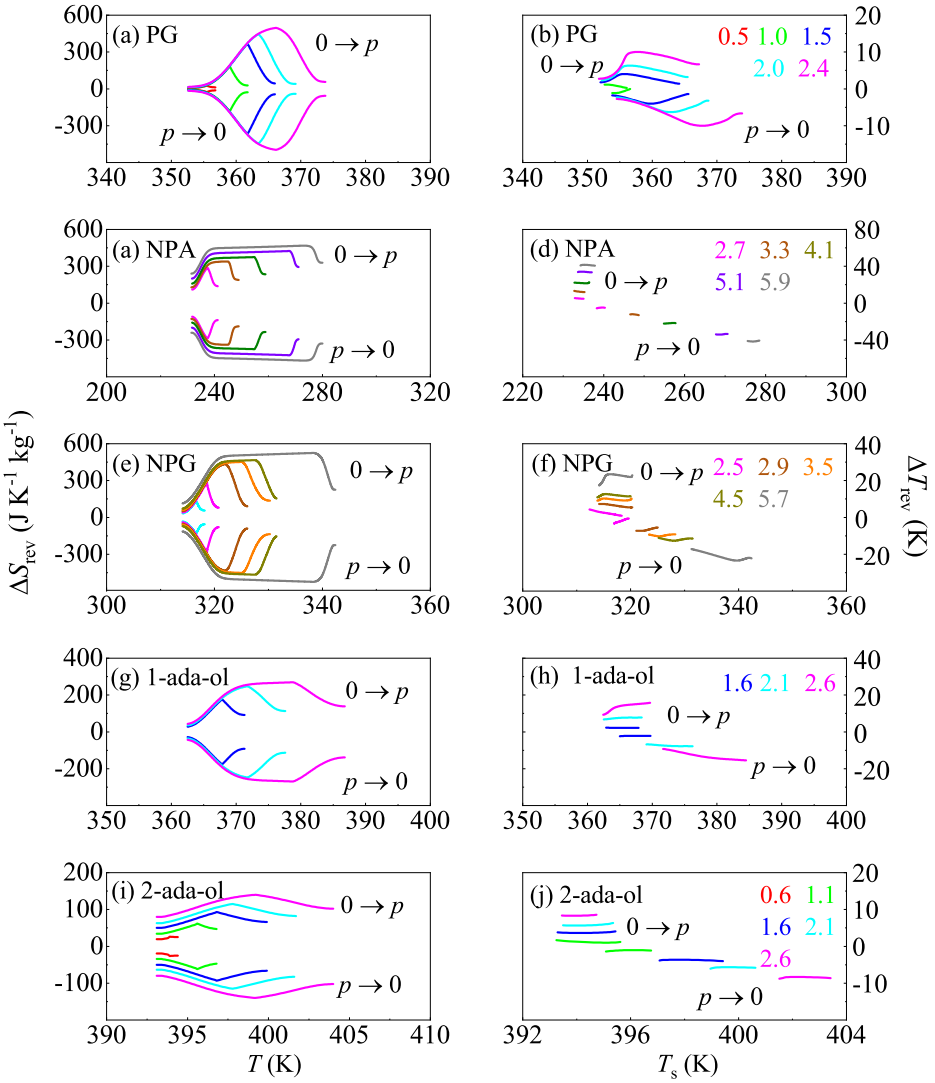

Figure 3.20: Reversible barocaloric effects after cyclic application and removal of pressure. Left and right panels stand for isothermal entropy changes and adiabatic temperature changes respectively.

	$\frac{\lvert\Delta V_t\rvert}{V_I}$ %	Tran.	T_t K	$\frac{dT_t}{dp}$ K kbar^{-1}	$\lvert\Delta H_t\rvert$ J g^{-1}	$\lvert\Delta S_t\rvert$ J K^{-1}kg^{-1}	$\lvert\Delta S_t^V\rvert$ J K^{-1}kg^{-1}	$d\Delta H_t/dp$ J g^{-1}kbar^{-1}	$d\Delta S_t/dp$ J K^{-1} kg^{-1} kbar^{-1}
TRIS	5.2	II → I	407 ± 1	3.7 ± 0.2	280 ± 5	680 ± 20	90 ± 50	-0.2 ± 4.0	-5 ± 10
		I → II	331 ± 1	1.5 ± 0.6	203 ± 5	600 ± 20		-5.6 ± 2.0	-19 ± 6
AMP	10.2	II → I	350 ± 1	6.4 ± 0.4	225 ± 5	630 ± 20	100 ± 50	-3.5 ± 2.0	-0.4 ± 4
		I → II	...	8.5 ± 0.7	...	...		-0.5 ± 2.0	-1 ± 5
PG	6.7	II → I	354 ± 1	7.9 ± 0.2	176 ± 4	490 ± 10	80 ± 40	-2.7 ± 0.7	-3 ± 2
		I → II	351 ± 1	9.4 ± 0.3	164 ± 4	480 ± 10		-4.2 ± 0.6	-1 ± 1
NPA	1.3	II → I	232 ± 1	20.0 ± 0.1	48 ± 2	204 ± 5	52 ± 10	-1.3 ± 0.7	-4 ± 2
		I → II	211 ± 1	11.9 ± 0.2	40 ± 2	197 ± 5		-0.8 ± 0.3	-10 ± 1
NPG	4.9	II → I	314 ± 1	10.4 ± 0.2 [a]	121 ± 2	383 ± 8	60 ± 30	3.0 ± 2.0[a]	3 ± 2[a]
		I → II	300 ± 1	9.3 ± 0.2 [a]	110 ± 2	361 ± 7		2.0 ± 3.0[a]	0.3 ± 5[a]
1-ada-ol	5.0	II → I	361 ± 1	17.9 ± 0.5	76 ± 2	211 ± 4	...	-9.1 ± 0.3	-25 ± 1
		I → II	347 ± 1	15.4 ± 0.5	71 ± 2	207 ± 4		-6.1 ± 0.2	-19 ± 1
2-ada-ol	0.8	II → I	390 ± 1	4.8 ± 0.2	26 ± 1	66 ± 2	...	-4.2 ± 0.3	-8 ± 1
		I → II	389 ± 1	5.3 ± 0.3	26 ± 1	66 ± 2		-3.6 ± 0.2	-9 ± 1

Table 3.9: Thermodynamic data for the II-I phase transition. Results of $\frac{\lvert\Delta V_t\rvert}{V_I}$ represent the relative transition volume changes, T_t the transition temperature, $\frac{dT_t}{dp}$ the transition temperature as a function of pressure, $\lvert\Delta H_t\rvert$ the transition enthalpy change, $\lvert\Delta S_t\rvert$ the transition entropy change, $\lvert\Delta S_t^V\rvert$ the volume contribution to the transition entropy change, $d\Delta H_t/dp$ the transition enthalpy change as a function of pressure and $d\Delta S_t/dp$ stands for the transition entropy change as a function of pressure. Values of enthalpy and entropy are obtained with DSC measurements at 2 K min^{-1}. [a]Measurements at p_{atm}.

Compound	p kbar	$\Delta S_{\mathrm{II}}\,(p_{\mathrm{atm}} \rightarrow p_1)$ J K^{-1} kg^{-1}	$\Delta S_{\mathrm{I}}\,(p_{\mathrm{atm}} \rightarrow p_1)^a$ J K^{-1} kg^{-1}	$\Delta S_{\mathrm{I}}\,(p_{\mathrm{atm}} \rightarrow p_1)^{\mathrm{b}}$ J K^{-1} kg^{-1}
TRIS	1.1	48 ± 6	6 ± 1	20 ± 20
	1.6	72 ± 8	10 ± 1	30 ± 20
	2.1	90 ± 10	12 ± 1	40 ± 20
	2.5	110 ± 20	15 ± 2	30 ± 20
AMP	1.0	9 ± 2	20.3	30 ± 20
	1.5	14 ± 3	29.8	50 ± 20
	2.0	18 ± 4	39.5	60 ± 20
	2.4	22 ± 5	47.2	60 ± 20
PG	1.0	6 ± 1	32 ± 4	20 ± 10
	1.5	9 ± 2	48 ± 6	40 ± 10
	2.0	12 ± 2	63 ± 8	40 ± 10
	2.5	15 ± 3	80 ± 10	50 ± 10
NPA	0.8	32 ± 2	48 ± 2	20 ± 10
	1.7	67 ± 4	100 ± 4	10 ± 10
	3.3	130 ± 7	193 ± 7	140 ± 20
	5.1	200 ± 20	300 ± 20	300 ± 20
NPG	0.9	2 ± 1	34 ± 2	30 ± 20
	1.9	4 ± 1	73 ± 4	70 ± 20
	2.9	5 ± 2	111 ± 6	120 ± 20
	5.1	9 ± 3	200 ± 20	200 ± 20
1-ada-ol	0.5	9 ± 1	18 ± 1	40 ± 10
	1.0	17 ± 1	34 ± 2	70 ± 10
	1.6	27 ± 2	54 ± 4	110 ± 20
	2.6	42 ± 3	84 ± 6	160 ± 20
2-ada-ol	0.6	19 ± 2	28 ± 1	23 ± 4
	1.1	34 ± 3	49 ± 1	48 ± 5
	1.6	50 ± 4	71 ± 2	68 ± 6
	2.6	81 ± 6	115 ± 3	105 ± 8

Table 3.10: Comparison between method 1[a] and method 2[b] for computed high- and low-temperature $\Delta S_{\mathrm{II/I}}$ for heating measurements.

Chapter 4

HYBRID ORGANIC-INORGANIC PEROVSKITES $[\mathbf{TMA}](\mathbf{Mn}(\mathbf{N}_3)_3)$ AND $[\mathbf{TMA}]_2(\mathbf{NaFe}(\mathbf{N}_3)_6)$

4.1 Introduction

The term perovskite originally refers to the calcium titanate $CaTiO_3$, a compound first discovered by Gustav Rose in Ural mounts and named after the mineralogist Lev Perovski [121]. The same term is however now used to refer to other compounds presenting similar crystal structure as $CaTiO_3$ and chemical formula of ABX_3 (Fig. 4.1). In perovskites, positions A and B are occupied by monovalent and divalent metal cations, respectively (where B usually presents smaller radii) whereas the X-site corresponds to a monovalent anion. More precisely, cations at B

are surrounded with six nearest neighbors (X anions) to form an octahedron, while the A cations occupy the center positions in-between these octahedra [122]. Perovskites present diverse chemical composition entailing important physical properties with industrial applications [123]. Nonetheless, the interest in discovering and exploiting new properties led to the synthesis of *Hybrid Organic-Inorganic Perovskites* (HOIPs). In HOIPs, the A-site is occupied by monovalent organic groups such as [TMA] = [-$(CH_3)_4N$], [TrMA] = [-$(CH_3)_3NH$], [MA] = [-$(CH_3)NH_3$], [FA] = [-$CH(NH_2)_2$] and many other (mostly amine cations). Additionally, X positions may correspond to monoatomic, biatomic and multiatomic groups with monovalent charge. At this point, the composition of the X-site anion can give rise to several families of HOIPs, such as halides (X = Cl^-, Br^-, I^-), azides (X = N_3^-), cyanides (X = CN^-), dicynametallites (X = $[Ag(CN)_2]^-, [Au(CN)_2]^-$), hypophosphites (X = $H_2PO_2^-$), borohydrates (X = BH_4^-) and formates[1] (X = $HCOO^-$) [124].

The chemical variability of HOIPs leads to many outstanding properties, such as magnetism [125, 126] and ferroelasticity [125, 127] among many others. These properties find their applications in industry in sensors [128], in gas storage applications [129] and in catalyst electrodes [130]. Additionally, HOIPs have been extensively exploited in photovoltaic cells due to their remarkable optical and electrical features [122, 131–133]. Recently, their efficiencies have considerably improved to values up to 25% which are comparable to those commonly achieved with GaAs around 29% [122, 134]. The barocaloric performance has newly been added as a potential application. High latent heats have been observed in the solid-solid first-order phase transition, which are mainly triggered by order-disorder changes. Among the HOIPs family, azide perovkistes present some of the highest values of transition entropy changes near room temperature (Fig. 4.2). For this reason, in this thesis the barocaloric capabilities of two azide perovskite compounds are further explored.

[1]Formate HOIPs (i.e. organic groups in the X-site), give rise to a particular perovskite family named Metal-Organic perovskite.

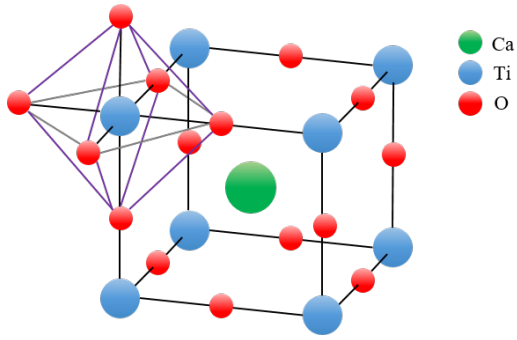

Figure 4.1: $CaTiO_3$ perovskite structure.

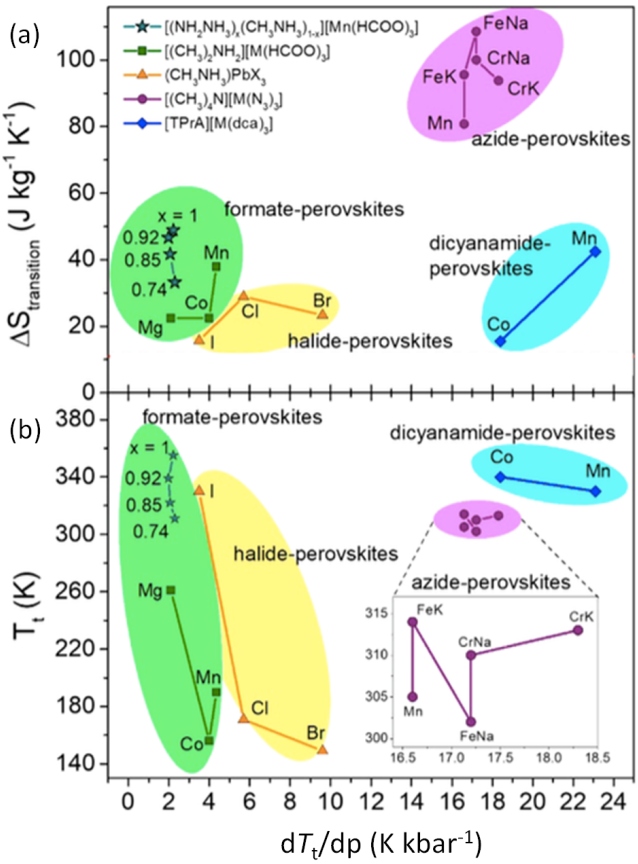

Figure 4.2: Upper and lower panels stand for the transition entropy changes and transition temperature with respect to dT_t/dp respectively. Modified from [135].

4.2 $[TMA](Mn(N_3)_3)$ and $[TMA]_2(NaFe(N_3)_6)$

The BCEs in $[TMA](Mn(N_3)_3)$ and $[TMA]_2(NaFe(N_3)_6)$ azide perovskites have been calculated. These compounds are also referred to as *simple* and *double* perovskites for simplicity. The simple compound has the structure ABX_3, where A = $[TMA]^+$, B = Mn^{+2} and X = N_3^-. Contrary, the double perovskite is arranged as $A_2B'B''X_6$ where the A and X-sites correspond to $[TMA]^+$ and N_3^- respectively (as in the case of the simple perovskite), and the inorganic positions are occupied by B' = Na^+ and B'' = Fe^{+3}.

For both compounds, a solid-solid first-order phase transition near room temperature is observed. In the high temperature phase, both of them present a cubic lattice with configurational disorder in both $[TMA]^+$ cations and azide linkers. The phase transition consists in a cooperative rotation of the $[Mn(N_3)_3]^-$ octahedrons accompanied with center shifts of $[TMA]^+$ cations and N_3^- bridging ligands. They also change their configuration to fixed positions giving rise to order emergence. An exemplification is displayed in Fig. 4.3a for the case of the simple perovskite compound. During the endothermic phase transition an anisotropic volume change is observed. The unit cell parameters a and c expand while b contracts. This negative thermal expansion behavior for the b parameter can be explained as a result of the hydrogen bonding between $[TMA]^+$ cations and N_3^- bridges. As temperature increases this bridging becomes weaker, also reinforcing nitrogen links which result in a shrinkage of the bond distance [136]. The crystallographic data for both compounds are summarized in Table 4.3.

4.3 Results

Powdered samples of $[TMA](Mn(N)_3)_3$ and $[TMA]_2(NaFe(N)_3)_6$ have been synthesized in Huazhong University (China)[2], and used as received. XRD measurements were also performed in Huazhong University (data from Table 4.1), from which the unit cell volume evolution (V/Z) with respect to T was obtained [Fig.

[2]School of Physics, Huazhong University of Science and Technology, Wuhan 430074, Republic of China

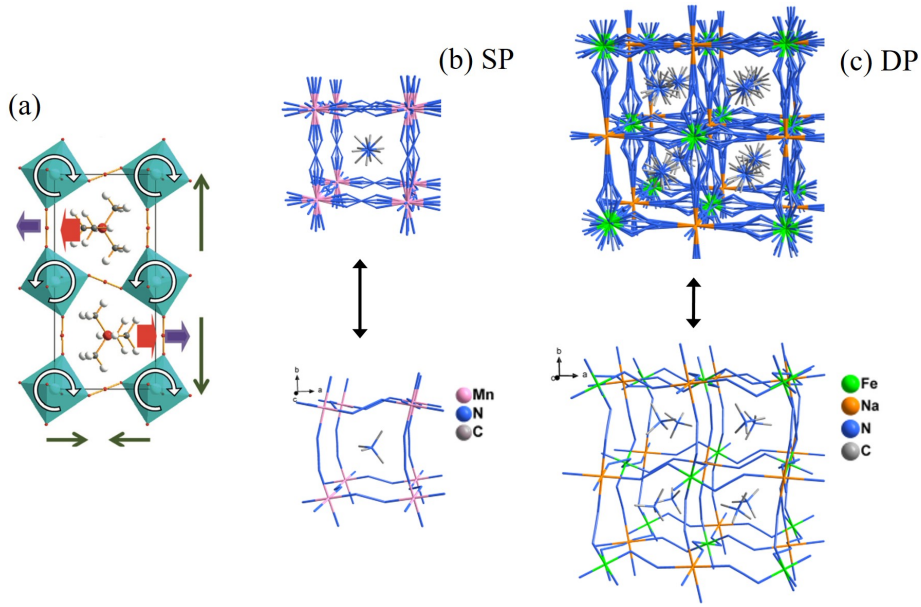

Figure 4.3: (a) Dynamics for the solid-solid phase transition for the simple perovskite. Panels (b) and (c) represent the lattice structures for the simple and double perovskite compounds, where down and up lattices stand for the low- and high-temperature phases, respectively. For the high-temperature phase lattice, multiple positions account for atomic disorder. Modified from [136]

Compound	Phase II		Phase I	
SP	$a = 6.189$ Å $b = 13.173$ Å $c = 6.284$ Å	monoclinic ($P2_1/m$) Z = 2	$a = 6.451$ Å	sc ($Pm\bar{3}m$) Z = 1
DP	$a = 12.796$ Å	fcc ($Fm\bar{3}m$) Z = 4	$a = 13.034$ Å	sc ($Pa\bar{3}$) Z = 4

Table 4.1: Crystallographic data of simple (SP) and double perovskites (DP). Measurements for the simple perovskite were taken at $T = 173$ K and $T = 333$ K for phases II and I, respectively, and at $T = 150$ K and $T = 333$ K for the double perovskite.

4.4(a,b)]. Both compounds present positive transition volume changes through the endothermic phase transition, that according to the Clausius-Clapeyron equation, entail a conventional barocaloric behavior ($\frac{dT}{dp} > 0$). For phases II and I, positive $\left(\frac{\partial V}{\partial T}\right)_p$ values have been determined by means of data linear fits. Standard and modulated DSC measurements have been performed in order to obtain the enthalpy change and heat capacity data at p_{atm}, respectively [Fig. 4.4(c-f)]. Conventional calorimetry has been performed at $|\dot{T}| = 5$ K min^{-1}, and yields remarkable transition entropy changes of ~ 80 J K^{-1} kg^{-1} and ~ 100 J K^{-1} kg^{-1} along with hysteresis values of ~ 3.8 K and ~ 1.3 K for the [TMA](Mn(N)$_3$)$_3$ and [TMA]$_2$(NaFe(N)$_3$)$_6$, respectively. In Table 4.2 data for the heat capacity and $\left(\frac{\partial V}{\partial T}\right)_p$ are summarized for both perovskites in phases II and I.

Compound	Phase	C_p J K^{-1} g^{-1}	$(\partial V/\partial T)_p$ Å^3 K^{-1}	$(\partial V/\partial T)_p$ cm^3 kg^{-1} K^{-1}
SP	I	1.7 ± 0.2 (313.0 K)	0.045 ± 0.004	0.11 ± 0.01
	II	1.7 ± 0.2 (304.2 K)	0.039 ± 0.008	0.09 ± 0.02
DP	I	1.3 ± 0.2 (308.2 K)	0.079 ± 0.003	0.099 ± 0.004
	II	1.6 ± 0.2 (302.8 K)	0.125 ± 0.012	0.16 ± 0.02

Table 4.2: Heat capacity and volume variation with respect temperature of both phases I and II, respectively. Compounds SP and DP correspond to simple and double perovskites, respectively.

Variable-pressure DTA measurements have been performed with the high-pressure calorimeters B and C for the simple and double perovskites, respectively (Fig. 4.5a and 4.5b). As expected, the transition temperature evolves towards higher values upon applying pressure for both of them. From the calorimetric peaks the phase diagram is directly obtained [Fig. 4.5(c,d)], with remarkable values of $\frac{dT_t}{dp}$ above 10 K kbar^{-1}. From peak integration, the transition enthalpy and entropy changes are derived [Fig. 4.5(e-f) and 4.5(g-h)]. As observed, changes at the transition for both compounds decrease under higher applied pressures. It should be pointed out that the pressure dependence for the double perovskite is approximately 3 times that from the simple perovskite compound. In Table 4.3, data derived from the phase transition are summarized.

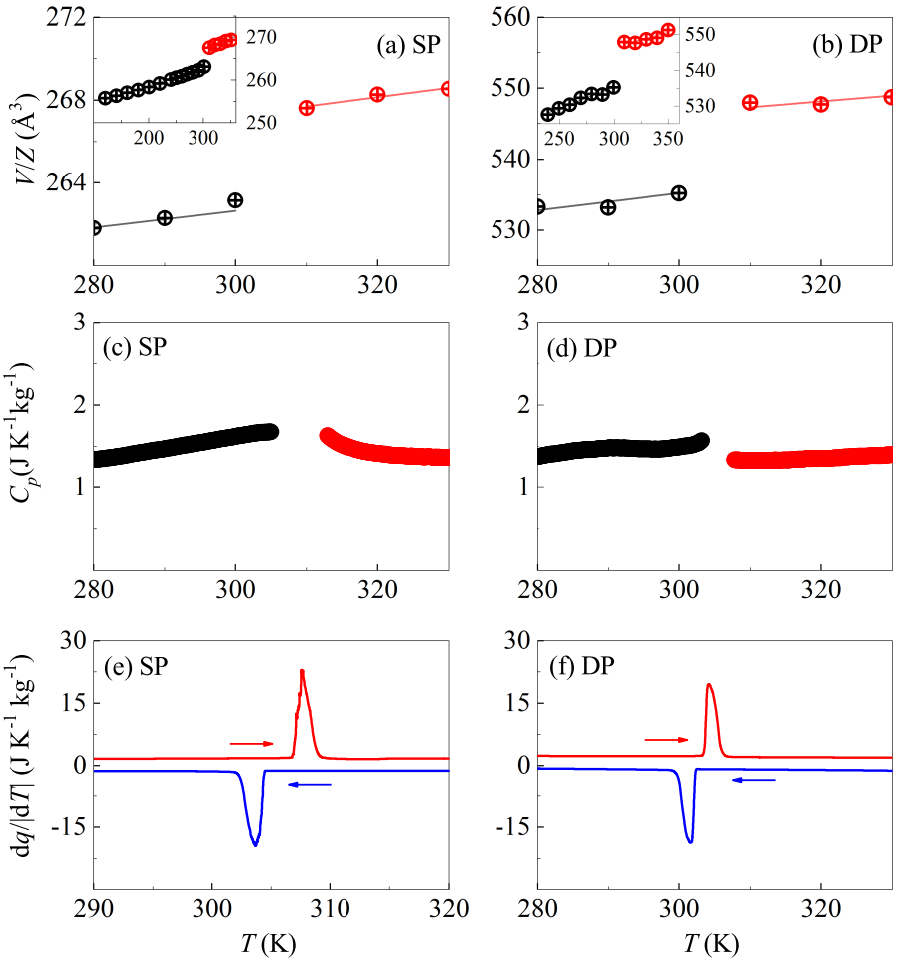

Figure 4.4: Unit cell volume (a,b), heat capacity (c,d) and heat flow measurements (e,f) with respect to temperature are displayed. Left and right columns correspond to simple (SP) and double perovskites (SP), respectively.

	$\frac{\lvert\Delta V_t\rvert}{V_I}$ %	Tran.	T_t K	$\frac{dT_t}{dp}$ K kbar^{-1}	$\lvert\Delta H_t\rvert$ J g^{-1}	$\lvert\Delta S_t\rvert$ J K^{-1} kg^{-1}	$d\Delta H_t/dp$ J g^{-1} kbar^{-1}	$d\Delta S_t/dp$ J K^{-1} kg^{-1} kbar^{-1}
SP	4.5	II → I.	307 ± 1	12.7 ± 0.4	25 ± 1	80 ± 4	-1.0 ± 0.2	-7.5 ± 0.8
		I → II	305 ± 1	12.1 ± 0.2	25 ± 1	81 ± 4	-1.0 ± 0.1	-5.8 ± 0.3
DP	5.4	II → I	304 ± 1	13.5 ± 0.5	30 ± 2	97 ± 4	-5.9 ± 0.4	-21.5 ± 0.9
		I → II	302 ± 1	17.7 ± 0.5	30 ± 2	102 ± 4	-5.5 ± 0.6	-19.5 ± 0.2

Table 4.3: Calorimetry results through the first-order phase transition. DSC measurements have been performed at 5 K min^{-1}. SP and DP stand for simple and double perovskites.

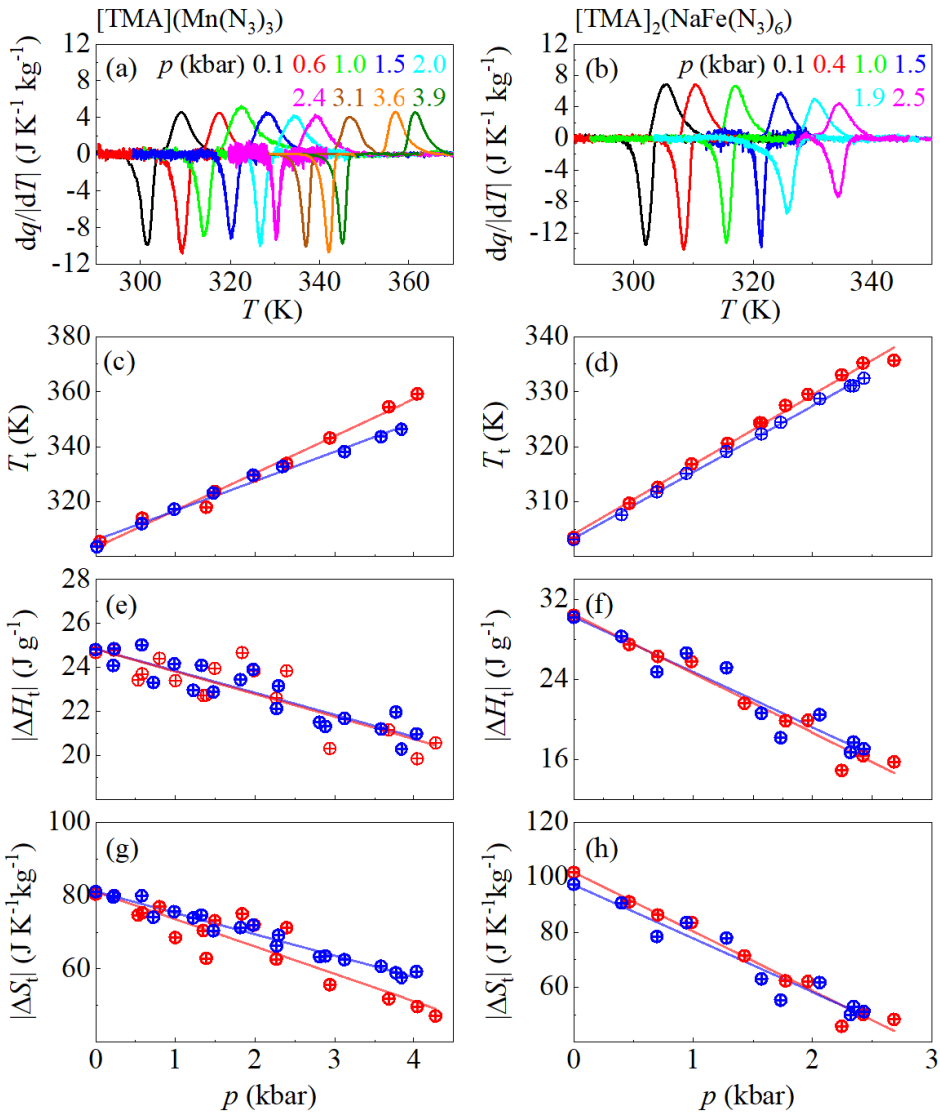

Figure 4.5: DTA measurements under pressure with respect to temperature at the quoted pressures (a,b) and start transition temperature (c,d), latent heat (e,f) and transition entropy change (g,h) with respect to pressure are displayed. Left and right columns show simple (SP) and double perovskite (DP) measurements, respectively. Blue and red dots correspond to heating and cooling runs.

For these compounds the transition entropy change emerges from the configurational and volumetric contributions: $\Delta S_\mathrm{t} = \Delta S_\mathrm{t}^c + \Delta S_\mathrm{t}^V$. More precisely, ΔS_t mainly comes from the order-disorder change through the phase transformation. In the case of the simple perovskite, the ratio of the high- and low-temperature

configurations is $N_{\mathrm{I}}/N_{\mathrm{II}} \sim 12$ [136]. Therefore, the configurational part of the transition entropy change is determined as $\Delta S_{\mathrm{t}}^{c} = \frac{R}{M} \ln(N_{\mathrm{I}}/N_{\mathrm{II}}) \sim 81$ J K^{-1} kg^{-1}, which highly agrees with the experimental result of $\Delta S_{\mathrm{t}} = 80 \pm 1$ J K^{-1} kg^{-1} determined by means of DSC. Within the same line of reasoning, for the double compound the order-disorder ratio $N_{\mathrm{I}}/N_{\mathrm{II}} \sim 525$ has been determined form DSC measurements [137] assuming that the configurational entropy change accounts for the full transition entropy change. The resulting configurational contribution of $\Delta S_{\mathrm{t}} = 111.5$ J K^{-1} kg^{-1}, lays slightly above with respect to our experimental DSC value of $\Delta S_{\mathrm{t}} = 97 \pm 1$ J K^{-1} kg^{-1} [137]. The volume contribution can not be evaluated since no data of the isothermal compressibility β is available. Nonetheless, the configurational contribution itself already suggests its main contribution in the first-order phase transition.

Quasi-direct and indirect methods have been applied in order to compute the isobaric entropy curves upon heating and cooling runs [Fig. 4.6(a,b) and Fig. 4.7(a,b) for the simple and double perovskites, respectively]. Note that since $V(T)/Z$ is a linear function of T, according to equation 1.27 it can be also assumed that $\frac{\partial C_p}{\partial p} \sim 0$. Therefore, the atmospheric pressure measurement of C_p can also be used to construct the isobaric entropy curves at higher pressures, where the entropy value at the reference temperature T_0 is adjusted following an isothermal path as defined in equation 1.25. At this point, the BCEs in the high-temperature phase can be determined from the isobaric entropy curves subtract, or also using the last mentioned equation 1.25 (method 1 and 2, respectively). In Table 4.4, method 1 and 2 are put into comparison, where a strong discrepancy is observed for high-pressure changes, especially for compound [TMA]$_2$(NaFe(N)$_3$)$_6$. This error may be associated with the calorimeter calibration, which in turn induces error in the experimental measurement of C_p, and the error associated with the volume measurement from which $\left(\frac{\partial V}{\partial T}\right)_p$ is derived. Nonetheless, this error does not affect much the BC results.

By means of curves subtraction, the $\Delta S(T, p_{\mathrm{atm}} \rightleftarrows p)$ and $\Delta T(S, p_{\mathrm{atm}} \rightleftarrows p)$ upon the first application and removal of pressure have been determined. Outstanding values of $|\Delta S| = 110 \pm 20$ J K^{-1} kg^{-1} and $|\Delta S| = 150 \pm 20$ J K^{-1} kg^{-1} are

obtained for the simple and double perovskite, respectively, after pressure changes of 2.5 kbar. Additionally, $|\Delta T| = 20 \pm 2$ K and $|\Delta T| = 30 \pm 3$ K are also achieved under the same applied pressure. It is also worth noting that under the minimum pressure changes of 0.5 kbar, remarkable barocaloric effects are already determined, reaching values of $|\Delta S| = 80 \pm 8$ J K^{-1} kg^{-1} and $|\Delta T| = 5 \pm 1$ K for both compounds [Fig. 4.6(c,d) and 4.7(c,d)]. As observed in the phase diagram, both materials are fully reversible since small values of hysteresis have been determined. At this point, the barocaloric effects under cyclic pressure changes have been computed. Due to the aforementioned small hysteresis values, the reversible and non-reversible results of the barocaloric effects are approximately the same for both of them. Values of $|\Delta S_{\mathrm{rev}}| = 100 \pm 10$ J K^{-1} kg^{-1} and $|\Delta S_{\mathrm{rev}}| = 130 \pm 20$ J K^{-1} kg^{-1} have been obtained, and adiabatic temperature changes of $|\Delta T_{\mathrm{rev}}| = 15 \pm 2$ K and $|\Delta S_{\mathrm{rec}}| = 25 \pm 3$ K for the simple and double perovskite, respectively, upon pressure changes of 2.5 kbar [Fig. 4.6(e,f) and 4.7(e,f)].

Compound	p kbar	$\Delta S_{\mathrm{II}}\,(p_{\mathrm{atm}} \rightarrow p_1)$ J K^{-1} kg^{-1}	$\Delta S_{\mathrm{I}}\,(p_{\mathrm{atm}} \rightarrow p_1)^a$ J K^{-1} kg^{-1}	$\Delta S_{\mathrm{I}}\,(p_{\mathrm{atm}} \rightarrow p_1)^{\mathrm{b}}$ J K^{-1} kg^{-1}
SP	1.0	9 ± 2	11 ± 1	15 ± 8
	1.9	18 ± 4	21 ± 2	19 ± 9
	2.9	27 ± 6	31 ± 3	20 ± 10
	4.0	37 ± 8	43 ± 4	30 ± 10
DP	0.9	15 ± 2	9.4 ± 0.4	20 ± 10
	1.6	25 ± 3	15.5 ± 0.6	50 ± 10
	2.0	32 ± 4	20.5 ± 0.8	50 ± 10
	2.5	39 ± 5	24 ± 1	70 ± 10

Table 4.4: Comparison between method 1[a] and method 2[b] for computing high- and low-temperature $\Delta S_{\mathrm{II/I}}$ for heating measurements. SP and DP refer to the simple and double perovskites respectively.

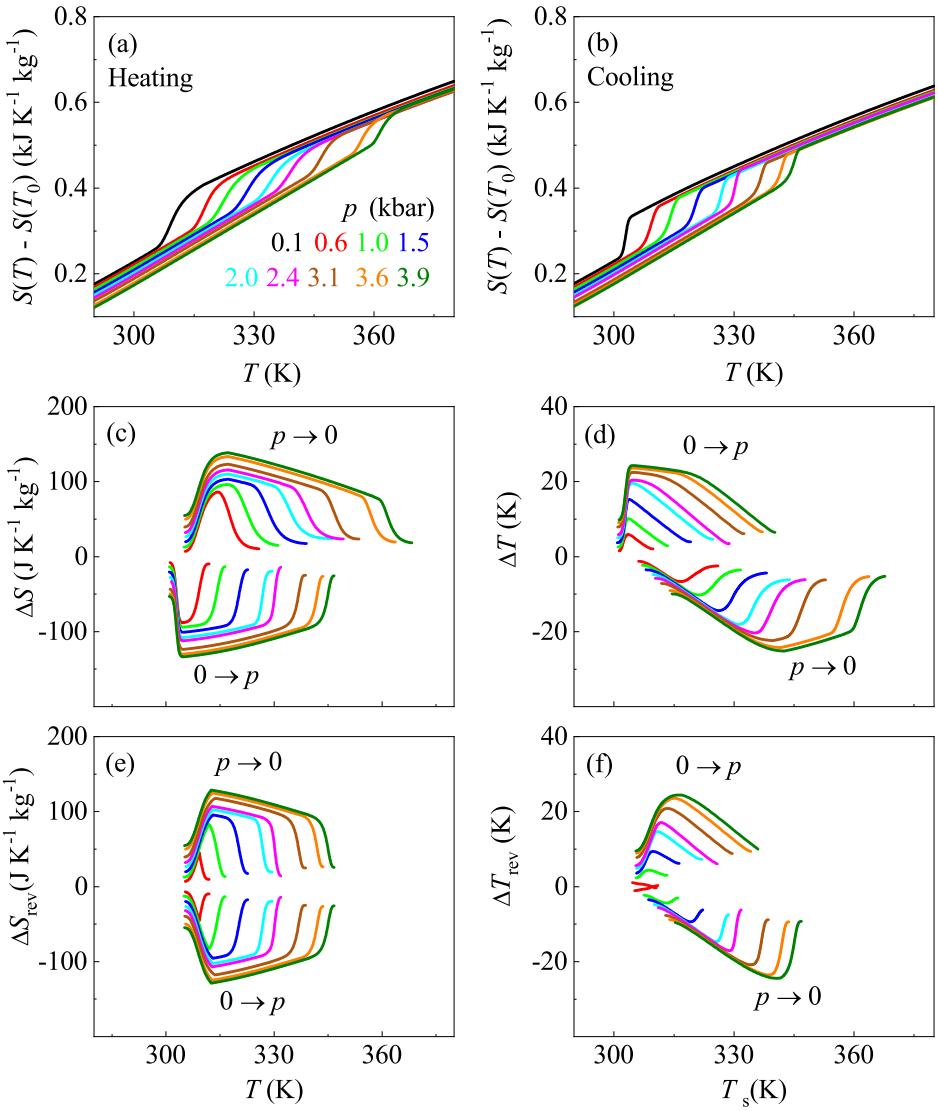

Figure 4.6: Panels (a) and (b) display the isobaric entropy curves for the simple perovskite [TMA](Mn(N)$_3$)$_3$ upon heating and cooling respectively, which derive the irreversible (c) and reversible isothermal entropy changes (d), and irreversible (e) and reversible adiabatic temperature changes (f) upon applying and removing pressure.

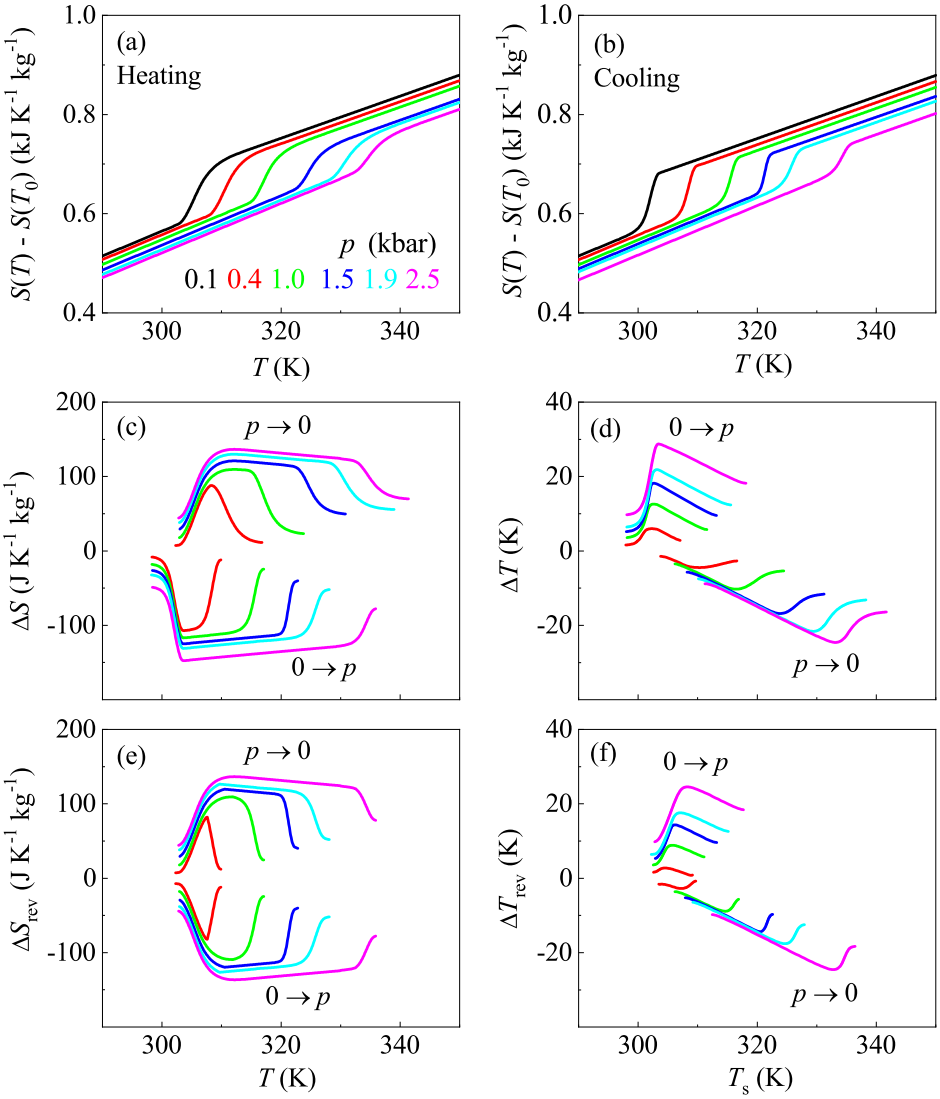

Figure 4.7: Panels (a) and (b) display the isobaric entropy curves for the double perovskite $[TMA]_2(NaFe(N)_3)_6$ upon heating and cooling respectively, which derive the irreversible (c) and reversible isothermal entropy changes (d), and irreversible (e) and reversible adiabatic temperature changes (f) upon applying and removing pressure.

Chapter 5

MAGNETIC ALLOYS

5.1 Introduction

Magnetic alloys are composed by different metallic elements in which at least one of them presents non-null magnetic moment. By means of tuning its composition and concentration, some of its physical properties can be modified resulting in advantageous applications. For instance, magnetic alloys are found in many areas of electronics, telecommunications, power converters (transformers and inductors), etc.

One of these remarkable properties is the magnetocaloric effect (MC), which in fact was first observed in iron by Warburg [138]. The MC effect arises when the application and removal of magnetic field through a magnetic alloy induces changes in entropy and temperature. Analogously to the BC effects, MC effects are enhanced at the vicinity of a magnetic transition, since higher magnetization changes also derive larger MC effects[1]. Nonetheless, pure ferromagnetic transitions are second-order, and the gradual magnetization change does not allow for remarkable MC performances [139]. For this reason, enhanced MC effects are observed in

[1] The isothermal entropy changes derived after the application of magnetic field (H) are

$$\Delta S(T, H_0 \rightarrow H_1) = \int_{H_0}^{H_1} \left(\frac{\partial M(T,H)}{\partial T} \right)_H dH,$$

where M is the magnetization, and H_0 and H_1 stand for the initial and final magnetic fields.

first-order magnetic transitions, which also entail coupling between magnetic and lattice degrees of freedom.

This coupling between magnetism and structure can be understood from a microscopic point of view. When a magnetic field is applied, the crystallographic structure associated with the higher magnetization is favored, therefore, a phase transition is induced from the low magnetization towards the higher magnetization phase. For this to happen, a change in magnetization between both phases is imperative, which according to the Clausius-Clapeyron equation is associated with the transition entropy change as $\frac{\mu_0 dT}{dH} = -\frac{\Delta M_t}{\Delta S_t}$ [140].

Many magnetic materials undergo athermal solid-solid phase transitions by which the transformation is not triggered by thermal fluctuations, and the system evolves in a diffusionless cooperative way [141]. In this kind of transitions the whole transformation is not triggered only at T_t (not isothermal transition), but instead, the whole temperature transition range needs to be overcome. Because of this, invariant hysteresis and calorimetry peak width with respect to temperature rate are expected.

In this thesis four magnetic alloys are studied. All of them are alloys based in Mn, which is the main element providing magnetic moment. The BC effects of these magnetic alloys are studied, which are expected to compete with other reported giant MC and eC effects [139, 142].

5.2 $MnCoGeB_{0.03}$

$MnCoGeB_{0.03}$ is a magnetic alloy based on MnCoGe and subsequently doped with boron. According to Trung *et.al.* [143], the boron doping allows to tune hysteresis and T_C (i.e. the Curie temperature) among other parameters. In this thesis, x = 0.03 is selected since at this boron concentration smaller hysteresis and T_C values result. In particular, T_C is tuned to coincide with the structural transformation. Consequently, at[2] $T_t^{II \to I} = 292$ K it undergoes a magnetostructural

[2]Martensitic transitions, due to their non isothermal condition, are characterized by start and finish transition temperatures. When inducing the transformation upon heating, start and finish austenite transition temperatures are referred as A_s and A_f, respectively. Likewise, upon cooling, start and finish martensite transition temperatures are accordingly named M_s and M_f.

martensitic phase transition from a ferromagnetic (FM) low-temperature phase where atoms are arranged in an orthorhombic lattice (TiNiSi-type, space group Pnma), to a high-temperature paramagnetic (PM) phase with hexagonal structure (Ni_2In -type, space group $P6_3/mmc$) [144] accompanied with negative transition volume changes. Fig. 5.1 shows the crystal structure of phases II and I, whose lattice parameters are summarized in Table 5.1.

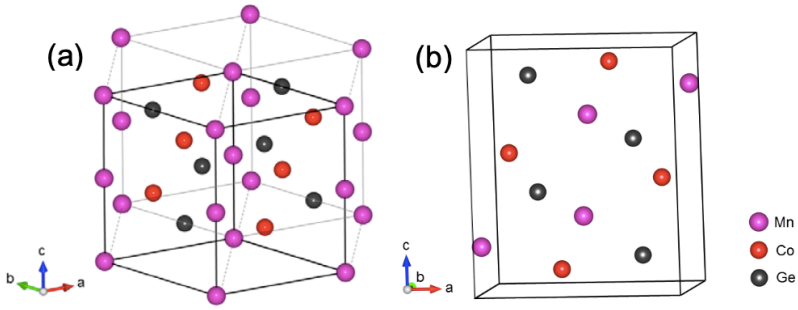

Figure 5.1: Hexagonal (a) and orthorhombic (b) phases for a MnCoGe-based alloy. Extracted from Ref. [145].

MnCoGe is a well known MC material [146–148]. Nonetheless, apart from the low sensitivity of the T_t to the magnetic field, $\frac{dT_t}{\mu_0 dH} \sim 2$ K T^{-1}, the high volume change observed at the magnetostructural phase transition ($|\Delta V_t|/V_I \sim 4\%$) cause the sample fragmentation, and consequently problems arise when designing MC cooling devices [149].

Phase II (300 K)	Phase I (350 K)
orthorhombic (Pnma) FM a =5.9321(7) Å b = 3.8199(6) Å c = 7.0561(7) Å Z = 1	hexagonal ($P6_3/mmc$) PM a = 4.0848(8) Å c = 5.3044(7) Å Z = 1

Table 5.1: Crystallographic parameters of $MnCoGeB_{0.03}$ [150].

Results

The sample was synthesized at the IPICYT[3] and used as received. X-ray diffraction measurements have been performed by the Chemistry Department and the Maxwell Center also from University of Cambridge (consult Appendix B) in order to compute the unit cell volume variation as a function of temperature (Fig. 5.2a). Negative transition volume changes are observed upon heating. Therefore, according to the Clausius-Clapeyron equation, inverse BCEs are expected. Additionally, negligible values of $\left(\frac{\partial V}{\partial T}\right)_p$ are derived out of the phase transition, which may anticipate small variations of $\Delta H_{\rm t}$ and $\Delta S_{\rm t}$ under applied pressures.

Standard and modulated DSC scans have been carried out at $p_{\rm atm}$ (Fig. 5.2b and 5.2c) in order to obtain calorimetry and heat capacity measurements (performed at University of Cambridge[4]), respectively. Standard DSC has been performed with temperature rate of $|\dot{T}| = 2$ K min^{-1}, and yield values of transition entropy changes of ~ 45 J K^{-1} kg^{-1} associated with hysteresis values of ~ 10 K. In Table 5.5 measurements of C_p and $(\partial V/\partial T)_p$ are summarized for phases I and II, where the small value of $(\partial V/\partial T)_p$ define this alloy as a nearly invar material.

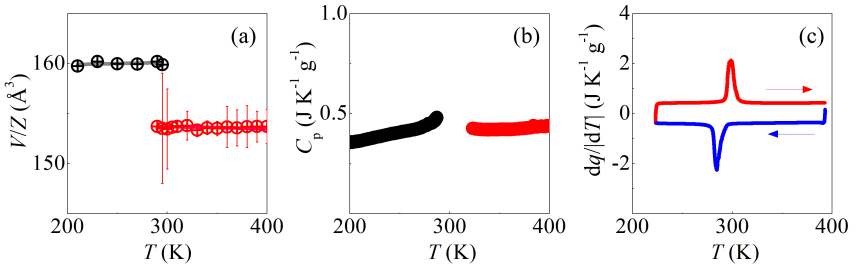

Figure 5.2: Unit cell volume (a), the heat capacity (b) and heat flow measurements (c) as a function of temperature for $MnCoGeB_{0.03}$. Red and blue lines stand for heating and cooling runs, and red and black circles for phase I and II measurements, respectively.

Variable-pressure DTA measurements have been carried out up to pressure values of 6 kbar by means of calorimeter C (Fig. 5.3a). As predicted by $V(T)/Z$ measurements, the $T_{\rm t}$ evolves towards lower temperature values upon applying pressure (Fig. 5.3b). More precisely, from the phase diagram, remarkable values

[3]Instituto Potosino de Investigación Científica y Tecnológica, Mexico
[4]Department of Materials Science, University of Cambridge, Cambridge CB3 0FS, UK

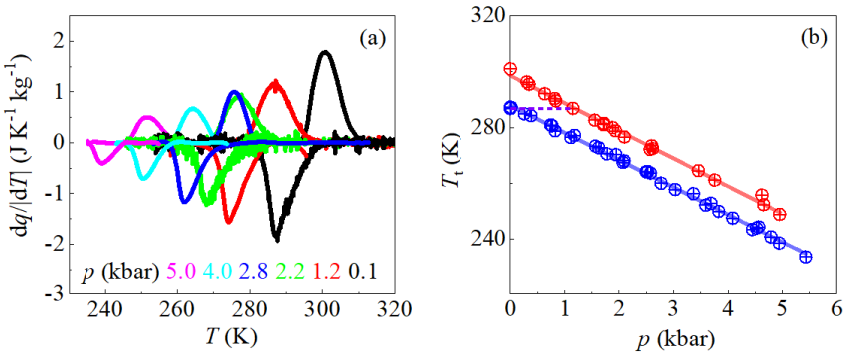

Figure 5.3: High-pressure calorimetric curves (a) and phase diagram (b) for $MnCoGeB_{0.03}$ where red and blue circles stand for heating and cooling runs respectively. Lines are fits of the data.

of $dT_t/dp \sim 10$ K kbar^{-1} are achieved. By means of peak integration, the pressure dependence of latent heat and transition entropy changes are computed [Fig. 5.4(a,b)]. Also, in Table 5.6 additional data regarding the phase transformation is summarized.

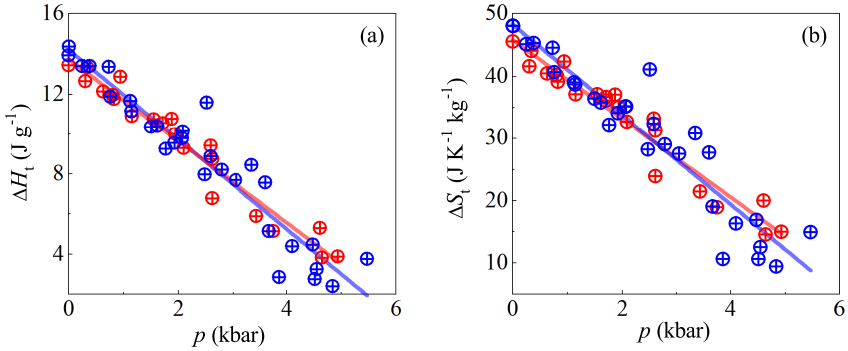

Figure 5.4: Transition enthalpy changes (a) and transition entropy changes (b) as a function of pressure for $MnCoGeB_{0.03}$. Red and blue circles stand accordingly for heating and cooling measurements. Lines are fits of the data.

The quasi-direct and indirect methods have been applied in order to construct the isobaric entropy curves (Fig. 5.5). As $\left(\frac{\partial V}{\partial T}\right)_p \approx 0$, according to equation 1.27 the pressure dependence of the heat capacity is $\left(\frac{\partial C_p}{\partial p}\right)_T \approx 0$. Consequently, the atmospheric pressure measurements of C_p can be employed to compute the high-pressure isobaric entropy curves. Recall that the entropy value at the reference temperature T_0 is adjusted following an isothermal path as defined in equation

1.24.

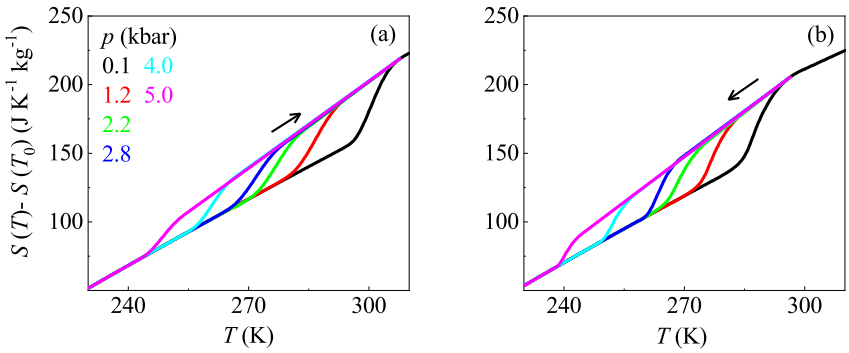

Figure 5.5: Isobaric entropy curves upon heating (a) and cooling (b) where $T_0 = 200$ K for $MnCoGeB_{0.03}$.

By means of isobaric entropy curves subtraction, $\Delta S\,(T, p_{\text{atm}} \rightleftarrows p)$ and $\Delta T\,(S, p_{\text{atm}} \rightleftarrows p)$ upon the first application and removal of pressure have been computed (Fig. 5.6). For instance, remarkable results of $|\Delta S| = 35 \pm 4$ J K^{-1} kg^{-1} and $|\Delta T| = 7 \pm 1$ K have been obtained upon pressure changes of 1.0 kbar. Additionally, as observed in the phase diagram, $MnCoGeB_{0.03}$ will present reversibility. Therefore, the BC effects driven upon the cyclic application and removal of pressure are computed (Fig. 5.7), which render large values of $|\Delta S_{\text{rev}}| = 25 \pm 3$ J K^{-1} kg^{-1} and $|\Delta T_{\text{rev}}| = 6.5 \pm 1$ K upon pressure changes of 2 kbar.

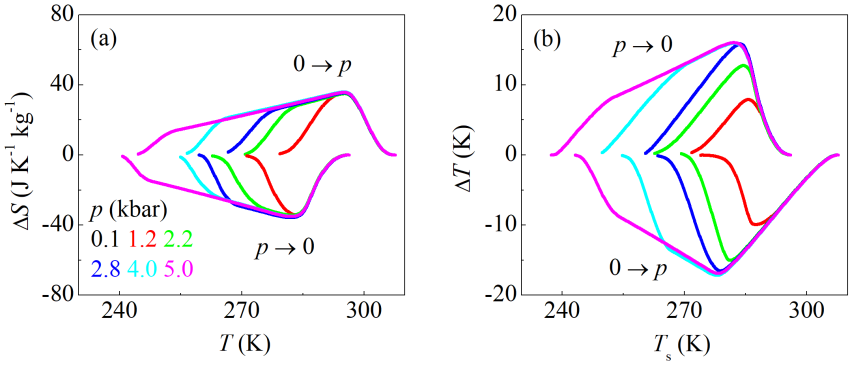

Figure 5.6: Irreversible isothermal entropy changes (a) and adiabatic temperature changes (b) under different pressure changes for $MnCoGeB_{0.03}$.

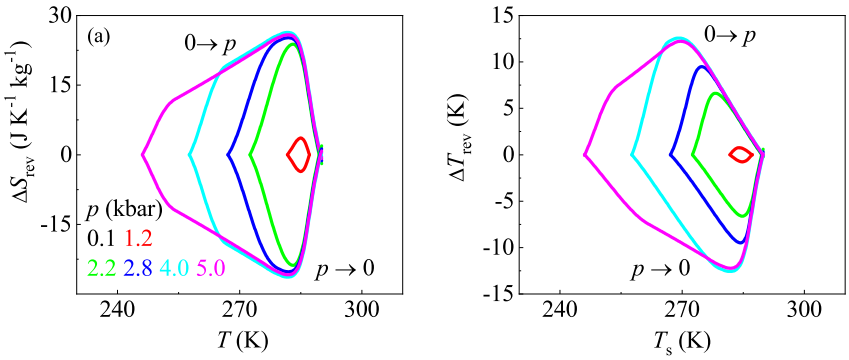

Figure 5.7: Reversible barocaloric effects of $MnCoGeB_{0.03}$ at different pressure changes.

5.3 Mn_3NiN and $Mn_3(Zn_{0.45}In_{0.55})N$

Mn_3NiN and $Mn(Zn_{0.45}In_{0.55})N$ will be presented in the same section due to their equivalent magnetostructural phase transition. Both compounds are magnetic alloys which belong to the antiperovskite Mn-based family Mn_3AN.

Upon heating, Mn_3NiN experiences a magnetic isostructural transition with negative volume changes. At both high- and low-temperature phases Mn_3NiN is arranged in a cubic lattice with $Pm\bar{3}m$ space group (crystallographic parameters summarized in Table 5.2). Upon cooling from the high-temperature PM state, at[5] $T_N^{I\to II} = 257.5$ K, a magnetovolumic phase transition occurs where the unit cell volume abruptly increases and the magnetic dipoles reorder into an antiferromagnetic (AFM) state. More precisely, Γ^{5g} and Γ^{4g} magnetic structures are observed (Fig. 5.8). Both of them present an AFM disposition, where Γ^{4g} has a component out of plane which produces a non null magnetic moment. Upon further cooling, the Mn magnetic dipoles reorient in the [111] plane, coming from a combination of Γ^{4g} and Γ^{5g} magnetic structures to a dominant Γ^{5g} one [151–154]. The reported volume changes associated with the phase transition between PM $\rightleftarrows$ AFM phases, exhibit $|\Delta V_t|/V_I \sim 0.4\%$ accompanied with a shrinkage of the lattice parameter of $|\Delta a| = (4.5 \pm 0.5)\ 10^{-3}$ Å^3 [153], which is considerably small compared to those obtained from other antiperovskite Mn-Ni materials, such as for the Mn_3GaN with

[5]Note that the Néel temperature (T_N) is analogous to T_C but for AFM-PM transitions.

results of $|\Delta V_t|/V_I \sim 1$ % [155]. In spite of the smaller volume changes, higher BC effects are obtained.

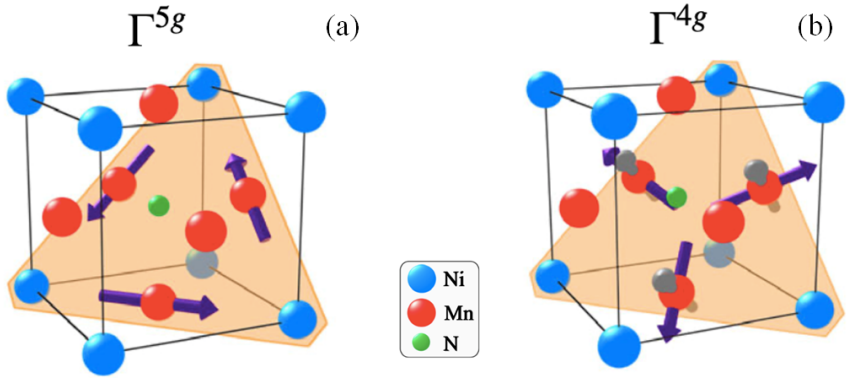

Figure 5.8: (a) Γ^{5g} and (b) Γ^{4g} magnetic structures of Mn_3NiN. Purple arrows indicate the AFM alignment of the Mn magnetic dipoles. Additionally, in the Γ^{4g} phase, the out of plane component is shown with gray arrows. Extracted from Ref. [152].

Phase II (220 K)	Phase I (300 K)
cubic ($Pm\bar{3}m$) AFM	cubic ($Pm\bar{3}m$) PM
a = 3.89062(3) Å	a = 3.88732(3) Å
Z = 1	Z = 1

Table 5.2: Lattice parameters of Mn_3NiN [154].

Similarly to the aforementioned Mn_3NiN, $Mn_3(Zn_{0.45}In_{0.55})N$ presents an equivalent magnetovolumic phase transition. The quaternary alloying allows to tailor the magnetic transition temperature to occur near room temperature for applications in refrigeration [156–158]. This is not the case of ternary alloys, which are observed to have their transition temperature under room temperature [159].

Phase II (10 K)	Phase I (315 K)
cubic ($Pm\bar{3}m$) AFM	cubic ($Pm\bar{3}m$) PM
a = 3.9475 Å^a	a = 3.94 Å^b
Z = 1	Z = 1

Table 5.3: Lattice parameters for $Mn_3(Zn_{0.45}In_{0.55})N$, where ^{a} has been obtained by neutron powder diffraction refinement (Imperial College) and ^{b} from dilatometry.

$Mn_3(Zn_{0.45}In_{0.55})N$ presents a cubic lattice with $Pm\bar{3}m$ space group at all temperatures (crystallographic data are summarized in Table 5.3). Upon cooling at $T_N^{I\rightarrow II} = 308$ K it undergoes a magnetic transition with positive volume changes of $|\Delta V_t|/V_I \sim 1$ %. Analogously to Mn_3NiN, it presents a high-temperature PM phase, where Mn magnetic moments rotate towards an AFM disposition ordered as an Γ^{5g} structure (Fig. 5.8a). The same magnetic structure is found for Mn_3ZnN [160] and Mn_3InN [161], therefore also Γ^{5g} structure is preserved after alloying.

Results

Samples were synthesized at Imperial College of London[6] and used as received. In order to compute the unit cell volume variation as a function of temperature, neutron powder diffraction (performed also by collaborators from Imperial College[6] at the HRPD beamline at the ISIS neutron source, UK), and dilatometry have been carried out for Mn_3NiN and $Mn_3(Zn_{0.45}In_{0.55})N$ (Figs 5.9a and 5.9b), respectively. As aforementioned, negative transition volume changes are observed upon heating for both compounds, with also negligible $\left(\frac{\partial V}{\partial T}\right)_p$ values out of the phase transformation. Therefore, according to the Clausius-Clapeyron equation, inverse BC effects are expected. It is important to highlight that for the specific case of $Mn_3(Zn_{0.45}In_{0.55})N$, a pretransitional range were $\left(\frac{\partial V}{\partial T}\right)_p > 0$ is observed in phase II. In the following lines the incorporation of this pretransitional effect on the quasi-direct method is explained.

Standard and modulated DSC scans have been carried out at p_{atm} in order to obtain calorimetry and heat capacity data[7] [Figs 5.9(c,d) and 5.9(e,f), respectively]. Standard DSC has been performed with temperature rates of $|\dot{T}| = 2$ K min^{-1} and $|\dot{T}| = 5$ K min^{-1} for $Mn_3(Zn_{0.45}In_{0.55})N$ and Mn_3NiN, respectively, which yield values of $|\Delta S_t| = 40 \pm 4$ J K^{-1} kg^{-1} and $|\Delta S_t| = 25 \pm 3$ J K^{-1} kg^{-1} and associated with hysteresis values of ~ 8 K and ~ 2 K. In Table 5.5 measurements of C_p and $(\partial V/\partial T)_p$ are summarized for phases I and II.

[6] Department of Physics, Blackett Laboratory, Imperial College London, London SW7 2AZ, United Kingdom

[7] Heat capacity measurements for $Mn_3(Zn_{0.45}In_{0.55})N$ have also been performed at Imperial College of London

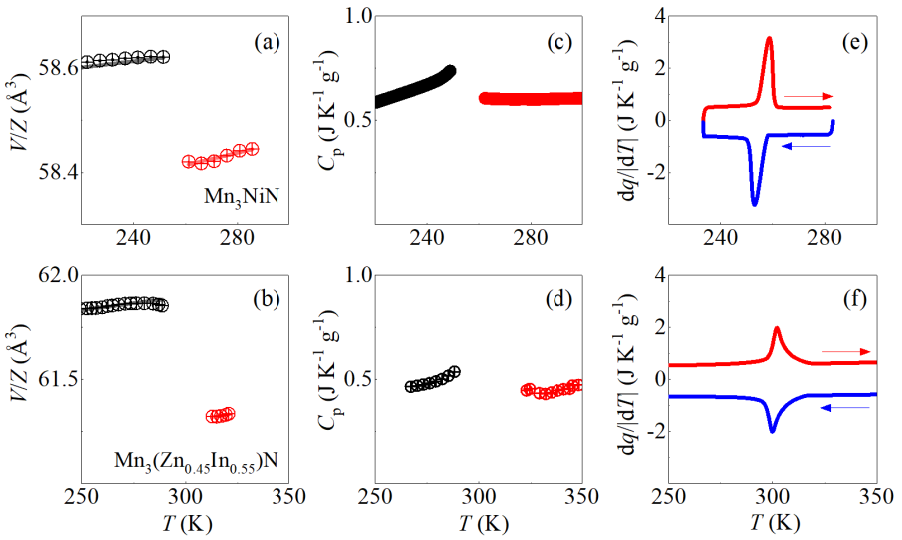

Figure 5.9: Unit cell volume (a,b), heat capacity variation (c,d), and heat flow measurements (e,f) as a function of temperature accordingly for Mn_3NiN and $Mn_3(Zn_{0.45}In_{0.55})N$. Red and blue lines stand for heating and cooling scans and black and red circles for phase II and I measurements, respectively.

Variable-pressure DTA measurements have been carried out up to pressure values of 6 kbar using calorimeter C [Figs 5.10(a,b)]. On the one side, as predicted by $\Delta V_t < 0$, for $Mn_3(Zn_{0.45}In_{0.55})N$ the T_t evolves towards lower temperature values upon applying pressure. On the other side, for the case of Mn_3NiN an anomaly is observed. The measurement performed at p_{atm} agrees with the DSC experiments upon heating and cooling runs. Nonetheless, upon heating scans, the transition temperature seems to increase up to pressures of ~ 2 kbar, while decreases again for $p > 2$ kbar. Conversely, cooling runs present a regular inverse BC behavior. No explanation for this unusual result has been obtained. Therefore, further analysis is required for this material.

From the DTA measurements, the phase diagram is straightforward obtained (Fig. 5.10c and 5.10d), and renders values of $dT_t/dp \sim 3.0$ K kbar^{-1} for Mn_3NiN (between 0-2.5 kbar) and $dT_t/dp \sim 3.0$ K kbar^{-1} for $Mn_3(Zn_{0.45}In_{0.55})N$. By means of peak integration, the pressure dependence of latent heat and transition entropy changes are computed (Fig. 5.11), which derive small pressure dependencies for both of them. In Table 5.6 additional data regarding the phase transfor-

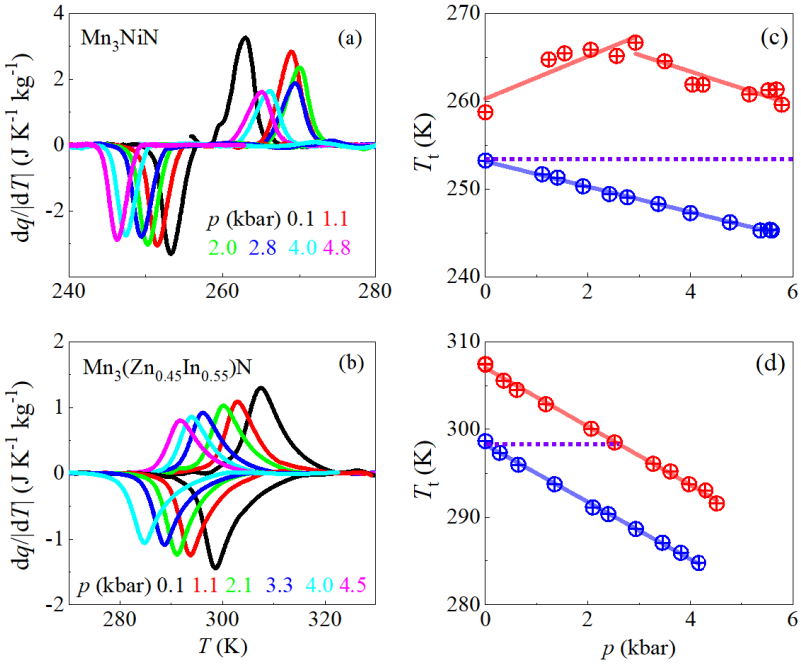

Figure 5.10: High-pressure calorimetry (a,b) and phase diagram (c,d) for Mn_3NiN and $Mn_3(Zn_{0.45}In_{0.55})N$, respectively. Red and blue circles stand respectively for heating and cooling measurements. Lines are fits of the data.

mation are summarized.

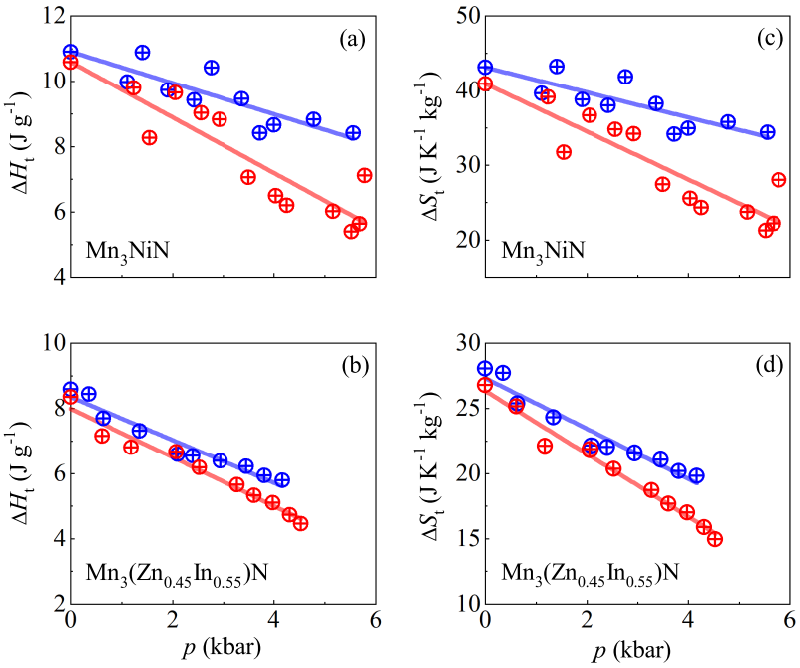

Figure 5.11: Transition enthalpy changes (a) and transition entropy changes (b) as a function of pressure for Mn_3NiN and $Mn_3(Zn_{0.45}In_{0.55})N$. Red and blue circles represent heating and cooling measurements, respectively. Lines are fits of the data.

The quasi-direct and indirect methods have been applied in order to construct the isobaric entropy curves (Fig. 5.14 and Fig. 5.15). In the case of Mn_3NiN, as $\left(\frac{\partial V}{\partial T}\right)_p \approx 0$, according to equation 1.27, the pressure dependence of the heat capacity is $\left(\frac{\partial C_p}{\partial p}\right)_T \approx 0$. Consequently, the atmospheric pressure measurements of C_p can be employed to compute the high-pressure isobaric entropy curves for this alloy, where the entropy value at T_0 is adjusted following equation 1.24. Nonetheless, as shown in Fig. 5.12, $Mn_3(Zn_{0.45}In_{0.55})N$ displays a pretransitional region for which $\left(\frac{\partial V}{\partial T}\right)_p \neq 0$. For this reason, in this case $\left(\frac{\partial C_p}{\partial p}\right)_T \neq 0$ and a special treatment for the heat capacity must be implemented. More precisely, a polynomial fitting of the atmospheric pressure C_p experimental data, previously shifted according to dT_t/dp (Fig. 5.13) has been incorporated into equation 1.23.

The BC performance out of the phase transition has also been evaluated. In Table 5.7 a comparison between the BCEs of $Mn_3(Zn_{0.45}In_{0.55})N$ computed by

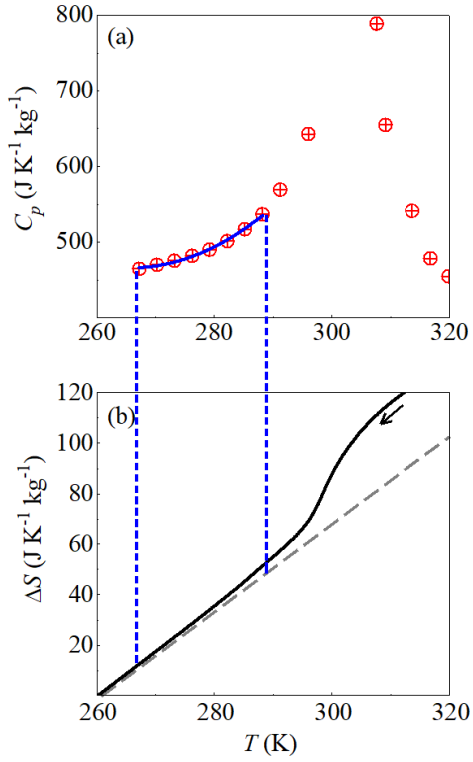

Figure 5.12: $Mn_3(Zn_{0.45}In_{0.55})N$ heat capacity (a) and entropy variation at p_{atm} (b) as a function of temperature. The gray dashed line indicates the entropy trend when the pretransitional contribution is not considered. In panel (a) blue dashed lines point out the heat capacity measurements used to correct the pretransitional contribution.

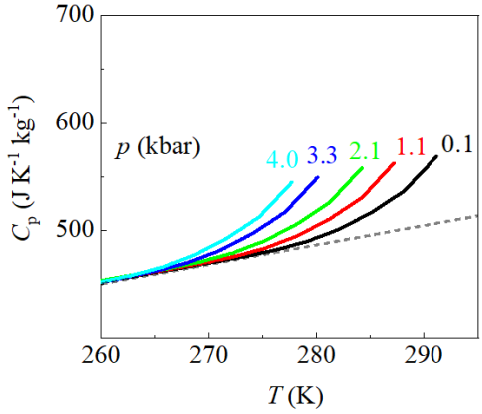

Figure 5.13: Heat capacity shift as a function of pressure according to $\frac{dT_t}{dp}$. Gray dashed line indicates the heat capacity variation without considering the phase transition.

means of method 1 (using equation 1.25) and method 2 (by means of isothermal subtraction of isobaric entropy curves) is displayed.

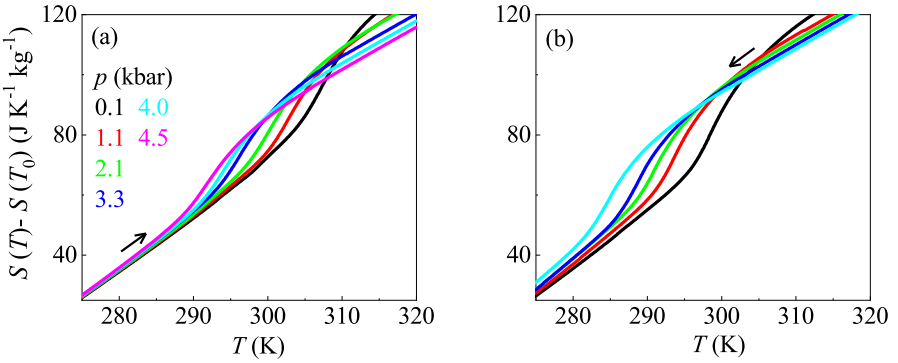

Figure 5.14: Isobaric entropy curves for $Mn_3(Zn_{0.45}In_{0.55})N$ upon heating (a) and cooling (b), where $T_0 = 260$ K.

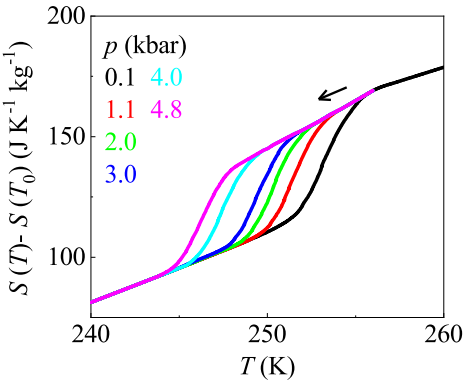

Figure 5.15: Isobaric entropy curves upon cooling for Mn_3NiN, where $T_0 = 220$ K.

By means of isobaric entropy curves subtraction, $\Delta S\,(T, p_{\mathrm{atm}} \rightleftarrows p)$ and $\Delta T\,(S, p_{\mathrm{atm}} \rightleftarrows p)$ upon the first application and removal of pressure have been computed (Fig. 5.16). Only measurements upon removing pressure have been computed for Mn_3NiN due to the aforementioned anomaly. Isothermal entropy changes of $|\Delta S| = 11 \pm 1$ J K^{-1} kg^{-1} and $|\Delta S| = 30 \pm 3$ J K^{-1} kg^{-1} have been respectively achieved for $Mn_3(Zn_{0.45}In_{0.55})N$ and Mn_3NiN, with associated adiabatic temperature changes of $|\Delta T| \sim 2$ K under pressure changes of 2 kbar for both of them. As observed in the phase diagrams, only $Mn_3(Zn_{0.45}In_{0.55})N$ will present reversibility. Therefore, the BC effects driven upon the cyclic application and removal of pressure are computed (Fig. 5.17). In this case the results obtained

reach $|\Delta S_{rev}| = 8 \pm 1$ J K^{-1} kg^{-1} and $|\Delta T_{rev}| = 2.6 \pm 0.3$ K under pressure changes of 4.8 kbar.

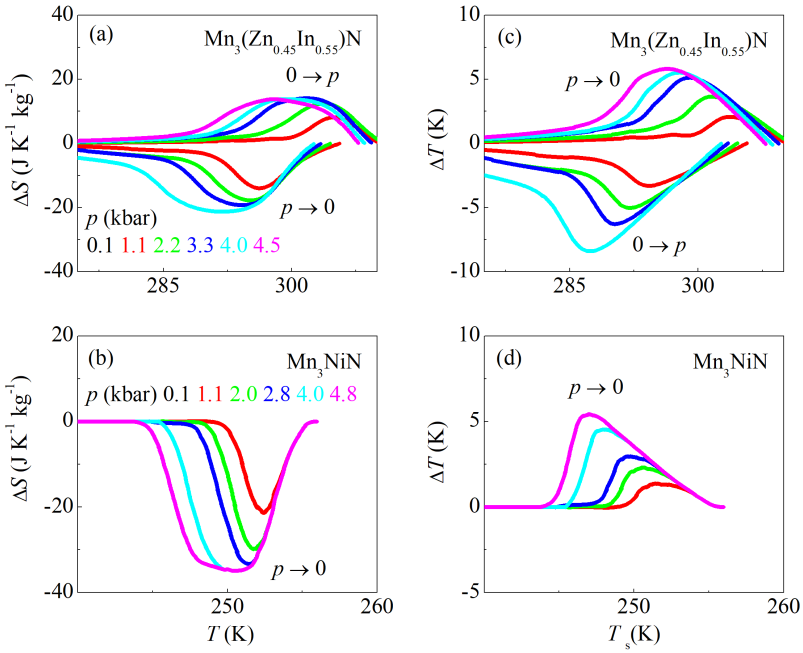

Figure 5.16: Irreversible isothermal entropy changes (a,b) and adiabatic temperature changes (c,d) under different pressure changes for $Mn_3(Zn_{0.45}In_{0.55})N$ and Mn_3NiN, respectively.

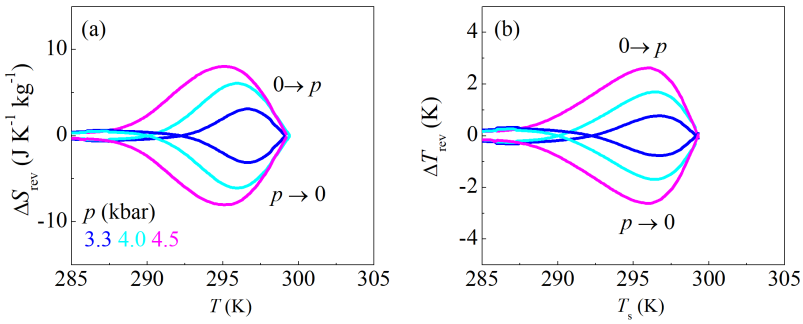

Figure 5.17: Reversible barocaloric effects of $Mn_3(Zn_{0.45}In_{0.55})N$ at different pressure changes.

5.4 $Ni_{50}Mn_{31.5}Ti_{18.5}$

$Ni_{50}Mn_{31.5}Ti_{18.5}$ is a shape memory Heusler alloy[8] fully composed by *d*-metals. Shape memory Heusler alloys are commonly formed by *d*- and *p*- group elements. Nonetheless, it has been recently observed that synthetization of fully *d*-group alloys (in our case Ti incorporation) increases the volume change at the phase transition. Therefore, this family of materials will be more sensitive to pressure changes, anticipating great BC performances [163, 164].

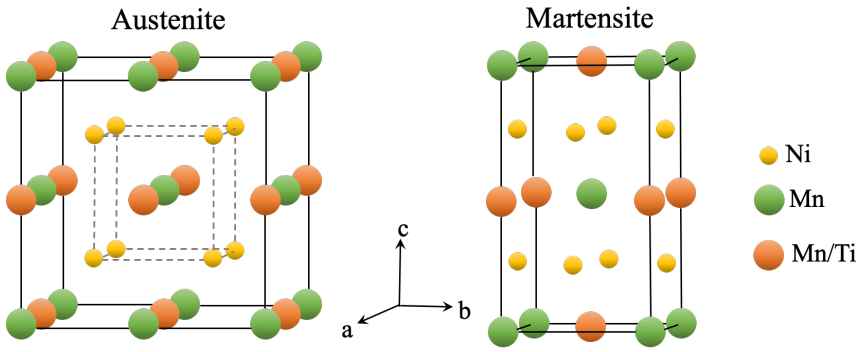

Figure 5.18: Representation of $Ni_{50}Mn_{31.5}Ti_{18.5}$ Heusler alloy in the low- and high-temperature phases (martensite and austenite respectively).

The composition has been tailored in order to tune the transition temperature slightly under room temperature. Then, it is also doped with boron in order to enhance its mechanical properties and grain inter-cohesion [165] resulting in a composition of $(Ni_{50}Mn_{31.5}Ti_{18.5})_{99.8}B_{0.2}$. Nonetheless, for simplicity it will be referred to as $Ni_{50}Mn_{31.5}Ti_{18.5}$. Upon cooling at $T_t^{I\rightarrow II} = 242.8$ K it undergoes a martensitic transition from a PM austenite phase with $Fm\bar{3}m$ space group [166], towards an AFM martensite phase with an orthorhombic crystal lattice with Pmma space group [167]. Further crystallographic information is detailed in Table 5.4. Contrary to the aforementioned magnetic alloys, upon cooling it exhibits remarkable negative volume changes through the phase transformation. For most of magnetic alloys, pressure and magnetic responses compete. For this reason, low ferromagnetic order for phases I and II is preferred in order to minimize the negative

[8] A Heusler alloy corresponds to a magnetic metallic alloy with chemical composition XYZ or X_2YZ in which atoms are arranged in a cubic lattice [162].

contribution of the magnetic entropy against the lattice entropy[9]. [150, 168]

Phase II (200 K)	Phase I (299 K)
orthorhombic (Pmma) AFM	fcc ($Fm\bar{3}m$) PM
a =8.544(43) Å	
b = 5.523(35) Å	a = 5.938(2) Å
c = 4.376(18) Å	Z = 1
Z =1	

Table 5.4: Crystallographic data for $Ni_{50}Mn_{31.5}Ti_{18.5}$.

Results

The sample was synthesized at the University of Science and Technology of Beijing [10] and used as received. In order to compute the unit cell volume variation as a function of temperature, synchrotron X-ray diffraction measurements have been performed at Alba Synchrotron [11] (consult Appendix B). The corresponding data are displayed in Fig. 5.19a, where negligible values of $\left(\frac{\partial V}{\partial T}\right)_p$ are derived out of the phase transition.

Standard and modulated DSC scans have been carried out at p_{atm} in order to obtain calorimetry and heat capacity data, respectively (Fig. 5.19b and 5.19c). More precisely, heat capacity measurements have also been implemented at University of Science and Technology of Beijing[10]. Standard DSC has been performed with temperature rate of $|\dot{T}| = 5$ K min^{-1}, and yield remarkable values of transition entropy changes of $|\Delta S_{\mathrm{t}}| = 86 \pm 5$ J K^{-1} kg^{-1} associated with hysteresis values of ~ 12 K. In Table 5.5 measurements of C_p and $(\partial V/\partial T)_p$ are summarized for phases I and II.

[9] Note that the Clausius-Clapeyron equation for a magnetic transition reads

$$\frac{\mu_0 dH}{dT} = -\frac{\Delta S_{\mathrm{t}}}{\Delta M_{\mathrm{t}}},$$

and the whole entropy contribution for a magnetostructural transition [66]

$$\Delta S_{\mathrm{t}}\,(T, 0 \to p, 0 \to H) = \int_0^p \left(\frac{\partial V}{\partial T}\right)_{0,p} dp + \int_0^H \left(\frac{\partial M}{\partial T}\right)_{H,0} dH + \int_0^p \int_0^H \left(\frac{\partial^2 M}{\partial p \partial T}\right)_{p,H} dH dp.$$

[10] State Key Laboratory for Advanced Metals and Materials, 30 Xueyuan Road, Haidian District, Beijing 100083, People's Republic of China

[11] ALBA Synchrotron, 08290 Cerdanyola del Vallès, Catalonia, Spain

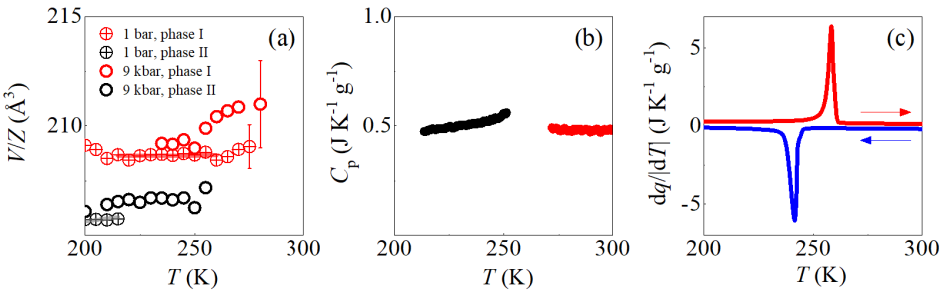

Figure 5.19: (a) Unit cell volume at $\sim$ 1 bar and $\sim$ 9.0 kbar (crossed and empty circles, respectively). Lines correspond to fits of the data. (b) Heat capacity variation where red and black stand for phases I and II, respectively. (c) Heat flow measurements as a function of temperature for $Ni_{50}Mn_{31.5}Ti_{18.5}$. Red and blue accordingly stand for heating and cooling scans. For the sake of clarity only two error bars are shown in (a).

Variable-pressure DTA measurements have been carried out up to pressures of 6 kbar using calorimeter B (Fig. 5.20a). As predicted by $V(T)/Z$ measurements, T_t evolves towards higher temperature values upon applying pressure, rendering results of $dT_t/dp \sim 3.0$ K kbar^{-1} (Fig. 5.20b). By means of peak integration, the pressure dependence of latent heat and transition entropy changes are computed (Fig. 5.21), displaying small pressure dependencies. In Table 5.6 additional data regarding the phase transformation are summarized.

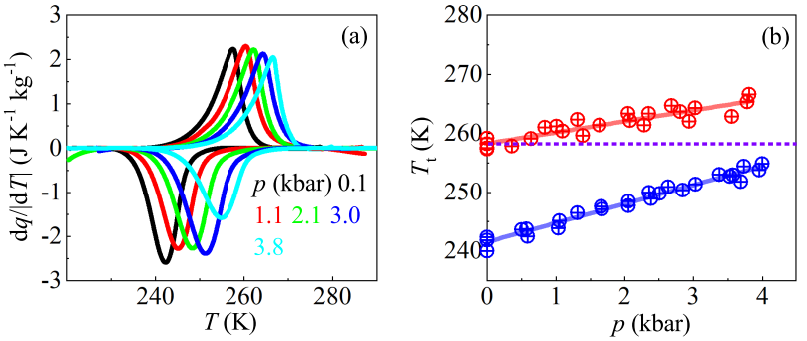

Figure 5.20: High-pressure calorimetry (a) and phase diagram (b) for $Ni_{50}Mn_{31.5}Ti_{18.5}$ where red and blue circles stand for heating and cooling measurements, respectively. Lines are fits of the data.

The quasi-direct and indirect methods have been applied in order to construct the isobaric entropy curves (Fig. 5.22). As for most of the studied compounds, the pressure dependence of the heat capacity is $\left(\frac{\partial C_p}{\partial p}\right)_T \approx 0$ due to the small

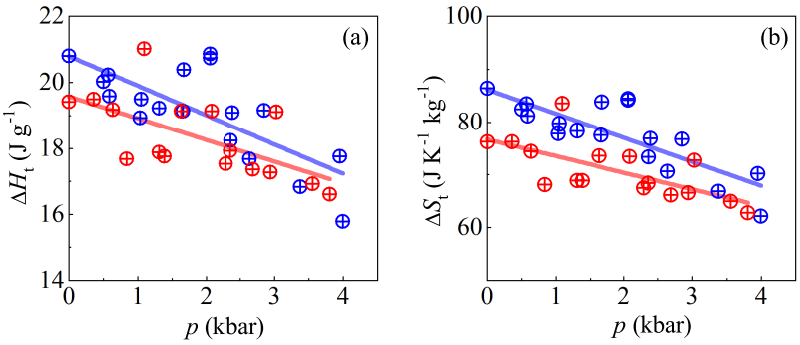

Figure 5.21: Transition enthalpy changes (a) and transition entropy changes (b) as a function of pressure for $Ni_{50}Mn_{31.5}Ti_{18.5}$ where red and blue circles stand for heating and cooling runs, respectively. Lines are fits of the data.

dependence of $V(T)/Z$. Consequently, the atmospheric measurements of C_p can also be employed to compute the high-pressure isobaric entropy curves, where $S(T_0)$ is defined by means of equation 1.24. By means of isobaric entropy curves subtraction, the $\Delta S\,(T, p_{\mathrm{atm}} \rightleftarrows p)$ and $\Delta T\,(S, p_{\mathrm{atm}} \rightleftarrows p)$ upon the first application and removal of pressure have been computed (Fig. 5.23). For instance, results of $|\Delta S| \sim 30$ J K^{-1} kg^{-1} and $|\Delta T| \sim 12$ K have been achieved after pressure changes of 2 kbar. Unfortunately, no reversible results have been obtained due to the high hysteresis exhibited within the temperature range under study. In Table 5.7 a comparison between the BCEs out of the phase transformation computed by means of method 1 (using equation 1.25) and method 2 (by means of isothermal subtraction of isobaric entropy curves) are summarized.

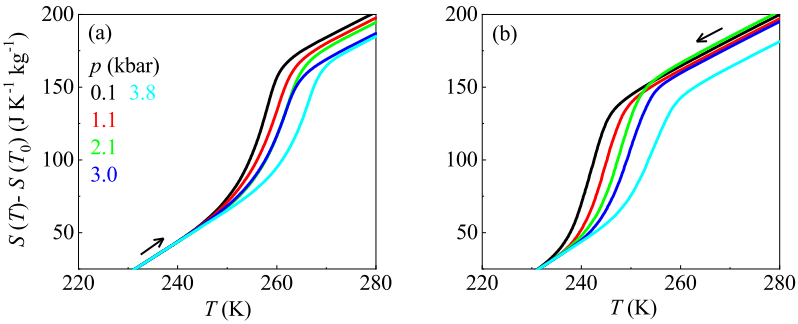

Figure 5.22: Isobaric entropy curves upon heating (a) and cooling (b) for $Ni_{50}Mn_{31.5}Ti_{18.5}$ where $T_0 = 260$ K.

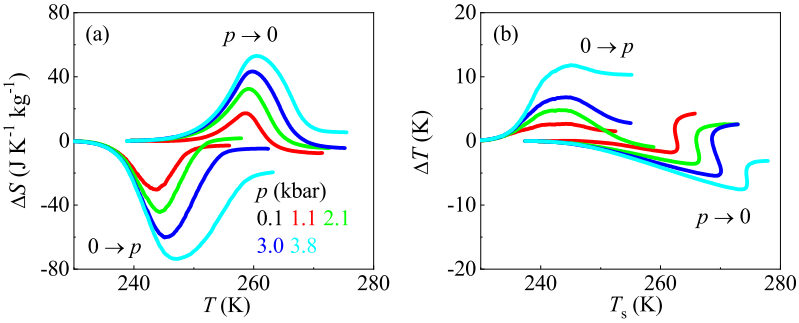

Figure 5.23: Irreversible isothermal entropy changes (a) and adiabatic temperature changes (b) under different pressure changes for $Ni_{50}Mn_{31.5}Ti_{18.5}$.

Compound	Phase	C_p J K^{-1} kg^{-1}	$(\partial V/\partial T)_p$ Å^3 K^{-1}	$(\partial V/\partial T)_p$ cm^3 kg^{-1} K^{-1}
(1)	I	420 ± 50 (328 K)	$(-2.0 \pm 1.0)\,10^{-3}$	$(-8.0 \pm 4.0)\,10^{-3}$
	II	440 ± 50 (274 K)	$(6.0 \pm 1.0)\,10^{-3}$	$(23.8 \pm 4.0)\,10^{-3}$
(2)	I	610 ± 60 (263 K)	$(1.6 \pm 0.3)\,10^{-3}$	$(6.6 \pm 2.0)\,10^{-3}$
	II	700 ± 70 (246 K)	$(7.6 \pm 0.2)\,10^{-4}$	$(3.1 \pm 0.1)\,10^{-3}$
(3)	I	430 ± 50 (332 K)	$(1.3 \pm 0.1)\,10^{-3}$	$(4.4 \pm 0.4)\,10^{-3}$
	II	500 ± 50 (282 K)	$(-6.0 \pm 1.0)\,10^{-3}$	$(-20.1 \pm 4.0)\,10^{-3}$
(4)	I	450 ± 50 (274 K)	$(1.4 \pm 2.0)\,10^{-3}$	$(18 \pm 26)\,10^{-3}$
	II	520 ± 60 (241 K)	$(3.0 \pm 2.0)\,10^{-3}$	$(39 \pm 26)\,10^{-3}$

Table 5.5: Heat capacity and derivative of the unit cell volume with respect temperature for phases I and II. Compounds (1), (2), (3) and (4) stand for $MnCoGeB_{0.03}$, Mn_3NiN, $Mn_3(Zn_{0.45}In_{0.55})N$ and $Ni_{50}Mn_{31.5}Ti_{18.5}$, respectively.

Compound	$\frac{\Delta V_t}{V_I}$ %	Tran.	T_t K	$\frac{dT_t}{dp}$ K kbar^{-1}	$\lvert\Delta H_t\rvert$ J g^{-1}	$\lvert\Delta S_t\rvert$ J (K kg)$^{-1}$	$d(\Delta H_t)/dp$ J (g kbar)$^{-1}$	$d(\Delta S_t)/dp$ J (K kg kbar)$^{-1}$
$MnCoGeB_{0.03}$	4.0	heat.	298.5 ± 0.5	-9.9 ± 0.2	13.4 ± 0.5	46 ± 4	-2.1 ± 0.1	-6.3 ± 0.4
		cool.	284.4 ± 0.5	-9.8 ± 0.1	13.9 ± 0.6	48 ± 4	-2.3 ± 0.2	-7.2 ± 0.5
Mn_3NiN	0.4	heat.	258.7 ± 0.5	-1.7 ± 0.3	10.6 ± 0.5	41 ± 4	-0.9 ± 0.1	-3.2 ± 0.1
		cool.	253.0 ± 0.5	-1.4 ± 0.1	10.9 ± 0.4	43 ± 4	-0.5 ± 0.1	-1.7 ± 0.4
$Mn_3(Zn_{0.45}In_{0.55})N$	0.9	heat.	302.1 ± 0.5	-3.4 ± 0.1	8.2 ± 0.4	26 ± 3	-0.8 ± 0.1	-2.4 ± 0.2
		cool.	299.8 ± 0.5	-3.3 ± 0.1	8.4 ± 0.4	27 ± 3	-0.7 ± 0.1	-1.9 ± 0.2
$Ni_{50}Mn_{31.5}Ti_{18.5}$	1.3	heat.	258.3 ± 0.5	1.9 ± 0.2	20 ± 1	76 ± 6	-0.4 ± 0.2	-2 ± 1
		cool.	241.6 ± 0.5	3.3 ± 0.2	21 ± 1	86 ± 5	-0.9 ± 0.2	-4.7 ± 0.8

Table 5.6: Summary of thermodynamic properties of the first-order phase transition, where $\frac{\Delta V_t}{V_I}$ is relative transition volume change, T_t the transition temperature, $\frac{dT_t}{dp}$ the transition temperature variation as a function of pressure, $|\Delta H_t|$ the transition enthalpy change, $|\Delta S_t|$ the transition entropy change, $d(\Delta H_t)/dp$ the transition enthalpy change as a function of pressure, and $d(\Delta S_t)/dp$ the transition entropy change as a function of pressure.

Compound	p kbar	$\Delta S_{\mathrm{II}}\,(p_{\mathrm{atm}} \to p_1)$ J K^{-1} kg^{-1}	$\Delta S_{\mathrm{I}}\,(p_{\mathrm{atm}} \to p_1)^a$ J K^{-1} kg^{-1}	$\Delta S_{\mathrm{I}}\,(p_{\mathrm{atm}} \to p_1)^{\mathrm{b}}$ J K^{-1} kg^{-1}
(1)	1.1	2.2 ± 0.5	0.5 ± 0.1	4 ± 5
	2.1	4 ± 1	0.9 ± 0.1	6 ± 5
	3.3	7 ± 2	1.5 ± 0.2	7 ± 5
	4.0	8 ± 2	1.8 ± 0.2	9 ± 5
(2)	1.1	4 ± 3	2 ± 3	5 ± 6
	2.1	8 ± 6	4 ± 6	8 ± 7
	3.0	12 ± 8	6 ± 8	15 ± 9
	3.8	15 ± 10	7 ± 10	18 ± 10

Table 5.7: Comparison between method 1[a] and method 2[b] for computing high- and low-temperature $\Delta S_{\mathrm{II/I}}$ for heating measurements. Compounds (1) and (2) stand for $Mn_3(Zn_{0.45}In_{0.55})N$ and $Ni_{50}Mn_{31.5}Ti_{18.5}$, respectively.

Chapter 6

SUPERIONIC CONDUCTOR AgI

6.1 Introduction

A solid material presents ionic conductivity when one of its ions moves through the interstitial vacancies (liquid-like mobility) while the others remain in the center positions of the crystal lattice. Materials showing ionic conductivity can be used as electrolytes, and consequently can be found in applications based on electrochemical cells (e.g. batteries [169]). A superionic conductor is defined as a compound which exhibits ionic conductivities above $\sigma \sim 10^{-1}\ \Omega^{-1}\ \mathrm{cm}^{-1}$ and has activation energies of $\sim 10^{-1}$ eV [170]. Therefore, a superionic phase transition is observed when the ionic conductivity is enlarged/reduced due to changes in the lattice structure.

In this thesis, the barocaloric effects of the well-known silver iodide (AgI) superionic conductor are studied. Its remarkable ionic conductivity has been known for over a century [171]. It can be found as a yellow powder or crystalline solid, and it is currently used as a weather modificator [172, 173] (more precisely as a cloud seeder), as an antiseptic [174] and in photographic supports [175, 176]. Above the superionic phase transition, AgI appears as the α-AgI polymorph, in which the iodine anions are positioned in a bcc cubic lattice with space group $\mathrm{Im}\bar{3}\mathrm{m}$ and the

silver cations hop through the interstitial vacancies [177]. More precisely, the Ag cation has 42 sites available, consisting on 6, 12 and 24 positions for the octahedral, tetragonal and trigonal sublattices per unit cell respectively (Fig. 6.1) [178]. Nonetheless, according to Ref. [179], Ag mainly occupies the 12 positions of the tetragonal sublattice. Notice that disorder is the cause of the aforementioned large ionic conductivity.

Upon cooling, at $T_t = 416$ K it exhibits a first-order phase transition with positive volume changes of $|\Delta V_t|/V_I \sim 5$ %. Due to this volume enlargement, the interstitial positions where the Ag cations flow in the α-AgI polymorph are too large to overcome. Therefore, in the low-temperature phase AgI does not exhibit superionic conductivity, and is in fact, constituted by two polymorphs (β and γ). In β-AgI, the iodine anions are arranged in a hexagonal-close-packed lattice with $P\bar{6}_3mc$ space group, and in γ-AgI they present a cubic-close-packed lattice with $F\bar{4}3m$ space group. In the β and γ polymorphs the silver cations are ordered, therefore, the "melting" of the Ag lattice through the phase transition also implies an order-disorder transformation with huge entropy change which involve potential caloric applications. The lattice parameters are summarized in Table 6.1.

Low-temperature (298 K)	High-temperature (608 K)	$\frac{\lvert\Delta V_t\rvert}{V_I}$
β–AgI[a] hexagonal ($P\bar{6}_3m$) a = 4.59 Å c = 7.73 Å	α–AgI[b] sc ($Im\bar{3}m$) a = 5.09 Å	5 %
γ-AgI[a] s.c ($F\bar{4}3m$) a = 6.493 Å		

Table 6.1: Lattice parameters of α-AgI, β-AgI and γ-AgI polymorphs extracted from Refs. [180][a] and [178][b].

6.2 Results

Powders of AgI were purchased at Sigma Aldrich with 99.999 % purity and used as received. Unit cell volumes for all polymorphs were determined by means

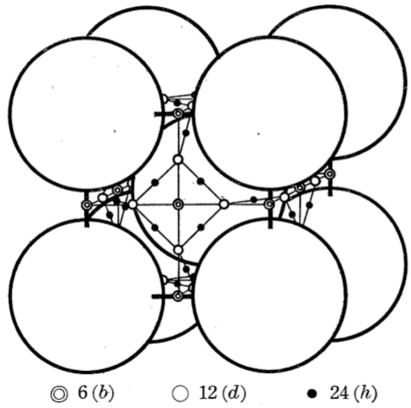

Figure 6.1: α-AgI structure. The double, empty and filled dots show the corresponding positions of the octahedra, tetrahedra and trigonal sublattices, respectively. Extracted from Ref. [178].

of X-ray diffraction and were obtained from Ref. [181] (Fig. 6.2a). Under the superionic phase transition ($T_t < 420$ K), the difference in unit cell volumes of β-AgI and γ-AgI polymorphs can be considered negligible. For the α-AgI, the volume dependence with temperature is slightly higher but still insignificant (see Table 6.2). Therefore, a priori small pressure dependencies of transition latent heat and entropy changes are expected.

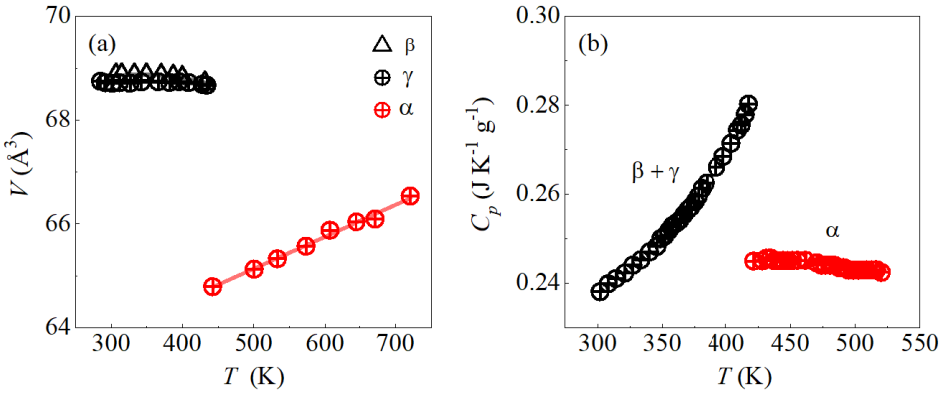

Figure 6.2: Unit cell volume (a) and heat capacity (b) with respect to temperature (from Ref. [181] and Ref.[182] respectively).

Standard DSC measurements were performed in order to obtain calorimetry data at p_{atm} with temperature rates of 2 K min^{-1} and 5 K min^{-1} (Fig. 6.3). It is observed that the transition temperature range (peak widening) also

	β-AgI	γ-AgI	α-AgI
C_p (J K^{-1} kg^{-1})	270 ± 30 (400 K)		250 ± 30 (425 K)
$(\partial V/\partial T)_p$ (Å^3 K^{-1})	$(-10.3 \pm 3.0)\ 10^{-4}$	$(-2.0 \pm 1.0)\ 10^{-4}$	$(61.6 \pm 3.0)\ 10^{-4}$
$(\partial V/\partial T)_p$ (cm^3 K^{-1}kg^{-1})	$(-2.6 \pm 0.7)\ 10^{-3}$	$(-5.1 \pm 3.0)\ 10^{-4}$	$(15.8 \pm 0.6)\ 10^{-3}$

Table 6.2: Heat capacity and derivative of the unit cell volume and specific volume with respect to T for each AgI polymorph.

increases at higher rates, from which values of $|\Delta H_t| = 27 \pm 1$ J g^{-1} and $|\Delta S_t| = 64 \pm 5$ J K^{-1} kg^{-1} have been obtained upon heating runs. Furthermore, large hysteresis values of ~ 25 K (at $|\dot{T}| = 2$ K min^{-1}) are derived. The modulated DSC measurement which yields the C_p was obtained from Ref. [182] (Fig. 6.2b). Additional data is summarized in Table 6.2.

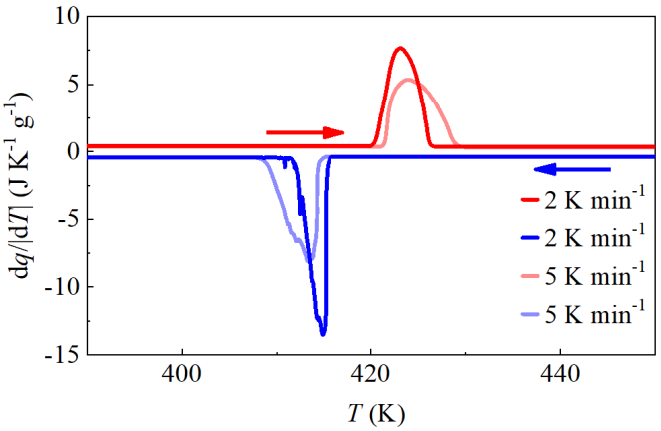

Figure 6.3: Standard DSC measurements performed at rates of 2 K min^{-1} and 5 K min^{-1}.

Pressure-variable DTA measurements have been performed up to 3 kbar (calorimeter A) upon heating and cooling (Fig. 6.4a). As expected, the superionic phase transition shifts towards smaller temperature values upon applying pressure. The phase diagram is straightforward deduced (Fig. 6.4b), from which remarkable values of $dT_t/dp = -14.0 \pm 0.7$ K kbar^{-1} and $dT_t/dp = -12.8 \pm 0.8$ K kbar^{-1} are derived for heating and cooling measurements near p_{atm}, respectively.

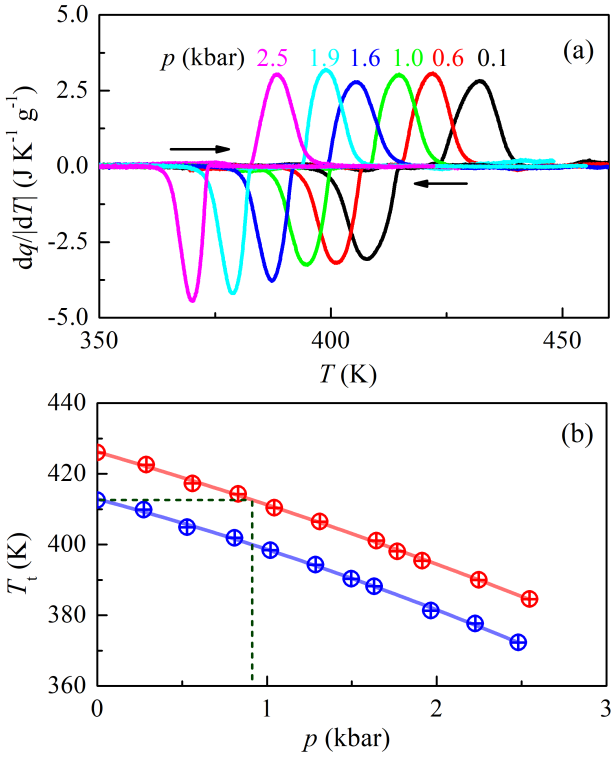

Figure 6.4: (a) Pressure-variable DTA measurements upon heating and cooling. Panel (b) displays the phase diagram deduced from (a) where the red and blue circles stand for heating and cooling measurements. Lines are the corresponding fits of the data.

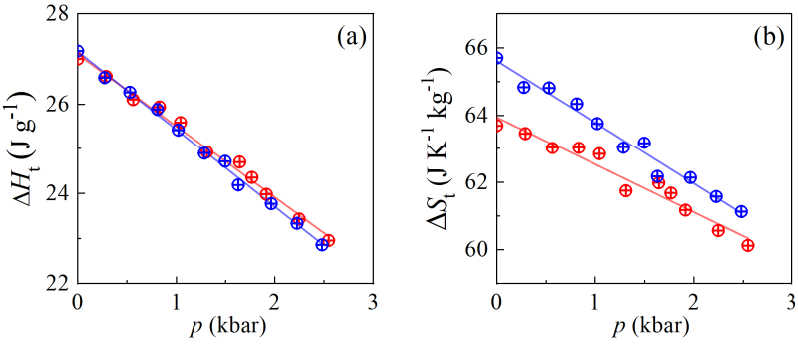

Figure 6.5: (a) Latent heat and (b) transition entropy change as a function of pressure. Blue and red dots stand for cooling and heating measurements. Lines are the corresponding linear fits.

At 2.5 kbar these values increase up to $dT_t/dp = (-18.8 \pm 2.0)$ K kbar^{-1} and $dT_t/dp = (-19.9 \pm 2.0)$ K kbar^{-1} for heating and cooling measurements, respectively. Both $|\Delta H_t|$ and $|\Delta S_t|$ with respect to pressure barely decrease (Fig. 6.5). Small values of $d(\Delta S_t)/dp$ are obtained, which agree with the previously mentioned results of $\left(\frac{dV}{dT}\right)_p$ which imply small BC out of the phase transition and therefore almost invariant $|\Delta S_t|$ with respect to pressure. The ratio of β-AgI and γ-AgI polymorphs remains constant at p_{atm} after the cyclic temperature driven phase transition [183]. In the same way, due to the low pressure dependence of the $|\Delta S_t|$, this ratio is believed to also remain constant under higher applied pressures. The huge $\frac{dT_t}{dp}$ and almost invariant $|\Delta S_t|$ at high pressures are in principle favorable features to obtain good BC performances. Additional information is summarized in Table 6.3.

Tran.	T_t K	$\lvert\Delta H_t\rvert$ J g^{-1}	$\lvert\Delta S_t\rvert$ J (K kg)$^{-1}$	$d(\Delta H_t)/dp$ J (K kg kbar)$^{-1}$	$d(\Delta S_t)/dp$ J (K kg kbar)$^{-1}$	dT_t/dp K kbar^{-1}
II $\rightarrow$ I	426 ± 1	27 ± 1	64 ± 5	-1.6 ± 0.1	-1.4 ± 0.1	-14 ± 1
I $\rightarrow$ II	413 ± 1	27 ± 1	66 ± 5	-1.7 ± 0.1	-1.8 ± 0.1	-13 ± 1

Table 6.3: Calorimetry measurements of AgI upon heating and cooling. T_t is the transition temperature, $|\Delta H_t|$ is the transition enthalpy change, $|\Delta S_t|$ the transition entropy change, $d(\Delta H_t)/dp$ the enthalpy variation with respect to pressure, $d(\Delta S_t)/dp$ the entropy variation with respect to pressure and dT_t/dp is the transition temperature with respect to pressure obtained near p_{atm}.

As the β-AgI and γ-AgI ratio remains constant, it is reasonable to implement the quasi-direct and indirect methods. Nonetheless, if the proportion was not constant, small differences in BC effects would be expected, since there are very small differences between β-AgI and γ-AgI entropies within error [51]. The quasi-direct and indirect methods have been implemented in order to compute the isobaric entropy curves (Fig. 6.6).

As observed in Table 6.4, at the high-temperature phase, the slightly higher values of $\left(\frac{\partial V}{\partial T}\right)_p$ obtained for α-AgI polymorph, which derives $\Delta S_\alpha (p_{atm} \rightarrow p) = \left(\frac{\partial V_\alpha}{\partial T}\right)_p (p - p_{atm})$ (method I) agree with the small isothermal entropy changes derived by the curves subtraction (method II). Additionally, note that the dependence of $V(T)/Z$ with respect to temperature exhibits a linear tendency of $\left(\frac{\partial V}{\partial T}\right)_p$.

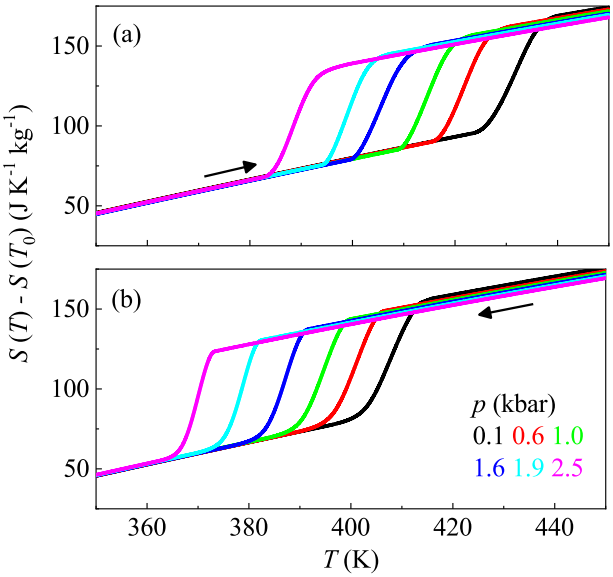

Figure 6.6: Isobaric entropy curves upon (a) heating and (b) cooling. The reference temperature is defined at $T_0 = 290$ K.

Therefore, according to equation 1.27, the heat capacity is not a function of pressure, and the atmospheric pressure measurements of the C_p can be employed in order to compute the high-pressure heat capacity contribution to the entropy.

By means of curves subtraction, $\Delta S(T, p_{\text{atm}} \rightleftarrows p)$ and $\Delta T(S, p_{\text{atm}} \rightleftarrows p)$ are computed after the first application and removal of pressure (Figs 6.7a and 6.7b). For instance, maximum values of $|\Delta S| = 62{\pm}7$ J K^{-1} kg^{-1} and $|\Delta T| = 36{\pm}4$ K after pressure changes of 2.5 kbar have been derived. Upon cyclic application of pressure, these last maximum values decrease to $|\Delta S| = 60{\pm}6$ J K^{-1} kg^{-1} and $|\Delta T| = 18{\pm}2$ K for pressure changes of 2.5 kbar (Figs 6.7c and 6.7d). It is worth noting from the phase diagram that the minimum pressure changes by which reversibility is observed is around 0.75 kbar (Fig. 6.4). Nonetheless, this result is experimentally reported by means of the irreversible entropy curves overlapping at 1.6 kbar with minimum values of $|\Delta S_{\text{rev}}| = 15 \pm 2$ J K^{-1} kg^{-1} and $|\Delta T_{\text{rev}}| = 3.0 \pm 0.3$ K.

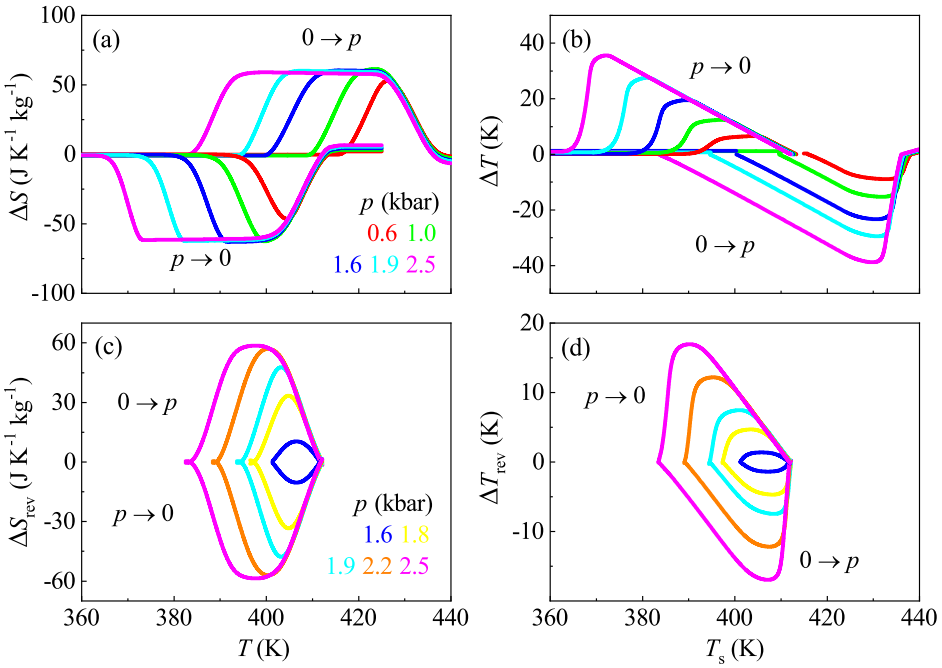

Figure 6.7: Irreversible (a,b) and reversible (c,d) barocaloric effects for different pressure changes.

p kbar	$\Delta S_{\beta/\gamma}\,(p_{\rm atm} \to p_1)$ J K^{-1} kg^{-1}	$\Delta S_{\alpha}\,(p_{\rm atm} \to p_1)^{\rm a}$ J K^{-1} kg^{-1}	$\Delta S_{\alpha}\,(p_{\rm atm} \to p_1)^{\rm b}$ J K^{-1} kg^{-1}
1.0	0.20 ± 0.05	2 ± 1	3 ± 5
1.6	0.24 ± 0.08	3 ± 1	4 ± 5
1.9	0.3 ± 0.1	3 ± 1	5 ± 5
2.5	0.4 ± 0.2	4 ± 2	6 ± 5

Table 6.4: Comparison between Method I[a] and Method II[b] for the $\Delta S_{\alpha}\,(p_{\rm atm} \to p_1)$ estimation. The $\Delta S_{\beta/\gamma}\,(p_{\rm atm} \to p_1)$ has been computed using the mean value of $\left(\frac{\partial V}{\partial T}\right)_p$ for β-AgI and γ-AgI polymorphs.

Chapter 7

DISCUSSION

The aim of this chapter is to compare the barocaloric effects for all compounds studied in this thesis, and to analyze them in relation to the other already known BC materials. For this reason, the most relevant results will be presented jointly with other reported values from literature. In Fig. 7.1, 7.2, and 7.3, the reversible adiabatic temperature changes ($|\Delta T^{\mathrm{rev}}_{\mathrm{max}}|$), reversible isothermal entropy changes ($|\Delta S^{\mathrm{rev}}_{\mathrm{max}}|$) and refrigerant capacity (RC) are represented respectively with respect to pressure change ($p_{\mathrm{atm}} \rightarrow p$). The coefficient of refrigerant performance (CRP) is displayed with respect to maximum values of ΔT_{rev} and ΔS_{rev} in Fig. 7.4 and with respect to RC at constant pressure in Fig. 7.5. Additionally the temperature span (T_{span}) for plastic crystals, hybrid perovskites, magnetic alloys and AgI are shown in Fig. 7.6 - 7.10 separately. The corresponding irreversible BCEs are attached in Appendix C along with the CRP with respect to pressure changes.

Apart from the BC results, other important properties such as thermal conductivity (κ), density (ρ), economic availability and toxicity features are discussed, since real applicability to future refrigeration setups must be considered. The barocaloric performances and their respective feasibility are commented in the following lines for each material family separately.

Magnetic alloys: Caloric effects were first observed in magnetic alloys after the application and removal of magnetic field. Remarkable magnetocaloric effects

have been obtained so far such as for $Gd_5(Si_2Ge_2)$ [23] or $MnAs_{1-x}Sb_x$[184] among others [185]. Nonetheless, in general, poor mechanical properties are displayed after cycling. Sample fragmentation [186, 187] usually caused by considerably high transition volume changes, implies challenging real technological applications in some cases. The strong coupling between magnetic and structural degrees of freedom demonstrated non-negligible mechanocaloric effects, with remarkable elastocaloric [188, 189] and barocaloric performances, which in some cases render competitive results with those obtained for magnetocaloric [20, 22, 49]. Brittleness is no longer an issue when contemplating a possible barocaloric device, since rupture favors the thermal contact with the pressure-transmitting fluid. Therefore, powdered samples can also be employed.

For all the magnetic alloys studied in this work, only $MnCoGeB_{0.03}$ and $Mn_3(Zn_{0.45}In_{0.55})N$ present reversible performances. $(Ni_{50}Mn_{31.5}Ti_{18.5})_{99.8}B_{0.2}$ renders the highest irreversible BCEs among the shape memory alloy family studied so far (comparative Table in Ref. [150]). Its results are only comparable with those of hexagonal Ni_2In-type Mn-Co-Ge compounds [190]. However, reversible BCEs are not expected under applied pressures of $p < 4$ kbar. For this reason its caloric performance will not be further discussed in this chapter. A similar issue concerns Mn_3NiN. Although giant irreversible BCEs are obtained, no reversible results have been computed in this case due to the non-reliable heating measurements.

The reversible BCEs exhibited by $MnCoGeB_{0.03}$ and $Mn_3(Zn_{0.45}In_{0.55})N$ compete with those obtained for other magnetic alloys [20, 191, 192]. Values of $|\Delta S^{\mathrm{rev}}_{\mathrm{max}}|$ for $MnCoGeB_{0.03}$ and $Mn_3(Zn_{0.45}In_{0.55})N$ converge at pressure changes of $\sim$2.3 kbar and $\sim$4.0 kbar, respectively, to entropy changes of $\sim$26.5 J K^{-1} kg^{-1} for both compounds. It is worth mentioning the small $p_{\mathrm{rev}} \sim 1.0$ kbar for $MnCoGeB_{0.03}$, which rapidly derives the aforementioned BCEs. Also, large pressure sensitivity of T_{t} for $MnCoGeB_{0.03}$ derives huge $|\Delta T^{\mathrm{rev}}_{\mathrm{max}}|$, which compare to the plastic crystal NPG result. Likewise, it is interesting to highlight the T_{span} obtained, associated with minimum reversible entropy and temperature variations of $\sim$20 J K^{-1} kg^{-1} and $\sim$8 K, respectively. Therefore similar RC results to ammo-

nium sulfate and $Fe_{49}Rh_{51}$ have been obtained for both compounds, which conversely, due to the particularly large transition volume changes of $MnCoGeB_{0.03}$, yield small values of CRP.

Aside from the BCEs reported here, it is important to comment on the giant thermal conductivity of $\kappa \sim 5$ W m^{-1} K^{-1} for $MnCoGeB_{0.03}$ compared to other giant BC materials [193]. The thermal conductivity of Mn_3NiN has not been specifically reported in literature, but for antiperovskite manganese nitrides with chemical formula $Mn_3Ga_{1-x}Sn_xN$ values of $\kappa \sim 3.2$ W m^{-1} K^{-1} at room temperature have been reported [194]. Therefore, similar κ is expected for Mn_3NiN, which in conjunction with the general values of κ for materials undergoing magnetostructural transitions [195–197], display positive results regarding their applicability. Also their high densities enable more compact devices jointly wasting smaller volume amounts of the solid refrigerant. In spite of the last mentioned benefits, metals are in general expensive elements and in some cases may be hazardous.

Hybrid organic-inorganic perovskites: These compounds are characterized for its extensive chemical variability which leads to many different physical properties. Recently, studies performed for [TPrA][Mn(dca)$_3$] [198] and $(CH_3)_2NH_2Mg(HCOO)_3$ [199] proved that BCEs are among the HOIPs promising features. Their good performances of $|\Delta S| \sim 40$ J K^{-1} kg^{-1} under small pressure changes for both materials encouraged further research in this topic. Generally for HOIPs, the high values of transition entropy changes arise from the order/disorder contribution, which in turn anticipate huge BCEs.

The HOIPs studied in this thesis correspond to [TMA]($Mn(N_3)_3$) and [TMA]$_2$($NaFe(N_3)_6$). They show remarkable results of $|\Delta S^{\mathrm{rev}}_{\mathrm{max}}|$ converging to maximum values of ~ 100 J K^{-1} kg^{-1} under small applied pressures of ~ 1.0 kbar, which exceed the BCEs obtained for other HOIPs so far. Additionally, they show small hysteresis values and high pressure sensitivity of T_{t}. Consequently, reversibility is observed under small applied pressures for both materials (~ 0.1 kbar). In addition to that, huge values of $\frac{dT_{\mathrm{t}}}{dp}$ straightforward imply huge values of $|\Delta T^{\mathrm{rev}}_{\mathrm{max}}|$, reaching the highest temperature variations studied in this work. Likewise, outstanding T_{span} are derived, associated with values of $|\Delta S^{\mathrm{rev}}_{\mathrm{min}}|$ and $|\Delta T^{\mathrm{rev}}_{\mathrm{min}}|$ up to

120 J K^{-1} kg^{-1} and 20 K, respectively, for both materials. Hereon, good values of RC and CRP are obtained, where the CRP is observed to decrease with respect to other materials due to the high transition volume changes exhibited.

Despite of the good BC performances described in the last paragraph, some aspects should be improved in these materials. HOIPs in general present small values of thermal conductivity around $\kappa \sim 1$ W m^{-1} K^{-1} [200–202], and their porosity does not favor heat transfer. Also, some toxicity issues must exist, due to the unsafe synthetization [203] or to the lead presence in some compounds [204]. Nonetheless, the chemical variability may contribute to overcome the hazardous concerns.

Superionic conductor AgI: This thesis presents the first experimental BC studies for superionic conductors. The good performances obtained for AgI motivated further BC research for other materials such as Li_3N[205] or computational predictions for $Cu_{2-x}Se$ compounds [206]. In this case, the BC interest for AgI originated from the high transition entropy changes yielded by the occupational order/disorder of Ag^+ ions though the phase transformation. More specifically, the reduction of the unit cell volume through the endothermic transition allows the ion disorder, and consequently the superionic conductivity emerges.

AgI shows inverse BCEs with great values of $|\Delta S^{\text{rev}}_{\text{max}}|$ up to $\sim$50 J K^{-1} kg^{-1}. Its high density of 5.7 g cm^{-3} makes this compound one of the most remarkable in terms of normalized entropy changes. It rapidly converges to $\sim$0.3 J K^{-1} cm^{-3} under pressure changes of 2.0 kbar. Hysteresis of $\sim$25 K is responsible of reversible pressure changes of $\sim$1.5 kbar, which is compensated by huge values of $\frac{dT_t}{dp}$ which derive outstanding results of $|\Delta T^{\text{rev}}_{\text{max}}|$ and T_{span}. The former renders temperature spans up to 20 K associated with values of $|\Delta S^{\text{rev}}_{\text{min}}|$ and $|\Delta T^{\text{rev}}_{\text{min}}|$ up to 55 J K^{-1} kg^{-1} and 15 K, respectively. In the same way, outstanding values of RC and CRP are obtained, which in fact, the RC for AgI represents the highest result obtained under pressure changes of 2.0 kbar along with two plastic crystal compounds.

Overall, the BCEs derived for the superionic conductor AgI are striking, which in fact are enhanced by its high density. Nonetheless, small thermal conductivity of $\kappa \sim$0.2 W m^{-1} K^{-1} is observed, which even decreases in the high-temperature

phase due to the reduction of the phonon mean free path caused by the Ag^+ mobility [207]. Given that AgI is mainly used for cloud-seeding, several studies of its potential toxicity for the ecosystem have been carried out [208–210], revealing that some toxic impact must be considered. Furthermore, the high price of AgI may not be economically affordable. For these reasons, further research in BCEs driven in superionic materials is encouraged.

Plastic Crystals: As for the superionic conductor AgI, the first experimental BCEs in plastic crystals were reported in this work. In this case, the huge emergence of orientational disorder through the endothermic phase transition anticipates huge transition entropy changes, which may also result in colossal BCEs. In this thesis, two subfamilies of plastic crystals have been studied: Neopentane (AMP, PG, TRIS, NPA and NPG) and adamantane derivatives (1-ada-ol and 2-ada-ol), which as introduced in the following lines yield the most outstanding BCEs reported so far.

Unfortunately, due to the enormous hysteresis values, plastic crystals presenting the highest irreversible caloric effects, AMP and TRIS, require minimum pressures to achieve reversibility of $p > 6$ kbar. For this reason, only the remaining plastic crystals will be commented in this section. The $|\Delta S^{\mathrm{rev}}_{\mathrm{max}}|$ for the neopentane derivatives PG and NPA are the highest reported so far even considering their low densities. At small pressures, the maximum values converge up to $|\Delta S_{\mathrm{rev}}| \sim 500$ J K^{-1} kg^{-1} entropy changes. Additionally, the pressure sensitivity of T_{t} derives great values of $|\Delta T^{\mathrm{rev}}_{\mathrm{max}}|$ and T_{span}. Consequently, remarkable results of RC and CRP are also obtained, especially for NPA and 2-ada-ol, since small ΔV_{t} are observed for these materials, and consequently, the work required to derive BCEs for certain pressure changes are smaller.

Despite the great BC performances of plastic crystals, some drawbacks hamper their straightforward implementation. First, small thermal conductivities are observed. According to Ref. [211], NPG and PG exhibit $\kappa = 0.24$ W m^{-1} K^{-1} and $\kappa = 0.36$ W m^{-1} K^{-1}, respectively. Similar results are obtained for other plastic crystals such as adamantane with $\kappa \sim 0.2$ W m^{-1} K^{-1} [212], and other adamantane derivatives like 2-adamantanone and 1-cyanoadamantane for which

$\kappa < 1$ W m^{-1} K^{-1} [213]. As aforementioned, plastic crystals present small densities. However, its great BC performances are still the highest observed even when normalized by volume. Additionally, the big hysteresis exhibited may anticipate considerable p_{rev} values, which in some cases may only be compensated by high $\frac{dT_{\mathrm{t}}}{dp}$. Lastly, plastic crystals are nowadays vastly used in industry with very competitive prices and non-major toxicologic events. For this reason it is also expected that refrigeration devices based on plastic crystals as solid refrigerants, will be economically affordable. Only irritation issues must be warned when direct human contact is inevitable.

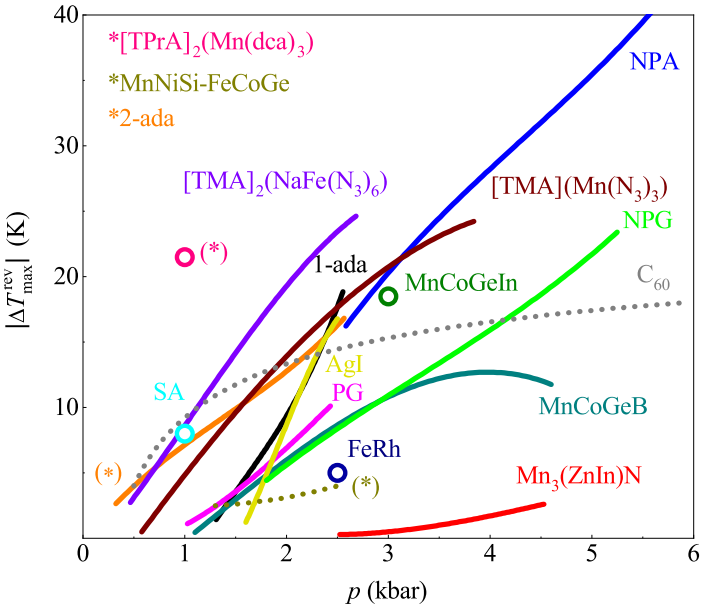

Figure 7.1: Pressure change dependence of $|\Delta T^{\mathrm{rev}}_{\mathrm{max}}|$. Solid lines stand for the compounds studied in this thesis, and dashed lines and empty dots for barocaloric materials obtained from literature.

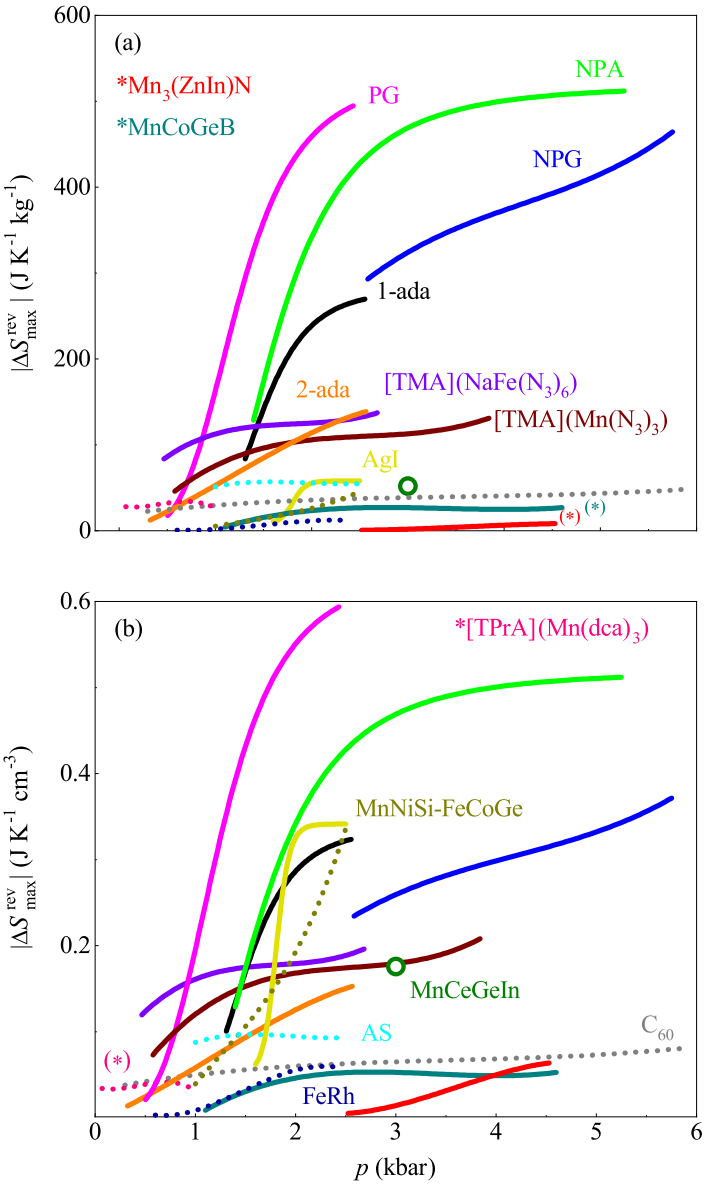

Figure 7.2: Pressure change dependence of the $|\Delta S^{\mathrm{rev}}_{\mathrm{max}}|$ normalized by mass (a) and volume (b). Solid lines stand for the compounds studied in this thesis [labeled in panel (a)], and dashed lines and empty dots for barocaloric materials obtained from literature [labeled in panel (b)].

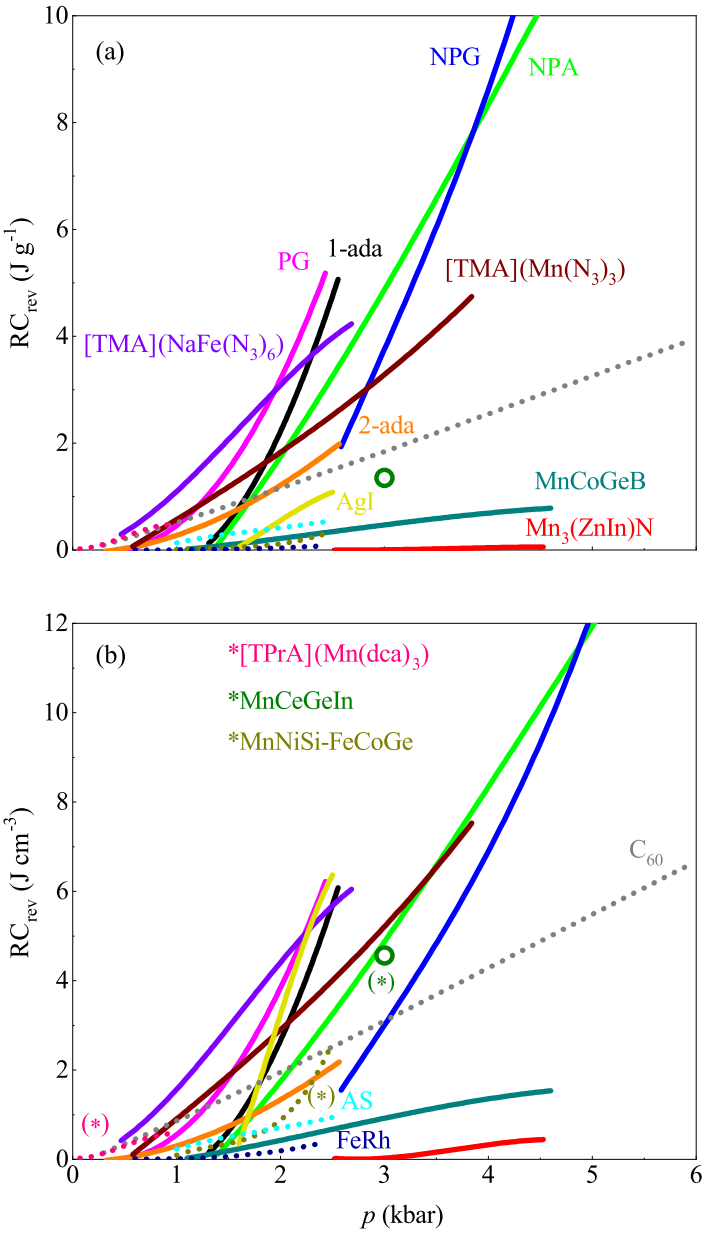

Figure 7.3: Pressure dependence of RC normalized by mass (a) and volume (b). Solid lines stand for the compounds studied in this thesis [labeled in panel (a)], and dashed lines and empty dots for barocaloric materials obtained from literature [labeled in panel (b)].

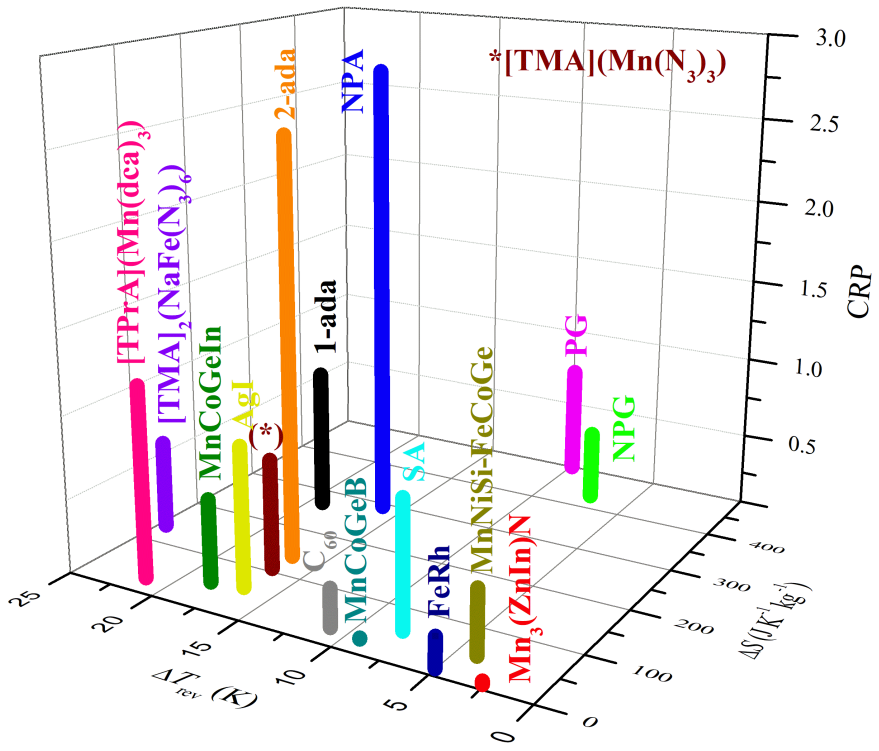

Figure 7.4: CRP at 2.5 kbar [$Mn_3(Zn_{0.45}In_{0.55})N$ has been displayed at 4.5 kbar]. ΔS and ΔT_{rev} stand for the reversible maximum peak values. Only materials presenting reversibility have been considered.

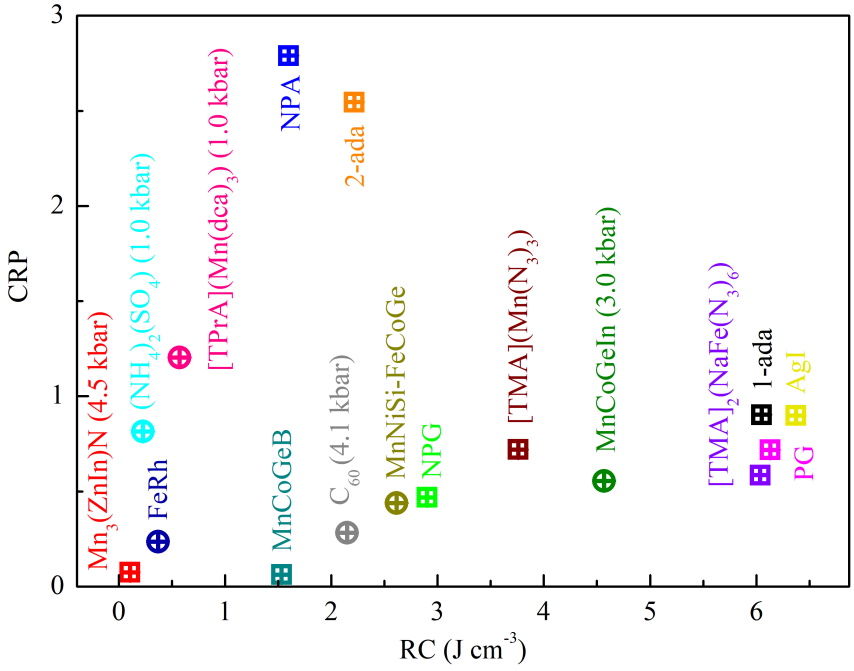

Figure 7.5: CRP with respect to RC for the studied reversible materials (crossed squares) and other barocaloric materials obtained from literature (crossed dots).

Compound	p_{rev} kbar	$\frac{\Delta V_t}{V_I}$ %	$\lvert\Delta T_{rev}^{max}\rvert$ K	$\lvert\Delta S_{rev}^{max}\rvert$ J K^{-1} kg^{-1}	$\lvert\Delta S_{rev}^{max}\rvert$ kJ K^{-1} m^{-3}	RC J g^{-1}	CRP	References
1-adamantanol	1.0	5.0	19 ± 2	270 ± 30	320 ± 40	5.0 ± 0.8	0.9 ± 0.2	This work
2-adamantanol	0.5	0.8	17 ± 2	140 ± 20	150 ± 20	2.0 ± 0.4	2.5 ± 0.4	This work
Neopentyl alcohol	2.0	1.3	16 ± 2	290 ± 30	230 ± 30	2.0 ± 0.7	2.8 ± 0.4	This work
Neopentylglicol	1.6	4.9	7 ± 1	430 ± 50	430 ± 50	2.9 ± 0.6	0.5 ± 0.1	This work
Pentaglycerine	0.4	6.7	10 ± 1	500 ± 50	600 ± 60	5.1 ± 0.7	0.7 ± 0.1	This work
$[TMA]\,(Mn(N)_3)_3$	0.01	4.5	17 ± 2	110 ± 10	170 ± 20	2.4 ± 0.3	0.7 ± 0.1	This work
$[TMA]_2\,(NaFe(N)_3)_6$	0.01	5.4	25 ± 3	140 ± 20	200 ± 20	4.2 ± 0.3	0.6 ± 0.1	This work
$MnCoGeB_{0.03}$	1.0	4.0	9 ± 1	25 ± 3	50 ± 5	0.4 ± 0.1	0.08 ± 0.01	This work
$Mn_3\,(Zn_{0.45}In_{0.55})\,N$ (4.5 kbar)	2.5	0.9	3 ± 1	8 ± 1	60 ± 10	0.05 ± 0.01	0.07 ± 0.01	This work
AgI	0.8	5.0	17 ± 2	58 ± 6	340 ± 40	1.1 ± 0.2	0.9 ± 0.2	This work
$(NH_4)_2\,SO_4$ (1.0 kbar)	0.01	0.9	8	58	93	0.6	1.2	[30]
$MnCoGe_{0.99}In_{0.01}$ (3.0 kbar)	...	3.9	19	52	176	1.4	0.6	[190]
$Fe_{49}Rh_{51}$ (2.5 kbar)	1.0	1.0	5	12	60	0.08 ± 0.02	0.2 ± 0.1	[36]
$[TPrA]\,(Mn(dca)_3)$ (1.0 kbar)	0.01	1.3	22	28	32	0.5	1.2	[198]
$[TPrA]\,(Cd(dca)_3)$ (0.07 kbar)	0.07	...	...	11.5	16	...	...	[214]
$MnNiSi_{0.6}FeCoGe_{0.4}$ (2.3 kbar)	0.3	2.7	4 ± 1	50 ± 5	336 ± 40	0.4 ± 0.1	0.4 ± 0.2	[215]
$MnNiSi_{0.61}FeCoGe_{0.39}$ (2.6 kbar)	0.3	2.7	6 ± 1	44 ± 5	310 ± 40	0.3 ± 0.1	0.6 ± 0.1	[215]
$MnNiSi_{0.59}FeCoGe_{0.41}$ (2.3 kbar)	0.2	2.7	2.0 ± 0.2	24 ± 5	170 ± 40	0.1 ± 0.05	0.10 ± 0.02	[215]
$MnNiSi_{0.62}FeCoGe_{0.38}$ (2.7 kbar)	0.4	3.0	...	57 ± 4	400 ± 40	1.2	-	[216]
C_{60} (4.1 kbar)	0.01	1.0	11 ± 1	31 ± 3	71 ± 7	2.6 ± 0.1	0.3 ± 0.1	[217]

Table 7.1: Maximum values of $|\Delta T_{rev}|$, $|\Delta S_{rev}|$, RC and CRP after pressure changes of 2.5 kbar for materials studied in this thesis. Also, barocaloric solid materials reported in literature are also attached.

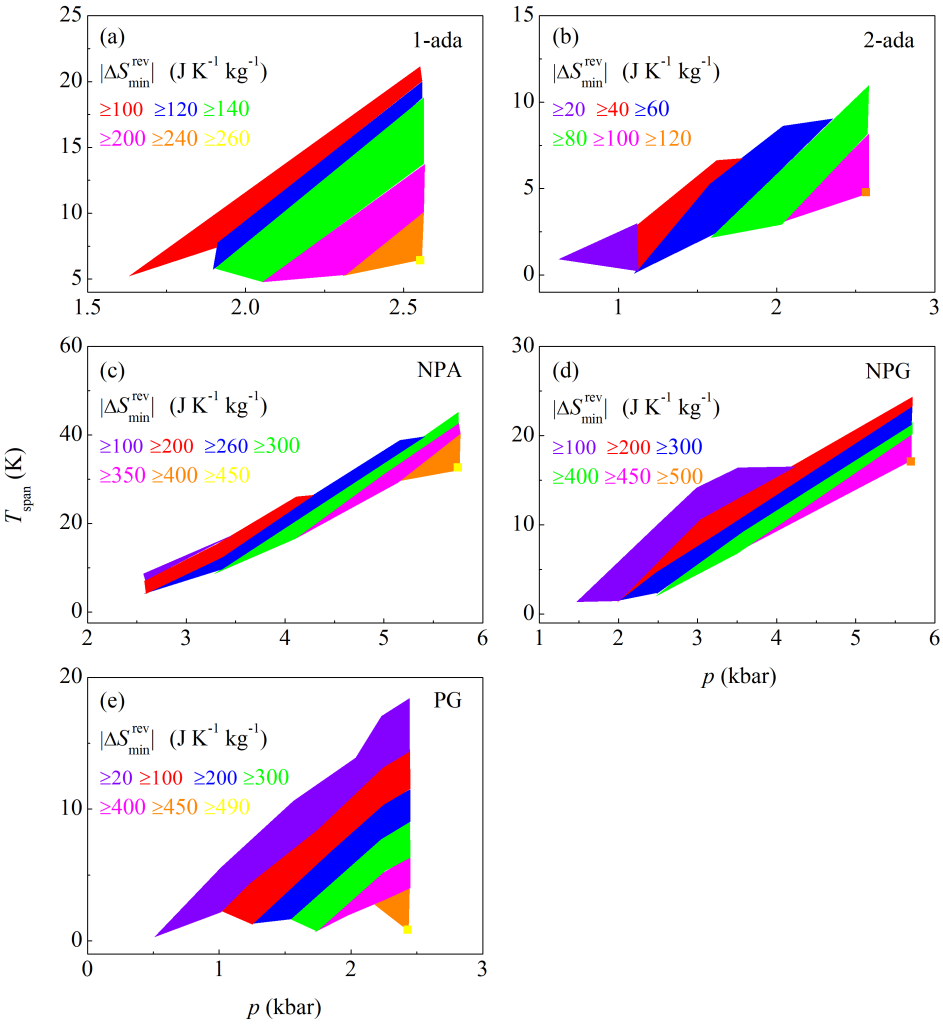

Figure 7.6: T_{span} required in order to achieve the minimum reversible $|\Delta S^{\mathrm{rev}}_{\mathrm{min}}|$ values indicated in the legend for plastic crystals.

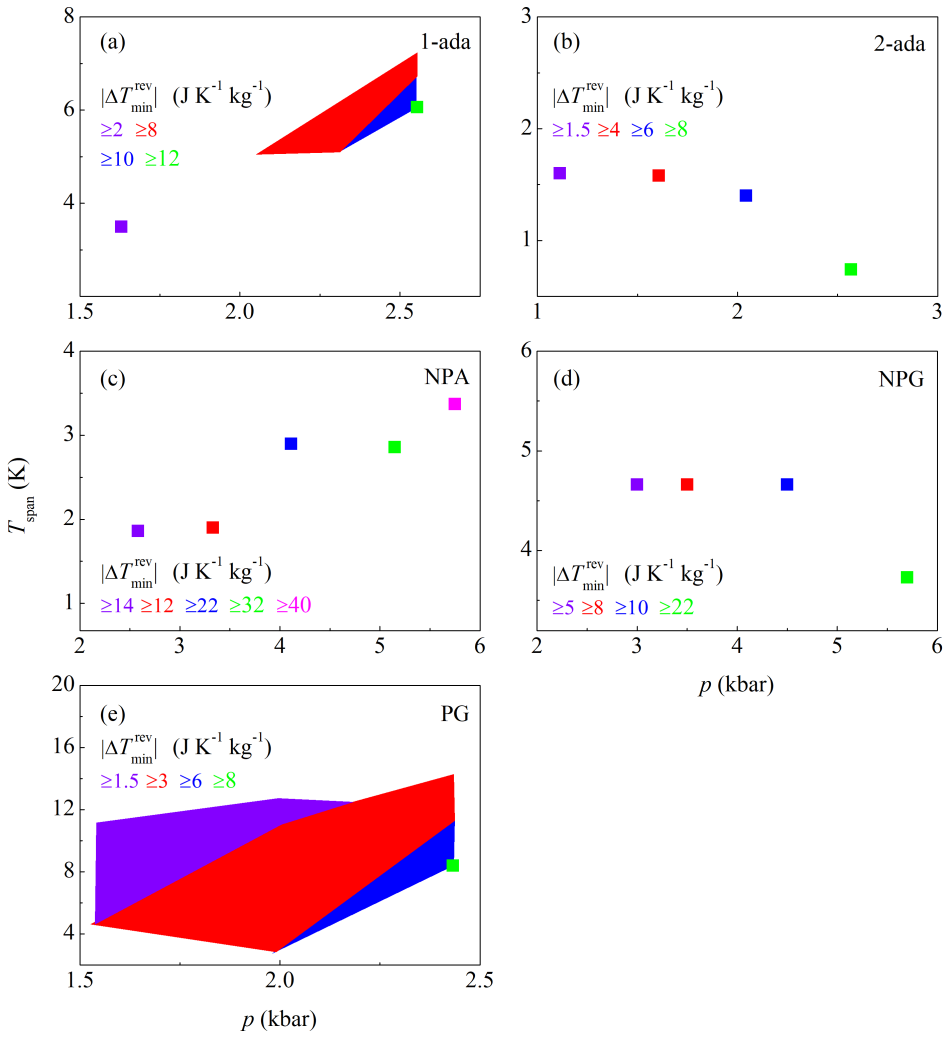

Figure 7.7: T_{span} required to obtain the minimum reversible $|\Delta T_{\mathrm{min}}^{\mathrm{rev}}|$ values indicated for plastic crystals.

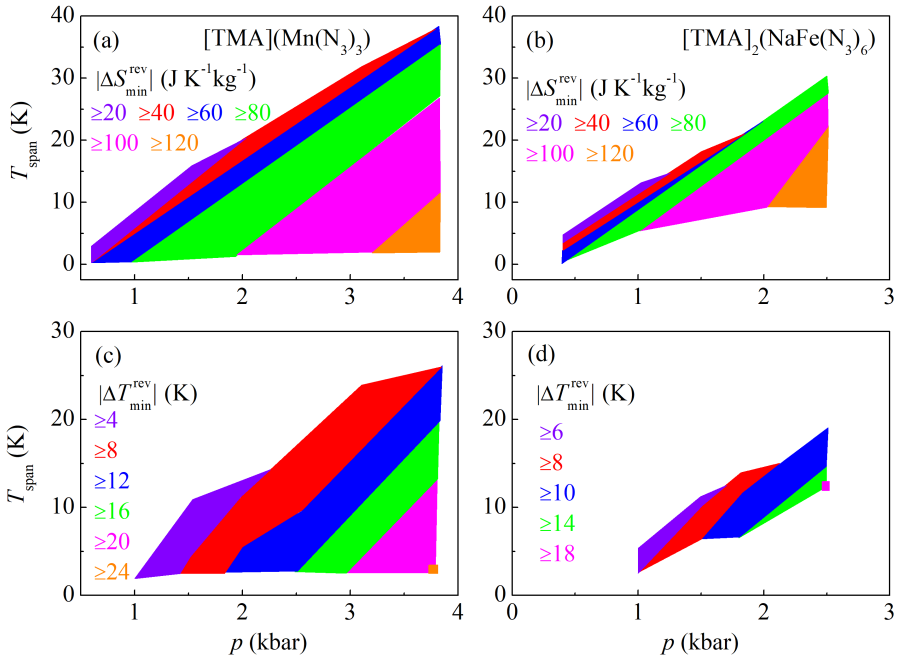

Figure 7.8: T_{span} required to obtain the minimum reversible $|\Delta S^{\mathrm{rev}}_{\mathrm{min}}|$ (a,b) and $|\Delta T^{\mathrm{rev}}_{\mathrm{min}}|$ (c,d) for $[\mathrm{TMA}]\,(\mathrm{Mn(N)_3})_3$ and $[\mathrm{TMA}]\,(\mathrm{NaFe(N)_3})_6$.

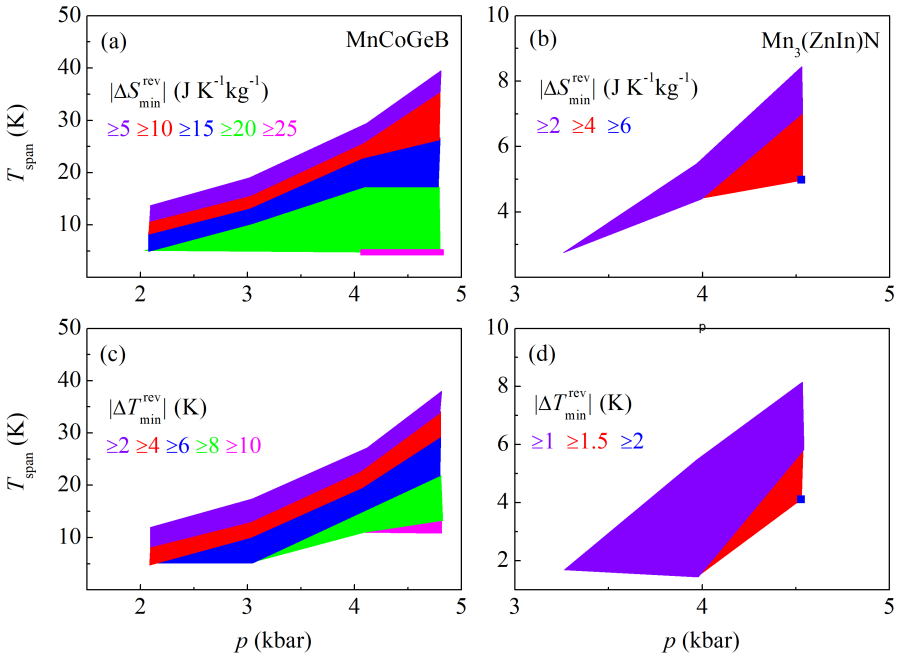

Figure 7.9: T_{span} with respect to the minimum reversible $|\Delta S^{\mathrm{rev}}_{\mathrm{min}}|$ (a,b) and $|\Delta T^{\mathrm{rev}}_{\mathrm{min}}|$ (c,d) for MnCoGeB and $\mathrm{Mn_3\,(Zn_{0.45}In_{0.55})\,N}$.

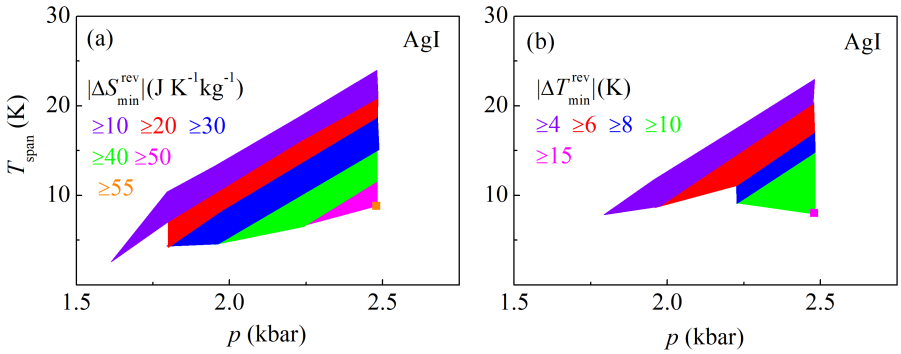

Figure 7.10: T_{span} with respect to the minimum reversible $|\Delta S^{\mathrm{rev}}_{\mathrm{min}}|$ (a) and $|\Delta T^{\mathrm{rev}}_{\mathrm{min}}|$ (b) for AgI.

Chapter 8

CONCLUSIONS

In this dissertation, the barocaloric effects (i.e. changes in temperature or entropy upon applying and removing hydrostatic pressure) through first-order phase transitions of four different families of materials have been studied. In particular, we analyze materials belonging to the family of plastic crystals (PC), hybrid organic-inorganic perovskites (HOIPs), magnetic alloys and one superionic conductor. The election of these materials is not arbitrary, but instead relies on several aspects, such as pressure sensitivity of the transition temperature T_t, and the amount of heat exchanged throughout the transformation, which anticipate good barocaloric performances. In order to determine the barocaloric effects, measurements at atmospheric pressure and high-pressure calorimetry have been performed, along with experiments of X-ray diffraction and dilatometry. By combining the quasi-direct and indirect methods, the barocaloric effects are obtained. Special attention has been put on reversibility, since this is the basis of real cycle applicability. A brief summary of results obtained for the different groups of materials is provided below:

- **Plastic crystals**: This dissertation reports some of the first barocaloric effects observed in plastic crystals. Particularly, we analyze derivatives from adamantane and neopentane. It is shown that the huge transition entropy changes mainly derive from the release of the orientational degrees of freedom

through the order-disorder phase transition, added to the volume contribution, which is minor for the neopentane derivatives. All compounds display conventional colossal barocaloric effects, among which neopentyl alcohol, neopentylglycol, pentaglycerine, 1-adamantanol and 2-adamantanol show reversibility under the pressure range of study (0–6 kbar). Reversible values between 300–500 J $K^{-1}kg^{-1}$ and 150–300 J $K^{-1}kg^{-1}$ have been respectively determined for neopentane and adamantane derivatives, for pressure changes of $\sim$ 2.5 kbar and associated with temperature changes between 10–20 K. These reversible barocaloric effects still present a colossal contribution even when normalized by volume. Plastic crystals are inexpensive materials, but in order to consider them fully applicable, efforts should be put on improving their low thermal conductivity.

- **Hybrid Organic-Inorganic perovskites**: The widespread use of these materials triggered further interest in discovering additional physical properties to take profit from. Presently, conventional barocaloric effects for [TMA]($Mn(N_3)_3$) and $[TMA]_2(NaFe(N_3)_6)$ are one of such properties. For instance, giant entropy and temperature changes of $\sim$ 100 J $K^{-1}kg^{-1}$ and 15–20 K have been derived respectively for pressure changes of 2 kbar for both compounds. Even though these materials show smaller entropy changes than plastic crystals, thermal hysteresis is smaller, and therefore yield reversible barocaloric effects at very small applied pressures of $\sim$ 0.1 kbar, which reaffirm them as very promising candidates. Nonetheless, as for the plastic crystal case, they exhibit small thermal conductivities.

- **Magnetic alloys**: Barocaloric effects of magnetic alloys Mn_3NiN, $Mn_3(Zn_{0.45}In_{0.55})N$, $MnCoGeB_{0.03}$ and $(Ni_{50}Mn_{31.5}Ti_{18.5})_{99.8}B_{0.2}$ have been studied, from which conventional effects have been obtained for Mn_3NiN and $(Ni_{50}Mn_{31.5}Ti_{18.5})_{99.8}B_{0.2}$, and inverse for $Mn_3(Zn_{0.45}In_{0.55})N$ and $MnCoGeB_{0.03}$. Large irreversible barocaloric performances have been derived for all these materials. Nonetheless, reversibility is only observed for $MnCoGeB_{0.03}$ and $Mn_3(Zn_{0.45}In_{0.55})N$, since small results of $\frac{dT_t}{dp}$ imply non-reversible barocaloric effects for the remaining compounds. More precisely,

reversible entropy changes of $\sim$25 J $K^{-1}kg^{-1}$ are exhibited for $MnCoGeB_{0.03}$ and $Mn_3(Zn_{0.45}In_{0.55})N$ for pressure changes of $\sim$ 2 kbar and $\sim$ 4 kbar, respectively, and temperature changes between 4–10 K for pressure changes of $\sim$3 kbar. Reversibility is derived for minimum pressure changes of 1 kbar for $MnCoGeB_{0.03}$, and 2.5 kbar for $Mn_3(Zn_{0.45}In_{0.55})N$. Contrary to the previous mentioned materials, they exhibit good values of thermal conductivity although more expensive synthetization costs due to their metal element composition.

- **Superionic conductor AgI**: Barocaloric effects for a superionic conductor are first ever reported experimentally in this work. The extensively known AgI was chosen for this purpose, since its barocaloric performance was already predicted in literature. The order-disorder phase transformation, from which ionic superconductivity arises, is the main contribution to the high entropy changes exhibited. Outstanding non-conventional reversible entropy and temperature changes of $\sim$50 J $K^{-1}kg^{-1}$ and $\sim$ 10 K have been reported for pressure changes of 2 kbar. When normalized by volume, its barocaloric effects become the most impressive observed in this dissertation. Unfortunately, the minimum pressure to obtain reversibility is considerably high, around 1.5 kbar, and small thermal conductivity is observed. Nonetheless, these results pave the way for future barocaloric research in superionic conductors.

Overall, the studied materials compare favorably with respect to other previously analyzed compounds. Specially results exhibited by PCs, HOIPs, and the superionic conductor AgI, provide useful insight to take into consideration for future work. However, improvements are required during the next years most especially concerning thermal conductivity.

Agraïments

M'agradaria primer de tot agrair al Josep Lluís Tamarit l'oportunitat de fer el doctorat al Grup de Caracterització de Materials de la UPC, i per haver lluitat sempre perquè això hagi sigut finalment possible.

Menció especial li haig de fer al Pol, moltíssimes gràcies pel teu temps, paciència i incansable dedicació durant aquests anys. De tu no només he après la ciència dels efectes barocalòrics, sinó també la constància, l'entrega i el perfeccionisme en la feina. M'emporto molts valors afegits gràcies a tu, vagi on vagi. Gràcies a la Maria, al Roberto i al Luis Carlos, per haver-me acompanyat també durant aquest camí. Agraeixo especialment a la Michela haver-me ensenyat tot el que havia de saber del laboratori de raigs X del Centre Multiescala, i a més a més ser una bona amiga, moltes gràcies pel teu suport! No em puc oblidar tampoc dels meus companys de doctorat: Sofia, Guada, Johnny, Yago i Eda. Sobretot per ser els meus amics dins i fora de la feina. Gràcies pels cafès, *asados*, sopars, cerveses, viatges... M'heu donat *vidilla* tots aquests anys!, i espero que així segueixi.

Gràcies també a tots els col · laboradors, al grup de Materials: Transicions de fase i sistemes multiescala del Departament de Física de la Matèria Condensada de la UB, to the Department of Materials Science and Metallurgy from the University of Cambridge and to the rest of groups which participated in this dissertation. Thanks to everyone!

Tampoc me n'oblido d'en Jordi Llorca i de la resta de companys del centre Multiescala: Trifon, Judit, Montse, Ina, Carla, Sandra i Angelica. La veritat és que m'ho he passat molt bé, espero que perduri la tradició del bar *Casolà*!

A tot l'equip de professors de les assignatures de Física del Campus Besòs. La docència també ha format part de la meva vida diària com a doctoranda. Ha sigut un plaer conèixer-us a tots!

Gràcies als meus amics de tota la vida: Als Marcs, l'Heura i a l'Albert, per romandre després de més de disset anys, i per la confiança durant tot aquest temps. El mateix dic de la Sara, la Iolanda, la Cristina i la Marina, les meves amigues de la carrera. Gràcies per no permetre que es crei la distància. Per moltes més tapes al restaurant xinès, amb *ternera a la shi chuan* i *gyozas*! Gràcies també als meus amics Diego i David! Espero que seguim fent *asados* i viatges a la cerca de més *glühwein* i formatges! Us estimo a tots!

El doctorat també ha tingut impacte en la meva família. Moltes gràcies als meus pares, que sempre m'han donat més del que han pogut i menys del que voldrien. A la meva germana, per deixar-me l'ordinador per acabar la tesi i per ser la millor amiga que tinc. Per acabar, no tinc paraules suficients per agrair-te, Adri, tot el que has fet per mi. Espero no haver-te avorrit gaire. Gràcies per tot el suport emocional, que és innombrable, i sobretot, per ser el meu acompanyant en aquesta vida.

List of Publications

- A. Aznar, P. Lloveras, M. Romanini, M. Del Barrio, J. Ll. Tamarit, C. Cazorla, D. Errandonea, N. Mathur, A. Planes, X. Moya and Ll. Mañosa Carrera, "Giant barocaloric effects over a wide temperature range in the superionic conductor AgI", *Nat. Commun.*, **8**, 1-6 (2017).

- D. Boldrin, E. Mendive-Tapia, J. Zemen, J. B. Staunton, T. Hansen, A. Aznar, J. Ll. Tamarit, M. Del Barrio, P. Lloveras, J. Kim, X. Moya and L. Cohen, "Multisite exchangeenhanced barocaloric response in Mn_3NiN", *Phys. Rev. X.*, **8**, 041035, (2018).

- A. Aznar, A. Gracia-Condal, A. Planes, P. Lloveras, M. Del Barrio, J. Ll. Tamarit, W. Xiong, D. Cong, C. Popescu and Ll. Mañosa Carrera, "Giant barocaloric effect in all-dmetal Heusler shape memory alloys", *Phys. Rev. Mater.*, **3**, 044406, (2019).

- P. Lloveras, A. Aznar, M. Del Barrio, P. Negrier, C. Popescu, A. Planes, Ll. Mañosa Carrera, E. Stern, A. Avramenko, N. Mathur, X. Moya and J. Ll. Tamarit, "Colossal barocaloric effects near room temperature in plastic crystals of neopentylglycol", *Nat. Commun.*, **10**, 1-7, (2019).

- A. Aznar, P. Lloveras, J. Kim, E. Stern, M. Del Barrio, J. Ll. Tamarit, N. Mathur and X. Moya, "Giant and reversible inverse barocaloric effects near room temperature in ferromagnetic $MnCoGeB_{0.03}$", *Adv. Mater.*, **31**, 1903577, (2019).

- A. Aznar, P. Lloveras, M. Del Barrio, P. Negrier, A. Planes, Ll. Mañosa

Carrera, N. Mathur, X. Moya and J. Ll. Tamarit, "Reversible and irreversible colossal barocaloric effects in plastic crystals", *J.Mater. Chem. A.*, **8**, 639–647, (2020).

- A. Aznar, P. Negrier, A. Planes, Ll. Mãnosa, E. Stern, X. Moya, M. Barrio, J. Ll. Tamarit and P. Lloveras, "Reversible colossal barocaloric effects near room temperature in 1-X-adamantane (X=Cl, Br) plastic crystals", *Phys. Rev. Appl.* (under review)

- A. Aznar, W. J. Wei, P. Lloveras, M. Barrio, J. Ll. Tamarit, N. D. Mathur, W. Li and X. Moya, "Giant and reversible barocaloric effects in hybrid organic-inorganic azide perovskites" (in preparation)

Other studies published during the PhD period

- M. Barrio, R. Levit, P. Lloveras, A. Aznar, P. Negrier, D. Mondieig, J.-Ll. Tamarit, "Relationship between the two-component system 1-Br-adamantane + 1-Cl-adamantane and the high-pressure properties of the pure components", *Fluid Ph. Equilibria*, **459**, 219–229 (2018).

- A. Aznar, P. Lloveras, M. Barrio, J.-Ll. Tamarit, "Melting of orientational degrees of freedom", *Eur. Phys. J. Special Topics*, **226**, 1017 (2017).

Appendix A

Volume contribution to the $\Delta S_{\mathbf{t}}$

The differential form of $S(T, V)$ can be written as

$$dS = \left(\frac{\partial S}{\partial T}\right)_V dT + \left(\frac{\partial S}{\partial V}\right)_T dV$$

where

$$\begin{cases} \left(\frac{\partial S}{\partial T}\right)_V = \frac{1}{T}\left(\frac{T\partial S}{\partial T}\right)_V = \frac{1}{T}\left(\frac{\delta Q}{\delta T}\right)_V = \frac{1}{T}C_V \\ \left(\frac{\partial S}{\partial V}\right)_T = \left(\frac{\partial p}{\partial T}\right)_V . \end{cases} \tag{A.1}$$

If a change in volume with no configurational change is considered, at $T = \text{cte}$

$$dS = \left(\frac{\partial S}{\partial V}\right)_T dV = \left(\frac{\partial p}{\partial T}\right)_V dV.$$

Now using the cyclic rule, the following equation may be written.

$$\left(\frac{\partial p}{\partial T}\right)_V \left(\frac{\partial T}{\partial V}\right)_p \left(\frac{\partial V}{\partial p}\right)_T = -1,$$

for which we immediately obtain that

$$\left(\frac{\partial p}{\partial T}\right)_V = -\frac{\frac{1}{V}\left(\frac{\partial V}{\partial T}\right)_p}{\frac{1}{V}\left(\frac{\partial V}{\partial p}\right)_T} = \frac{\alpha}{\beta}.$$

Therefore, the following expression for dS at isothermal conditions for a volume change of dV reads

$$dS = \frac{\alpha}{\beta} dV.$$

If we now consider an initial state with (α_1, β_1) and a final state with (α_2, β_2) where $\frac{\alpha_1}{\beta_1} \approx \frac{\alpha_2}{\beta_2}$ is assumed, the following expression for the entropy change is obtained.

$$dS = \frac{\alpha}{\beta} dV \quad \longrightarrow \quad \Delta S = \int_1^2 \left(\frac{\alpha}{\beta}\right) dV \quad \rightarrow \quad \boxed{\Delta S = \left\langle \frac{\alpha}{\beta} \right\rangle \Delta V}$$

Appendix B

XRD measurements

X-ray diffraction for $MnCoGeB_{0.03}$

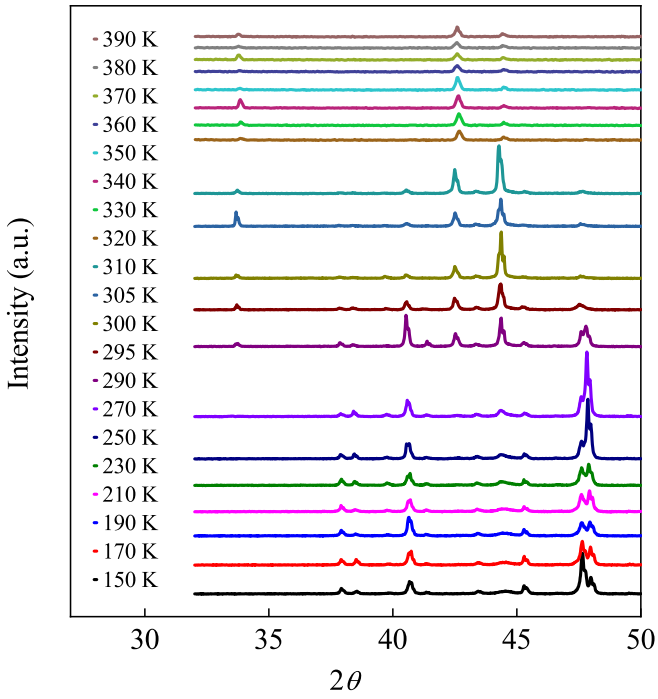

Figure B.1: X-ray diffraction patterns with respect to temperature for MnCoGeB. Measurements performed by the Chemistry Department and the Maxwell Center from University of Cambridge.

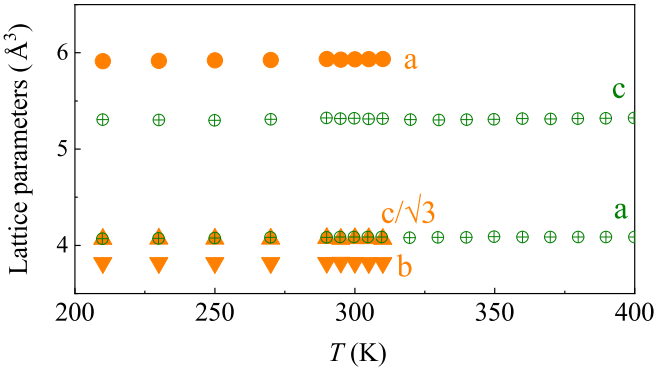

Figure B.2: Lattice parameters with respect to temperature for MnCoGeB. Orange and green dots stand for lattice parameters of phases II and I, respectively. Measurements performed by the Chemistry Department and the Maxwell Center from University of Cambridge.

X-ray diffraction for $Ni_{50}Mn_{31.5}Ti_{18.5}$

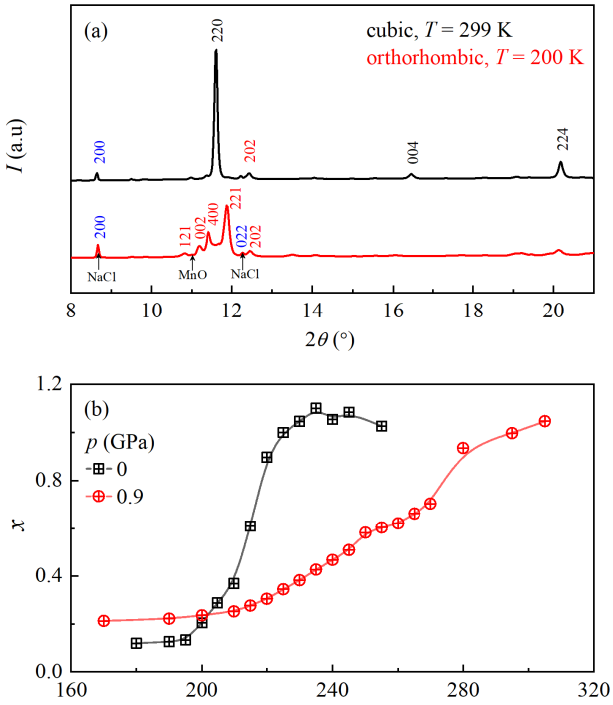

Figure B.3: (a) X-ray diffraction at p_{atm} measured at phases II and I. Panel (b) displays the fraction of mass evolution with respect to temperature taken from the diffraction peaks intensity.

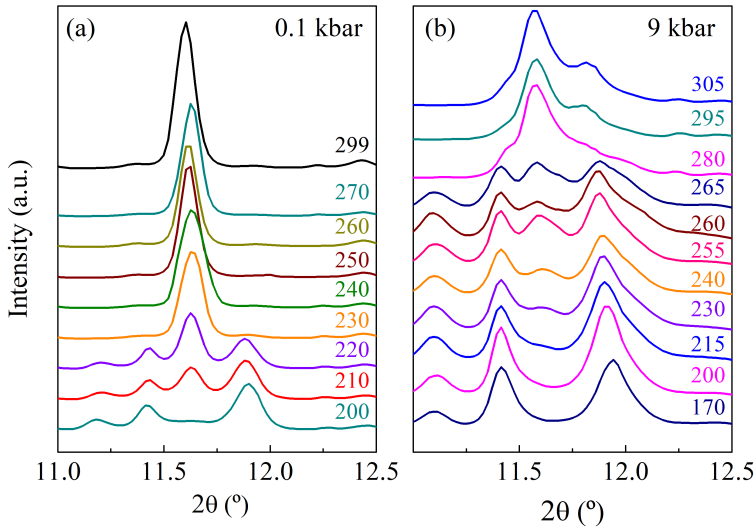

Figure B.4: X-ray diffraction measurements at (a) p_{atm} and (b) 9 kbar upon cooling. Temperature (in K) is indicated in for each measurement.

Appendix C

Barocaloric effects

Additional irreversible barocaloric results are presented in Fig. C.1-C.4. Table C.1 and C.2 summarize the irreversible caloric effects obtained upon heating and cooling respectively for all materials studied in this thesis.

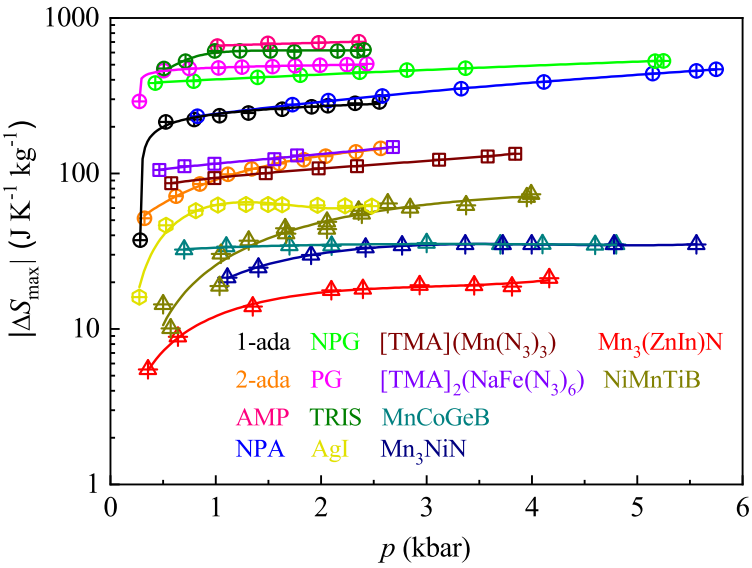

Figure C.1: Irreversible maximum values of $|\Delta S_{max}|$ at different pressure changes for cooling measurements.

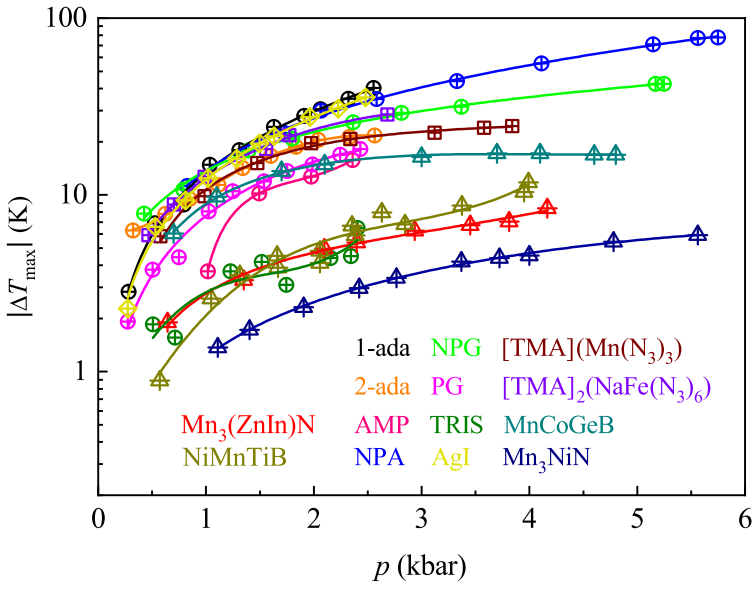

Figure C.2: Irreversible maximum values of $|\Delta T_{\max}|$ for cooling measurements at different pressure changes.

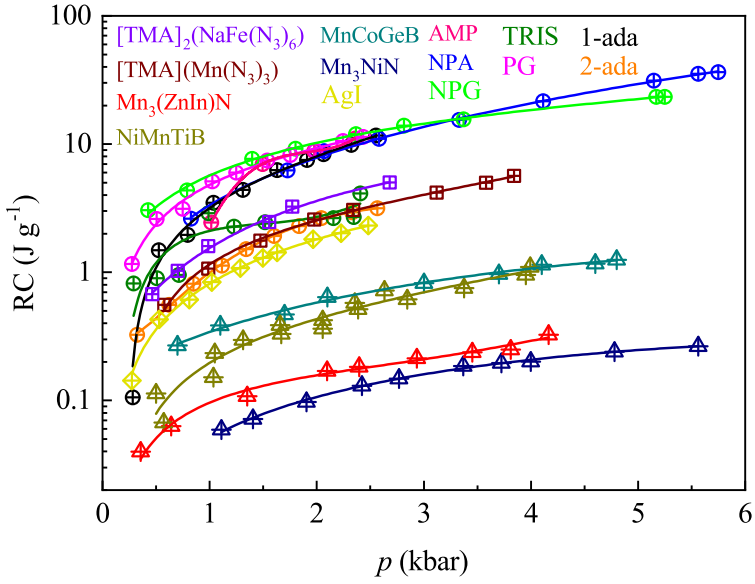

Figure C.3: Irreversible refrigerant capacity for cooling measurements with respect to pressure changes.

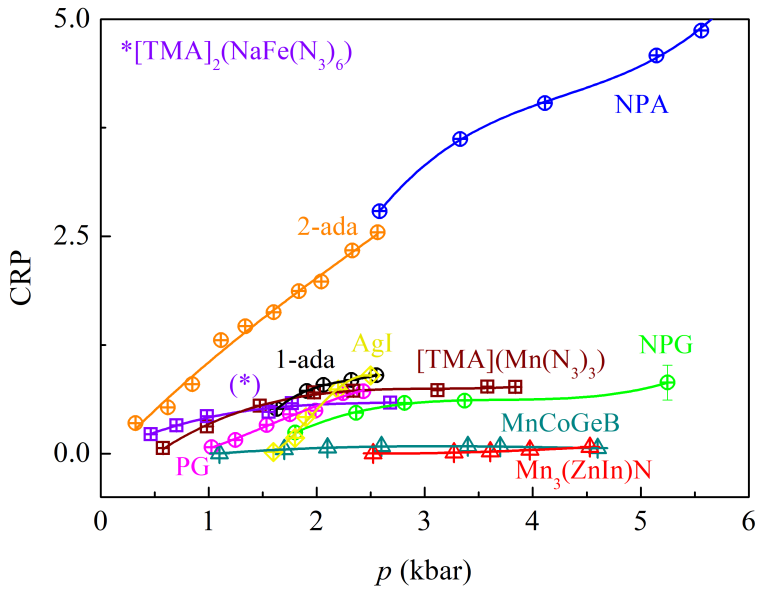

Figure C.4: Reversible CRP with respect to pressure changes.

Compound	p kbar	$\lvert\Delta T_{max}\rvert$ K	$\lvert\Delta S_{max}\rvert$ J K^{-1} kg^{-1}	RC J g^{-1}
Tris(hydroxymethyl)aminomethane	2.5	10 ± 1	580 ± 60	7.0 ± 0.8
2-amino-2-methyl-1,3-propanediol	2.5	15 ± 2	680 ± 70	11 ± 2
Pentaglycerine	2.4	18 ± 2	510 ± 50	9 ± 1
Neopentyl alcohol	2.7	40 ± 4	310 ± 40	19 ± 2
Neopentylglicol	2.5	24 ± 3	460 ± 50	12 ± 2
1-adamantanol	2.6	42 ± 5	310 ± 30	15 ± 2
2-adamantanol	2.6	17 ± 2	150 ± 20	2.6 ± 0.5
[TMA] ($Mn(N_3)_3$)	2.4	20 ± 2	120 ± 20	3.6 ± 0.5
$[TMA]_2$ ($NaFe(N_3)_6$)	2.4	25 ± 3	140 ± 20	4.7 ± 0.7
$MnCoGeB_{0.03}$	2.5	17 ± 2	35 ± 4	1.0 ± 0.1
Mn_3NiN	–	–	–	–
$Mn_3(ZnIn)N$	2.5	5 ± 1	15 ± 2	0.2 ± 0.1
NiMnTiB	2.7	6 ± 1	47 ± 5	0.4 ± 0.1
AgI	2.5	38 ± 4	57 ± 6	2.4 ± 0.3

Table C.1: Barocaloric effects obtained using heating runs.

Compound	p kbar	$\lvert\Delta T_{\max}\rvert$ K	$\lvert\Delta S_{\max}\rvert$ J K^{-1} kg^{-1}	RC J g^{-1}
Tris(hydroxymethyl)aminomethane	2.5	7 ± 1	630 ± 70	4.1 ± 0.8
2-amino-2-methyl-1,3-propanediol	2.5	15 ± 2	710 ± 70	11 ± 2
Pentaglycerine	2.4	22 ± 3	510 ± 50	11 ± 2
Neopentyl alcohol	2.7	32 ± 4	320 ± 40	11 ± 2
Neopentylglicol	2.5	26 ± 3	440 ± 50	12 ± 2
1-adamantanol	2.6	34 ± 4	290 ± 30	12 ± 2
2-adamantanol	2.6	17 ± 2	150 ± 20	3.2 ± 0.5
[TMA] $(Mn(N)_3)_3$	2.3	20 ± 2	110 ± 10	3.1 ± 0.3
$[TMA]_2\,(NaFe(N)_3)_6$	2.7	29 ± 3	150 ± 20	5.0 ± 0.7
$MnCoGeB_{0.03}$	2.1	19 ± 2	34 ± 4	0.6 ± 0.1
Mn_2NiN	2.4	3 ± 1	33 ± 4	0.10 ± 0.01
$Mn_3(ZnIn)N$	2.4	5 ± 1	18 ± 2	0.20 ± 0.02
NiMnTiB	2.6	8 ± 1	64 ± 7	0.7 ± 0.1
AgI	2.5	35 ± 4	60 ± 6	2.2 ± 0.3

Table C.2: Barocaloric effects obtained using cooling runs.

Bibliography

[1] J. Rees, *Refrigeration nation: a history of ice, appliances, and enterprise in America*, ch. 1, p. 20. JHU Press, 2013.

[2] University of Birminham, "A cool world: Defining the energy conundrum of cooling for all.." `https://www.birmingham.ac.uk/Documents/college-eps/energy/Publications/2018-clean-cold-report.pdf`. Online; accessed 30 November 2020.

[3] A. Cavallini *J. Phys. Conf. Ser.*, vol. 1599, p. 012001, 2020.

[4] S. F. Pearson, "Refrigerants past, present and future," in *The International Congress of refrigeration in Washington DC USA. [cited July 22, 2008]*, 2003.

[5] "Ammonia leak in shanghai kills 15: Local government." `https://www.hurriyetdailynews.com/ammonia-leak-in-shanghai-kills-15-local-government-53593`. Accessed: 2021-01-02.

[6] "Ammonia leak at refrigeration plant." `https://www.acr-news.com/ammonia-leak-at-refrigeration-plant`. Accessed: 2021-01-02.

[7] M. O. McLinden, C. J. Seeton, and A. Pearson *Science*, vol. 370, pp. 791–796, 2020.

[8] T. Midgley Jr and A. L. Henne *Ind. Eng. Chem*, vol. 22, pp. 542–545, 1930.

[9] S. Solomon, R. R. Garcia, F. S. Rowland, and D. J. Wuebbles *Nature*, vol. 321, pp. 755–758, 1986.

[10] M. Protocol *Washington, DC: US Government Printing Office*, vol. 26, pp. 128–136, 1987.

[11] E. A. Heath *Int. Leg. Mater.*, vol. 56, pp. 193–205, 2017.

[12] D. Coulomb, J. Dupont, and A. Pichard *29th Informatory Note on Refrigeration Technologies; Technical Report; International Institute of Refrigeration: Paris, France*, 2015.

[13] J. Gough *Mem. Proc. Manch. Lit. Philos. Soc*, vol. 1, pp. 288–295, 1805.

[14] P. Weiss and A. Piccard *C. R. Phys*, vol. 166, pp. 352–354, 1918.

[15] G. Brown *J. Appl. Phys*, vol. 47, pp. 3673–3680, 1976.

[16] P. Kobeko and J. Kurtschatov *Z. Phys*, vol. 66, pp. 192–205, 1930.

[17] C. Rodriguez and L. Brown *Metall. Mater. Trans. A*, vol. 11, pp. 147–150, 1980.

[18] S. Nikitin, G. Myalikgulyev, A. Tishin, M. Annaorazov, K. Asatryan, and A. Tyurin *Mod. Phys. Lett.*, vol. 148, pp. 363–366, 1990.

[19] T. Strässle, A. Furrer, P. Lacorre, and K. A. Müller *J. Alloys Compd*, vol. 303, pp. 228–231, 2000.

[20] L. Mañosa, D. González-Alonso, A. Planes, E. Bonnot, M. Barrio, J.-L. Tamarit, S. Aksoy, and M. Acet *Nat. Mater.*, vol. 9, pp. 478–481, 2010.

[21] C. J. Adkins and C. J. Adkins, *Equilibrium thermodynamics*, ch. 7, pp. 100–105. Cambridge University Press, 3 ed., 1983.

[22] E. Stern-Taulats, A. Gràcia-Condal, A. Planes, P. Lloveras, M. Barrio, J.-L. Tamarit, S. Pramanick, S. Majumdar, and L. Mañosa *Appl. Phys. Lett*, vol. 107, p. 152409, 2015.

[23] V. K. Pecharsky and K. A. Gschneidner Jr *Phys. Rev. Lett*, vol. 78, p. 4494, 1997.

[24] X. Moya, E. Stern-Taulats, S. Crossley, D. González-Alonso, S. Kar-Narayan, A. Planes, L. Mañosa, and N. D. Mathur *Adv. Mater.*, vol. 25, pp. 1360–1365, 2013.

[25] B. Neese, B. Chu, S.-G. Lu, Y. Wang, E. Furman, and Q. Zhang *Science*, vol. 321, pp. 821–823, 2008.

[26] A. Gràcia-Condal, E. Stern-Taulats, A. Planes, E. Vives, and L. Mañosa *Phys. Status Solidi B*, vol. 255, p. 1700422, 2018.

[27] E. Bonnot, R. Romero, L. Mañosa, E. Vives, and A. Planes *Phys. Rev. Lett*, vol. 100, p. 125901, 2008.

[28] P. Lloveras, A. Aznar, M. Barrio, P. Negrier, C. Popescu, A. Planes, L. Mañosa, E. Stern-Taulats, A. Avramenko, N. D. Mathur, X. Moya, and J.-L. Tamarit *Nat. Commun.*, vol. 10, pp. 1–7, 2019.

[29] L. Mañosa, E. Stern-Taulats, A. Planes, P. Lloveras, M. Barrio, J.-L. Tamarit, B. Emre, S. Yüce, S. Fabbrici, and F. Albertini *Phys. Status Solidi B*, vol. 251, pp. 2114–2119, 2014.

[30] P. Lloveras, E. Stern-Taulats, M. Barrio, J.-L. Tamarit, S. Crossley, W. Li, V. Pomjakushin, A. Planes, L. Mañosa, N. D. Mathur, *et al. Nat. Commun*, vol. 6, p. 8801, 2015.

[31] M. Gorev, E. Bogdanov, I. Flerov, and N. Laptash *J. Phys. Condens*, vol. 22, p. 185901, 2010.

[32] G. Jaeger *Arch. Hist. Exact Sci.*, vol. 53, pp. 51–81, 1998.

[33] P. Papon, J. Leblond, and P. H. Meijer, *Physics of Phase Transitions*, ch. 1, pp. 13–15. Springer, 2 ed., 2002.

[34] S. P. Vallone, A. N. Tantillo, A. M. dos Santos, J. J. Molaison, R. Kulmaczewski, A. Chapoy, P. Ahmadi, M. A. Halcrow, and K. G. Sandeman *Adv. Mater.*, vol. 31, p. 1807334, 2019.

[35] S. Yuce, M. Barrio, B. Emre, E. Stern-Taulats, A. Planes, J.-L. Tamarit, Y. Mudryk, K. A. Gschneidner Jr, V. K. Pecharsky, and L. Mañosa *Appl. Phys. Lett.*, vol. 101, p. 071906, 2012.

[36] E. Stern-Taulats, A. Planes, P. Lloveras, M. Barrio, J.-L. Tamarit, S. Pramanick, S. Majumdar, C. Frontera, and L. Mañosa *Phys. Rev. B*, vol. 89, p. 214105, 2014.

[37] E. Stern-Taulats, P. Lloveras, M. Barrio, E. Defay, M. Egilmez, A. Planes, J.-L. Tamarit, L. Mañosa, N. Mathur, and X. Moya *APL Mater.*, vol. 4, p. 091102, 2016.

[38] L. Mañosa, D. González-Alonso, A. Planes, M. Barrio, J.-L. Tamarit, I. S. Titov, M. Acet, A. Bhattacharyya, and S. Majumdar *Nat. Commun.*, vol. 2, pp. 1–5, 2011.

[39] J. L. Lebowitz *Phys. Today*, vol. 46, pp. 32–32, 1993.

[40] S. Yip, *Handbook of materials modeling*, ch. 7, p. 2145.

[41] M. Jenau, J. Reuter, J. L. Tamarit, and A. Würflinger *J. Chem. Soc. Faraday Trans.*, vol. 92, pp. 1899–1904, 1996.

[42] D. Wu, J. J. Gassensmith, D. Gouvêa, S. Ushakov, J. F. Stoddart, and A. Navrotsky *J. Am. Chem. Soc*, vol. 135, pp. 6790–6793, 2013.

[43] X. Moya, S. Kar-Narayan, and N. D. Mathur *Nat. Mater*, vol. 13, pp. 439–450, 2014.

[44] G. Bäckström and R. Ross *Int. J. Thermophys.*, vol. 6, pp. 101–105, 1985.

[45] M. Brokate and J. Sprekels, *Hysteresis and phase transitions*, vol. 121, pp. 1–10. Springer Science & Business Media, 2012.

[46] Y. Mnyukh *Am. J. Condens. Matter Phys.*, vol. 3, pp. 142–150, 2013.

[47] F. J. Pérez-Reche, E. Vives, L. Mañosa, and A. Planes *Phys. Rev. Lett*, vol. 87, p. 195701, 2001.

[48] B. Emre, S. Yüce, E. Stern-Taulats, A. Planes, S. Fabbrici, F. Albertini, and L. Mañosa *J. Appl. Phys*, vol. 113, p. 213905, 2013.

[49] E. Stern-Taulats, A. Planes, P. Lloveras, M. Barrio, J.-L. Tamarit, S. Pramanick, S. Majumdar, S. Yüce, B. Emre, C. Frontera, *et al. Acta Mater.*, vol. 96, pp. 324–332, 2015.

[50] T. Gottschall, E. Stern-Taulats, L. Mañosa, A. Planes, K. P. Skokov, and O. Gutfleisch *Appl. Phys. Lett*, vol. 110, p. 223904, 2017.

[51] A. Aznar, P. Lloveras, M. Romanini, M. Barrio, J.-L. Tamarit, C. Cazorla, D. Errandonea, N. D. Mathur, A. Planes, X. Moya, *et al. Nat. Commun*, vol. 8, pp. 1–6, 2017.

[52] A. Aznar, P. Lloveras, M. Barrio, P. Negrier, A. Planes, L. Mañosa, N. D. Mathur, X. Moya, and J.-L. Tamarit *J. Mater. Chem. A*, vol. 8, pp. 639–647, 2020.

[53] K. Gschneidner Jr and V. K. Pecharsky *Annu. Rev. Mater. Sci.*, vol. 30, pp. 387–429, 2000.

[54] E. Brück, H. Yibole, and L. Zhang *Philos. Trans. R. Soc. A*, vol. 374, p. 20150303, 2016.

[55] L. Mañosa and A. Planes *Appl. Phys. Lett*, vol. 116, p. 050501, 2020.

[56] M. Wood and W. Potter *Cryogenics*, vol. 25, pp. 667–683, 1985.

[57] NETZSCH, "Principle of a heat-flux DSC." `https://www.netzsch-thermal-analysis.com/en/landing-pages/principle-of-a-heat-flux-dsc/`. Online; accessed 12 October 2020.

[58] TA Instruments, "Discovery DSC." `https://www.tainstruments.com/wp-content/uploads/Discovery-DSC-Brochure.pdf`. Online; accessed 12 October 2020.

[59] "DSC differential scanning calorimeter." `http://physics-astronomy-manuals.wwu.edu/TA`. Accessed: 2020-02-20.

[60] G. Höhne, W. F. Hemminger, and H.-J. Flammersheim, *Differential scanning calorimetry*. Springer Science & Business Media, 2013.

[61] K. Kodre, S. Attarde, P. Yendhe, R. Patil, and V. Barge *Research and Reviews: J. Pharmaceutical Analysis (RRJPA)*, vol. 3, pp. 11–22, 2014.

[62] P. Gill, S. Sauerbrunn, and M. Reading *Journal of Thermal Analysis*, vol. 40, pp. 931–939, 1993.

[63] G. Höhne, W. F. Hemminger, and H.-J. Flammersheim, *Differential scanning calorimetry*, ch. 3, p. 53. Springer Science & Business Media, 2 ed., 2013.

[64] J. Schawe and G. Höhne *Thermochimica acta*, vol. 287, pp. 213–223, 1996.

[65] Leonard C. Thomas, "Modulated DSC paper 1." `http://www.tainstruments.com/pdf/literature/TP_006_MDSC_num_1_MDSC.pdf`. Accessed: 2018-08-29.

[66] E. S. Taulats, *Giant caloric effects in the vicinity of first-order phase transitions*. PhD thesis, Departament de Fisica de la Materia Condensada. Universitat de Barcelona, April 2017.

[67] "European synchrotron radiation facility (ESRF, Grenoble)." `https://www.esrf.eu/about/synchrotron-science/synchrotron`. Accessed: 2020-02-20.

[68] J. Timmermans *J. Chem. Phys*, vol. 35, pp. 331–344, 1938.

[69] W. Helfrich and G. Heppke, *Liquid Crystals of One-and Two-Dimensional Order*, vol. 11, pp. 47–48. Garmisch-Partenkirchen, Germany: Springer Science & Business Media, 2012.

[70] L. Staveley *Annu. Rev. Phys. Chem*, vol. 13, pp. 351–368, 1962.

[71] E. D. Emmons, J. C. Fallas, V. K. Kamisetty, W.-M. Chien, A. M. Covington, R. S. Chellappa, S. A. Gramsch, R. J. Hemley, and D. Chandra *J. Phys. Chem. B*, vol. 114, pp. 5649–5656, 2010.

[72] P. Negrier, M. Barrio, J. L. Tamarit, L. C. Pardo, and D. Mondieig *Cryst. Growth Des*, vol. 12, pp. 1513–1519, 2012.

[73] P. Negrier, J. L. Tamarit, M. Barrio, and D. Mondieig *Cryst. Growth Des*, vol. 13, pp. 782–791, 2013.

[74] B. B. Hassine, P. Negrier, M. Romanini, M. Barrio, R. Macovez, A. Kallel, D. Mondieig, and J. L. Tamarit *Phys. Chem. Chem. Phys*, vol. 18, pp. 10924–10930, 2016.

[75] A. H. Mones and B. Post *J. Chem. Phys*, vol. 20, pp. 755–756, 1952.

[76] National Center for Biotechnology Information, "PubChem Database, CID=10041." `https://pubchem.ncbi.nlm.nih.gov/compound/Neopentane`. Online; accessed 18 Mars 2020.

[77] N. C. for Biotechnology Information., "Pubchem database. cid=6503." https://pubchem.ncbi.nlm.nih.gov/compound/2-Amino-2-hydroxymethyl-propane-1_3-diol. Online; accessed 19 Mars 2020.

[78] M. Barrio, J. Font, D. López, J. Muntasell, J. L. Tamarit, P. Negrier, N. Chanh, and Y. Haget *J. Phys. Chem. Solids*, vol. 54, pp. 171–181, 1993.

[79] J. L. Tamarit, B. Legendre, and J. Buisine *Mol. Cryst. Liq. Cryst.*, vol. 250, pp. 347–358, 1994.

[80] D. Eilerman and R. Rudman *J. Chem. Phys*, vol. 72, pp. 5656–5666, 1980.

[81] D. Miller, J. Bryant, E. Madsen, and W. Ghiorse *Appl. Environ. Microbiol*, vol. 65, pp. 4715–4724, 1999.

[82] R. H. Kallet, R. M. Jasmer, J. M. Luce, L. H. Lin, and J. D. Marks *Am. J. Respir. Crit. Care Med*, vol. 161, pp. 1149–1153, 2000.

[83] M. Barrio, J. Font, D. López, J. Muntasell, J. L. Tamarit, P. Negrier, and Y. Haget *J. Phys. Chem. Solids*, vol. 55, pp. 1295–1302, 1994.

[84] National Center for Biotechnology Information, "PubChem Database, CID=1531." https://pubchem.ncbi.nlm.nih.gov/compound/2-Amino-2-methyl-1_3-propanediol. Online; accessed 25 Mars 2020.

[85] N. Sugimoto, K. Patel, and H. Abe, Nov. 7 2013. US Patent App. 13/980,418.

[86] K. Yamaguchi and S. Ishitobi, Nov. 15 2016. US Patent App. 13/575,043.

[87] A. F. de Castro and J. L. Neff, Nov. 6 1984. US Patent App. 548,042.

[88] P. Sevigny, Dec. 8 2016. US Patent App. 15/239,374.

[89] M. Barrio, J. Font, D. López, J. Muntasell, J. L. Tamarit, and F. Cossio *J. Phase. Equilibria. Diffus.*, vol. 12, no. 4, pp. 409–415, 1991.

[90] National Center for Biotechnology Information, "PubChem Database, CID=145641." https://pubchem.ncbi.nlm.nih.gov/compound/145641. Online; accessed 4 April 2020.

[91] D. Eilerman, R. Lippman, and R. Rudman *Acta Crystallogr. Sect. B-Struct. Sci*, vol. 39, pp. 263–266, 1983.

[92] R. A. Lewis, *Hawley's condensed chemical dictionary.* John Wiley & Sons, 2016.

[93] V. O. Sheftel, *Indirect food additives and polymers: migration and toxicology*, p. 422. CRC Press, 1 ed., 2000.

[94] R. A. Lewis, *Hawley's condensed chemical dictionary*, p. 1281. John Wiley & Sons, 15 ed., 2016.

[95] National Center for Biotechnology Information, "PubChem Database, CID=6404." `https://pubchem.ncbi.nlm.nih.gov/compound/Neopentyl-alcohol`. Online; accessed 6 April 2020.

[96] J. Salud, D. O. López, M. Barrio, and J. L. Tamarit *J. Mater. Chem*, vol. 9, pp. 909–916, 1999.

[97] E. G. Belder, F. A. Koldijk, F. Visser, T. A. Misev, A. R. Hofkamp, and M. Houweling, July 5 1994. US Patent App. 912,976.

[98] T. A. Girard and E. C. Slaght, Aug. 7 1962. US Patent App. 713,801.

[99] Y. Kokeguchi, Nov. 29 2016. US Patent App. 12/647,155.

[100] National Center for Biotechnology Information, "PubChem Database, CID=31344." `https://pubchem.ncbi.nlm.nih.gov/compound/Neopentyl-glycol`. Online; accessed 18 June 2020.

[101] C. Nordman and D. Schmitkons *Acta. Crystallogr.*, vol. 18, pp. 764–767, 1965.

[102] S. R. Salman, J. C. Lindon, and T. A. Carpenter *Thermochim. Acta.*, vol. 232, pp. 171–176, 1994.

[103] K. Aigami, Y. Inamoto, N. Takaishi, K. Hattori, A. Takatsuki, and G. Tamura *J. Med. Chem.*, vol. 18, pp. 713–721, 1975.

[104] J. Rabey, P. Nissipeanu, and A. Korczyn *Journal of neural transmission-Parkinson's disease and dementia section*, vol. 4, pp. 277–282, 1992.

[105] J. S. Wishnok *J. Chem. Educ*, vol. 50, p. 780, 1973.

[106] National Center for Biotechnology Information, "PubChem Database, CID=9238." `https://pubchem.ncbi.nlm.nih.gov/compound/Adamantane`. Online; accessed 8 April 2020.

[107] P. D. Harvey, D. F. Gilson, and I. S. Butler *Can. J. Chem*, vol. 65, pp. 1757–1760, 1987.

[108] National Center for Biotechnology Information, "PubChem Database, CID=64152." `https://pubchem.ncbi.nlm.nih.gov/compound/1-Adamantanol`. Online; accessed 14 April 2020.

[109] National Center for Biotechnology Information, "PubChem Database, CID=64149." `https://pubchem.ncbi.nlm.nih.gov/compound/2-Adamantanol`. Online; accessed 14 April 2020.

[110] S. R. Salman and K. F. Abas *Thermochim. Acta.*, vol. 142, pp. 245–249, 1989.

[111] M. Charapennikau, A. Blokhin, A. Kabo, and G. Kabo *J. Chem. Thermodyn*, vol. 35, pp. 145–157, 2003.

[112] P. Mekala in *TT Chen Honorary Symposium on Hydrometallurgy, Electrometallurgy and Materials Characterization*, p. 465, John Wiley & Sons, 2012.

[113] M. del Barrio, *Miscibilidad en fase plástica: La sincristalización entre los derivados del neopentano.* PhD thesis, Escola Tècnica Superior d'Enginyers Industrials de Barcelona. Universitat Politècnica de Catalunya, 1993.

[114] J. Salud, M. Barrio, D. López, J. L. Tamarit, and X. Alcobé *J. Appl. Crystallogr*, vol. 31, pp. 748–757, 1998.

[115] T. Bo, T. Zhi-Cheng, L. Rui-Bin, M. Chang-Gong, and Z. Jing-Nan *Energy Convers. Manag*, vol. 51, pp. 1905–1910, 2010.

[116] D. Chandra, W.-M. Chien, V. Gandikotta, and D. W. Lindle *Z. Phys. Chem*, vol. 216, p. 1433, 2002.

[117] M. Straka, A. van Genderen, K. Ruuvzička, and V. Ruuvzička *J. Chem. Eng. Data*, vol. 52, pp. 794–802, 2007.

[118] N. Kobelev, R. Nikolaev, N. Sidorov, and Y. M. Soifer *Phys. Solid State*, vol. 43, pp. 2344–2350, 2001.

[119] J. L. Schlenker, G. Gibbs, and M. Boisen *Acta Crystallogr. Sec. A*, vol. 34, pp. 52–54, 1978.

[120] G. Guthrie and J. McCullough *J. Phys. Chem. Solids*, vol. 18, pp. 53–61, 1961.

[121] G. Rose, *De novis quibusdam fossilibus quae in montibus Uraliis inveniuntur*. Berlin: Scripsit, 1839.

[122] W.-J. Xu, S. Kopyl, A. Kholkin, and J. Rocha *Coord. Chem. Rev.*, vol. 387, pp. 398–414, 2019.

[123] A. Bhalla, R. Guo, and R. Roy *Mater. Res. Innov.*, vol. 4, pp. 3–26, 2000.

[124] S. G. Z.-m. W. Wei Li, Alessandro Stroppa, *Hybrid Organic-Inorganic Perovskites*, ch. 1, pp. 1–3. Weinheim, Germany: Wiley-VCH, 1 ed., 2020.

[125] L. Zhou, X. Zheng, P.-P. Shi, Z. Zafar, H.-Y. Ye, D.-W. Fu, and Q. Ye *Inorg. Chem*, vol. 56, pp. 3238–3244, 2017.

[126] J. A. Schlueter, J. L. Manson, K. A. Hyzer, and U. Geiser *Inorg. Chem*, vol. 43, pp. 4100–4102, 2004.

[127] F.-J. Geng, L. Zhou, P.-P. Shi, X.-L. Wang, X. Zheng, Y. Zhang, D.-W. Fu, and Q. Ye *J. Mater. Chem. C*, vol. 5, pp. 1529–1536, 2017.

[128] X. Fang, B. Zong, and S. Mao *Nanomicro Lett.*, vol. 10, p. 64, 2018.

[129] H. Li, L. Li, R.-B. Lin, W. Zhou, Z. Zhang, S. Xiang, and B. Chen *EnergyChem*, vol. 1, p. 100006, 2019.

[130] V. Pascanu, G. González Miera, A. K. Inge, and B. Martín-Matute *J. Am. Chem. Soc*, vol. 141, pp. 7223–7234, 2019.

[131] M. T. Weller, O. J. Weber, P. F. Henry, A. M. Di Pumpo, and T. C. Hansen *ChemComm*, vol. 51, pp. 4180–4183, 2015.

[132] C. C. Stoumpos, C. D. Malliakas, and M. G. Kanatzidis *Inorg. Chem*, vol. 52, pp. 9019–9038, 2013.

[133] A. K. Jena, A. Kulkarni, and T. Miyasaka *Chem. Rev*, vol. 119, pp. 3036–3103, 2019.

[134] D. P. McMeekin, G. Sadoughi, W. Rehman, G. E. Eperon, M. Saliba, M. T. Hörantner, A. Haghighirad, N. Sakai, L. Korte, B. Rech, M. B. Johnston, L. M. Herz, and H. J. Snaith *Science*, vol. 351, pp. 151–155, 2016.

[135] J. M. Bermúdez-García, M. Sánchez-Andújar, and M. A. Señarís-Rodríguez *J. Phys. Chem. Lett*, vol. 8, pp. 4419–4423, 2017.

[136] L. C. Gómez-Aguirre, B. Pato-Doldán, A. Stroppa, L.-M. Yang, T. Frauenheim, J. Mira, S. Yáñez-Vilar, R. Artiaga, S. Castro-García, M. Sánchez-Andújar, *et al. Chem. Eur. J.*, vol. 22, pp. 7863–7870, 2016.

[137] Z.-Y. Du, Y.-P. Zhao, C.-T. He, B.-Y. Wang, W. Xue, H.-L. Zhou, J. Bai, B. Huang, W.-X. Zhang, and X.-M. Chen *Cryst. Growth Des*, vol. 14, pp. 3903–3909, 2014.

[138] E. Warburg *Ann. Phys.*, vol. 249, pp. 141–164, 1881.

[139] J. Liu, T. Gottschall, K. P. Skokov, J. D. Moore, and O. Gutfleisch *Nature materials*, vol. 11, pp. 620–626, 2012.

[140] A. Planes, L. Mañosa, and M. Acet *J. Phys. Condens. Matter*, vol. 21, p. 233201, 2009.

[141] A. G. Khachaturyan, *Theory of structural transformations in solids*, ch. 6, p. 153. Courier Corporation, 2013.

[142] D. Cong, W. Xiong, A. Planes, Y. Ren, L. Mañosa, P. Cao, Z. Nie, X. Sun, Z. Yang, X. Hong, and Y. Wang *Phys. Rev. Lett*, vol. 122, p. 255703, 2019.

[143] N. Trung, L. Zhang, L. Caron, K. Buschow, and E. Brück *Appl. Phys. Lett*, vol. 96, p. 172504, 2010.

[144] S. Kaprzyk and S. Niziol *J. Magn. Magn. Mater*, vol. 87, pp. 267–275, 1990.

[145] Q. Ren, *New materials for magnetic refrigeration: the magnetocaloric effect in MnCoGe-based intermetallics.* PhD thesis, School of Physical, Environmental, and Mathematical Sciences. University of New South Wales, Canberra, April 2016.

[146] G. Daniel-Pérez, J. S. Llamazares, P. Alvarez-Alonso, C. F. Sánchez-Valdés, R. Varga, V. Chernenko, and A. Quintana-Nedelcos *J. Magn. Magn. Mater*, vol. 444, pp. 263–269, 2017.

[147] C. F. Sánchez-Valdés, J. S. Llamazares, H. Flores-Zúñiga, D. Ríos-Jara, P. Alvarez-Alonso, and P. Gorria *Scr. Mater*, vol. 69, pp. 211–214, 2013.

[148] X. Si, Y. Liu, X. Lu, W. Wang, W. Lei, J. Lin, T. Zhou, and Y. Xu *J. Appl. Phys*, vol. 119, p. 215104, 2016.

[149] F. Zhu, J. Lin, W. Jiang, C. Yang, L. Li, X. Zhang, W. Song, X. Zhu, P. Tong, and Y. Sun *Scr. Mater*, vol. 150, pp. 96–100, 2018.

[150] A. Aznar, P. Lloveras, J.-Y. Kim, E. Stern-Taulats, M. Barrio, J. L. Tamarit, C. F. Sánchez-Valdés, J. L. Sánchez Llamazares, N. D. Mathur, and X. Moya *Adv. Mater.*, vol. 31, p. 1903577, 2019.

[151] P. Lukashev and R. F. Sabirianov *J. Appl. Phys*, vol. 107, p. 09E115, 2010.

[152] D. Boldrin, E. Mendive-Tapia, J. Zemen, J. B. Staunton, T. Hansen, A. Aznar, J.-L. Tamarit, M. Barrio, P. Lloveras, J. Kim, X. Moya, and L. F. Cohen *Phys. Rev. X.*, vol. 8, p. 041035, 2018.

[153] D. Fruchart, E. Bertaut, R. Madar, G. Lorthioir, and R. Fruchart *Solid State Commun.*, vol. 9, pp. 1793–1797, 1971.

[154] M. Wu, C. Wang, Y. Sun, L. Chu, J. Yan, D. Chen, Q. Huang, and J. W. Lynn *J. Appl. Phys*, vol. 114, p. 123902, 2013.

[155] D. Matsunami, A. Fujita, K. Takenaka, and M. Kano *Nat. Mater*, vol. 14, pp. 73–78, 2015.

[156] S. Iikubo, K. Kodama, K. Takenaka, H. Takagi, M. Takigawa, and S. Shamoto *Phys. Rev. Lett*, vol. 101, p. 205901, 2008.

[157] R. Huang, L. Li, F. Cai, X. Xu, and L. Qian *Appl. Phys. Lett*, vol. 93, p. 081902, 2008.

[158] K. Takenaka, A. Ozawa, T. Shibayama, N.-h. Kaneko, T. Oe, and C. Urano *Appl. Phys. Lett*, vol. 98, p. 022103, 2011.

[159] R. Niewa *Eur. J. Inorg. Chem.*, vol. 2019, pp. 3647–3660, 2019.

[160] B. Qu and B. Pan *J. Appl. Phys*, vol. 108, p. 113920, 2010.

[161] D. Fruchart, R. Fruchart, P. L'Héritier, K. Kanematsu, R. Madar, S. Misawa, Y. Nakamura, P. Webster, and K. Ziebeck, *Magnetic Properties of Metals: Alloys and Compounds of d-Elements with Main Group Elements. Part 2*, ch. 1, p. 226. Landolt-Börnstein - Group III Condensed Matter 19c : Condensed Matter, Springer-Verlag Berlin Heidelberg, 1 ed., 1988.

[162] C. Felser and A. Hirohata, *Heusler alloys*, ch. 1, p. 4. Switzerland: Springer, 1 ed., 2015.

[163] Z. Wei, E. Liu, Y. Li, X. Han, Z. Du, H. Luo, G. Liu, X. Xi, H. Zhang, W. Wang, *et al. Appl. Phys. Lett*, vol. 109, p. 071904, 2016.

[164] Z. Wei, Y. Shen, Z. Zhang, J. Guo, B. Li, E. Liu, Z. Zhang, and J. Liu *APL Mater.*, vol. 8, p. 051101, 2020.

[165] Z. Yang, D. Cong, X. Sun, Z. Nie, and Y. Wang *Acta Mater.*, vol. 127, pp. 33–42, 2017.

[166] Z. Wei, E. Liu, J. Chen, Y. Li, G. Liu, H. Luo, X. Xi, H. Zhang, W. Wang, and G. Wu *Appl. Phys. Lett*, vol. 107, p. 022406, 2015.

[167] S. Aksoy, M. Acet, P. Deen, L. Mañosa, and A. Planes *Phys. Rev. B*, vol. 79, p. 212401, 2009.

[168] V. Recarte, J. Pérez-Landazábal, V. Sánchez-Alarcos, V. Zablotskii, E. Cesari, and S. Kustov *Acta Mater.*, vol. 60, pp. 3168–3175, 2012.

[169] B. B. Owens *J. Power Sources*, vol. 90, pp. 2–8, 2000.

[170] M. B. Salamon, *Physics of superionic conductors*, vol. 15, ch. 1. Springer Science & Business Media, 2013.

[171] W. Kohlrausch *Ann. Phys.*, vol. 253, pp. 642–654, 1882.

[172] D. Axisa and T. P. DeFelice *Atmos. Res.*, vol. 178, pp. 114–124, 2016.

[173] I. Geresdi, L. Xue, N. Sarkadi, and R. Rasmussen *J. Appl. Meteorol. Climatol*, pp. 1–54, 2020.

[174] M. Kannan, K. Rajarathinam, S. Venkatesan, B. Dheeba, and A. Maniraj, *Silver Iodide Nanoparticles as an Antibiofilm Agent—A Case Study on Gram-Negative Biofilm-Forming Bacteria*, ch. 19, pp. 435–456. Amsterdam: Elsevier, 1 ed., 2017.

[175] F. E. Germann and M. C. Hylan *J. Am. Chem. Soc*, vol. 45, pp. 2486–2493, 1923.

[176] R. L. Daubendiek, "Photographic elements containing bright yellow silver iodide," June 9 1987. US Patent 4,672,026.

[177] A. Wright and B. Fender *J. Phys. C*, vol. 10, p. 2261, 1977.

[178] S. Hoshino *J. Phys. Soc. Jpn*, vol. 12, pp. 315–326, 1957.

[179] S. Hull *Rep. Prog. Phys*, vol. 67, p. 1233, 2004.

[180] R. Wilsey *Lond.Edinb.Dubl.Phil.Mag.*, vol. 46, pp. 487–496, 1923.

[181] B. Lawn *Acta Cryst.*, vol. 17, pp. 1341–1347, 1964.

[182] R. Shaviv, E. F. Westrum Jr, F. Grønvold, S. Stølen, A. Inaba, H. Fujii, and H. Chihara *J. Chem. Thermodyn*, vol. 21, pp. 631–651, 1989.

[183] G. Burley *Acta Crystallogr. A*, vol. 23, pp. 1–5, 1967.

[184] H. Wada and Y. Tanabe *Appl. Phys. Lett*, vol. 79, pp. 3302–3304, 2001.

[185] A. Kitanovski *Adv. Energy Mater.*, vol. 10, p. 1903741, 2020.

[186] J. Torrens-Serra, C. Biffi, R. Santamarta, V. Recarte, J. Pérez-Landazábal, A. Tuissi, and E. Cesari *Mater. Charact.*, vol. 93, pp. 24–31, 2014.

[187] A. Waske, E. Lovell, A. Funk, K. Sellschopp, A. Rack, L. Giebeler, P.-F. Gostin, S. Fähler, and L. Cohen *APL Mater.*, vol. 4, p. 106101, 2016.

[188] S. Nikitin, G. Myalikgulyev, M. Annaorazov, A. Tyurin, R. Myndyev, and S. Akopyan *Phys. Lett.*, vol. 171, pp. 234–236, 1992.

[189] R. Millán-Solsona, E. Stern-Taulats, E. Vives, A. Planes, J. Sharma, A. K. Nayak, K. Suresh, and L. Mañosa *Appl. Phys. Lett*, vol. 105, p. 241901, 2014.

[190] R.-R. Wu, L.-F. Bao, F.-X. Hu, H. Wu, Q.-Z. Huang, J. Wang, X.-L. Dong, G.-N. Li, J.-R. Sun, F.-R. Shen, *et al. Scientific reports*, vol. 5, p. 18027, 2015.

[191] F. Hu, S. Wei, Y. Cao, Z. Li, X. He, K. Xu, Y. Zhang, Y. Kang, H. Yang, and Q. Zhang *J. Alloys Compd*, vol. 818, p. 153356, 2020.

[192] X. He, Y. Kang, S. Wei, Y. Zhang, Y. Cao, K. Xu, Z. Li, C. Jing, and Z. Li *J. Alloys Compd*, vol. 741, pp. 821–825, 2018.

[193] Q. Zheng, S. E. Murray, Z. Diao, A. Bhutani, D. P. Shoemaker, and D. G. Cahill *Phys. Rev. Mater.*, vol. 2, p. 075401, 2018.

[194] Z. Liqiang, W. Daolian, T. Jie, L. Wen, W. Wei, H. Rongjin, and L. Laifeng *RARE METAL MAT ENG.*, vol. 43, pp. 1304–1307, 2014.

[195] Y. Shao, M. Zhang, H. Luo, A. Yan, and J. Liu *Appl. Phys. Lett*, vol. 107, p. 152403, 2015.

[196] Y. Yang, Q.-C. Zhang, Y.-Y. Pan, L.-S. Long, and L.-S. Zheng *ChemComm*, vol. 51, pp. 7317–7320, 2015.

[197] Y. Ouyang, M. Zhang, A. Yan, W. Wang, F. Guillou, and J. Liu *Acta Mater.*, vol. 187, pp. 1–11, 2020.

[198] J. M. Bermúdez-García, M. Sánchez-Andújar, S. Castro-García, J. López-Beceiro, R. Artiaga, and M. A. Señarís-Rodríguez *Nat. Commun*, vol. 8, pp. 1–8, 2017.

[199] M. Szafrański, W.-J. Wei, Z.-M. Wang, W. Li, and A. Katrusiak *APL Mater.*, vol. 6, p. 100701, 2018.

[200] A. Pisoni, J. Jacimovic, O. S. Barisic, M. Spina, R. Gaál, L. Forró, and E. Horváth *J. Phys. Chem. Lett*, vol. 5, pp. 2488–2492, 2014.

[201] C. Ge, M. Hu, P. Wu, Q. Tan, Z. Chen, Y. Wang, J. Shi, and J. Feng *J. Phys. Chem. C*, vol. 122, pp. 15973–15978, 2018.

[202] X. Qian, X. Gu, and R. Yang *Nano Energy*, vol. 41, pp. 394–407, 2017.

[203] S. G. Z.-m. W. Wei Li, Alessandro Stroppa, *Hybrid Organic-Inorganic Perovskites*, ch. 4, pp. 185–186. Weinheim, Germany: Wiley-VCH, 1 ed., 2020.

[204] Z. Yi, N. H. Ladi, X. Shai, H. Li, Y. Shen, and M. Wang *Nanoscale*, vol. 1, pp. 1276–1289, 2019.

[205] A. K. Sagotra, D. Chu, and C. Cazorla *Nat. Commun*, vol. 9, pp. 1–7, 2018.

[206] J. Min, A. K. Sagotra, and C. Cazorla *Phys. Rev. Mater.*, vol. 4, p. 015403, 2020.

[207] M. Goetz and J. Cowen *Solid State Commun.*, vol. 41, pp. 293–295, 1982.

[208] C. Fajardo, G. Costa, L. Ortiz, M. Nande, M. Rodríguez-Membibre, M. Martín, and S. Sánchez-Fortún *Ecotoxicol. Environ. Saf.*, vol. 133, pp. 433–441, 2016.

[209] B. D. Williams and J. A. Denhom *J. Weather Modif*, vol. 41, pp. 75–96, 2009.

[210] R. B. Standler and B. Vonnegut *J. Appl. Meteorol.*, no. 8, pp. 1388–1391, 1972.

[211] C. Son and J. Morehouse *J Thermophys Heat Trans*, vol. 5, pp. 122–124, 1991.

[212] J. Wigren and P. Andersson *Mol. Cryst. Liq. Cryst.*, vol. 59, pp. 137–148, 1980.

[213] D. Szewczyk, A. Jeżowski, A. I. Krivchikov, and J. L. Tamarit *J. Low Temp. Phys.*, vol. 41, pp. 469–472, 2015.

[214] J. M. Bermúdez-García, S. Yáñez-Vilar, A. García-Fernández, M. Sánchez-Andújar, S. Castro-García, J. López-Beceiro, R. Artiaga, M. Dilshad, X. Moya, and M. A. Señarís-Rodríguez *J. Mater. Chem. C*, vol. 6, pp. 9867–9874, 2018.

[215] P. Lloveras, T. Samanta, M. Barrio, I. Dubenko, N. Ali, J.-L. Tamarit, and S. Stadler *APL Mater.*, vol. 7, p. 061106, 2019.

[216] T. Samanta, P. Lloveras, A. Us Saleheen, D. L. Lepkowski, E. Kramer, I. Dubenko, P. W. Adams, D. P. Young, M. Barrio, J. L. Tamarit, *et al. Appl. Phys. Lett*, vol. 112, p. 021907, 2018.

[217] J. Li, D. Dunstan, X. Lou, A. Planes, L. Mañosa, M. Barrio, J. L. Tamarit, and P. Lloveras *J. Mater. Chem. A*, 2020.